LUND UNIVERSITY

Surface guided radiotherapy

Kügele, Malin

2021

Document Version:
Publisher's PDF, also known as Version of record

Link to publication

Citation for published version (APA):
Kügele, M. (2021). *Surface guided radiotherapy*. [Doctoral Thesis (compilation), Faculty of Science]. Lund University, Faculty of Science.

Total number of authors:
1

Creative Commons License:
Unspecified

General rights
Unless other specific re-use rights are stated the following general rights apply:
Copyright and moral rights for the publications made accessible in the public portal are retained by the authors and/or other copyright owners and it is a condition of accessing publications that users recognise and abide by the legal requirements associated with these rights.
• Users may download and print one copy of any publication from the public portal for the purpose of private study or research.
• You may not further distribute the material or use it for any profit-making activity or commercial gain
• You may freely distribute the URL identifying the publication in the public portal

Read more about Creative commons licenses: https://creativecommons.org/licenses/

Take down policy
If you believe that this document breaches copyright please contact us providing details, and we will remove access to the work immediately and investigate your claim.

LUND UNIVERSITY

PO Box 117
221 00 Lund
+46 46-222 00 00

Surface guided radiotherapy

Surface guided radiotherapy

Malin Kügele

LUND
UNIVERSITY

DOCTORAL DISSERTATION

by due permission of the Faculty of Science, Lund University, Sweden.
To be defended in the Torsten Landberg lecture hall, 3rd floor in the Radiotherapy building, Klinikgatan 5, Skåne University Hospital, Lund.
September 17th at 13.00 AM.

Faculty opponent
Marco Schwarz, Ph.D.
Head of Proton Medical Physics, Trento, Italy

Organization LUND UNIVERSITY Department of Medical Radiation Physics Clinical Sciences, Lund Faculty of Science	**Document name** **Doctoral Dissertation** **Date of issue**
Author(s) Malin Kügle	Sponsoring organization

Title and subtitle Surface Guided Radiotherapy

Abstract

Modern radiotherapy aims to treat the decease while minimizing the radiation dose to the adjacent normal tissue, to minimize acute and late effects of the treatment. The foremost technological approaches have been intensity modulated radiotherapy (IMRT) and intensity modulated proton therapy (IMPT) in combination with image guided radiotherapy (IGRT). IMRT and IMPT is characterized by a more conform dose distribution, often accompanied by steep dose gradients. In turn, accurate patient localization and motion management becomes more important. Several image guidance systems are available for radiotherapy (RT), with 3-dimensional (3D) volumetric images with cone beam computed tomography (CBCT) as a gold standard. In recent years, surface imaging (SI) using an optical surface scanning system has been included in the IGRT toolbox. The SI system Catalyst^{TM} (C-rad Positioning AB, Uppsala Sweden) visualize 3D surface images of the patient topography, and direct correlate the patient localization to the initial planned position. SI offers the largest field-of-view in RT, does not contribute to radiation exposure, provides real-time feedback and sub-millimeter spatial resolution. These characteristics are suitable for both patient positioning and motion management during RT.

Integration with the linac provides beam control and automatic couch shifts, which imposes rigorous attention to quality assurance (QA) of the SI systems. In order to integrate the beam control, beam latency times (beam-on and beam-off) should be characterized, which required the development PIN diode circuit as a QA tool. Of extra importance was the measurements of the beam-off latency time, since it represents the time the linac continues to irradiate after the beam hold signal was sent from the SI system. The automatic couch shift is calculated by a deformable image registration (DIR) algorithm, unique for the Catalyst^{TM} surface scanning system. Positioning accuracy is dependent on the image registration, and hence, a deformable thorax phantom was developed to investigate accuracy of the DIR with anatomical realistic deformations present as a QA tool.

Compared to traditional 3-point localization for patient positioning, this thesis has shown that SI improve the positioning for both breast and prostate cancer patients. Also, the SI workflow has shown to be time efficient for positioning of prostate cancer patients. A respiratory motion management technique is deep inspiration breath hold (DIBH), where the patient is instructed to hold his/her breath during the treatment delivery. The aim using DIBH, is to create an anatomical distance between the treatment volume and surrounding organs-at-risk (OARs). Comparative treatment planning studies, within the work of this thesis, showed that DIBH can be an effective method for both left sided breast cancer and Hodgkin's lymphoma (HL) in order to spare dose to the heart. For HL, the combination of IMPT and DIBH was found to spare dose to OARs, however, due to the spread in target localization individual deviations from this treatment technique were observed. The real-time feedback from the surface image system was used to investigate the reproducibility of the DIBH to ensure correct dose distribution during the treatment delivery. High reproducibility of the isocenter position during DIBH was observed, however, for a few breath holds larger deviations occurred which urges the need to use beam control tolerance for the isocenter.

The overall conclusion is that optical imaging systems, developed within the work of this thesis, can be used as an imaging tool for accurate and faster patient setup, intrafractional motion monitoring and reduced dose to OARs during treatment in DIBH.

Key words Radiotherapy, Surface Guided Radiotherapy, SGRT, patient positioning, interfraction motion, DIBH, breast cancer, Hodgkin's lymphoma, linac latency times, deformable image registration

Classification system and/or index terms (if any)

Supplementary bibliographical information	**Language** English
ISSN and key title	**ISBN** 978-91-7895-955-6 (pdf) 978-91-7895-956-3 (print)

Recipient's notes	**Number of pages** 68	Price
	Security classification	

I, the undersigned, being the copyright owner of the abstract of the above-mentioned dissertation, hereby grant to all reference sources permission to publish and disseminate the abstract of the above-mentioned dissertation.

Signature  Date 2021-08-10

Surface guided radiotherapy

Malin Kügele

LUND
UNIVERSITY

Cover photo by Malin Kügele

Copyright © p. 1-68 Malin Kügele 2021

Paper I © Elsevier Masson SAS

Paper II © John Wiley and Sons

Paper III © Taylor & Francis Group

Paper IV © John Wiley and Sons

Paper V © John Wiley and Sons

Paper VI © Elsevier Masson SAS

Faculty of Science, Lund University
Department of Medical Radiation Physics

ISBN 978-91-7895-955-6 (pdf)
ISBN 978-91-7895-956-3 (print)

Printed in Sweden by Media-Tryck, Lund University
Lund 2021

Media-Tryck is a Nordic Swan Ecolabel certified provider of printed material. Read more about our environmental work at www.mediatryck.lu.se

MADE IN SWEDEN

To my beloved daughter Smilla
- my never ending creative source

Abstract

Modern radiotherapy aims to treat the decease while minimizing the radiation dose to the adjacent normal tissue, to minimize acute and late effects of the treatment. The foremost technological approaches have been intensity modulated radiotherapy (IMRT) and intensity modulated proton therapy (IMPT) in combination with image guided radiotherapy (IGRT). IMRT and IMPT is characterized by a more conform dose distribution, often accompanied by steep dose gradients. In turn, accurate patient localization and motion management becomes more important. Several image guidance systems are available for radiotherapy (RT), with 3-dimensional (3D) volumetric images with cone beam computed tomography (CBCT) as a gold standard. In recent years, surface imaging (SI) using an optical surface scanning system has been included in the IGRT toolbox. The SI system Catalyst™ (C-rad Positioning AB, Uppsala Sweden) visualize 3D surface images of the patient topography, and direct correlate the patient localization to the initial planned position. SI offers the largest field-of-view in RT, does not contribute to radiation exposure, provides real-time feedback and sub-millimeter spatial resolution. These characteristics are suitable for both patient positioning and motion management during RT.

Integration with the linac provides beam control and automatic couch shifts, which imposes rigorous attention to quality assurance (QA) of the SI systems. In order to integrate the beam control, beam latency times (beam-on and beam-off) should be characterized, which required the development PIN diode circuit as a QA tool. Of extra importance was the measurements of the beam-off latency time, since it represents the time the linac continues to irradiate after the beam hold signal was sent from the SI system. The automatic couch shift is calculated by a deformable image registration (DIR) algorithm, unique for the Catalyst™ surface scanning system. Positioning accuracy is dependent on the image registration, and hence, a deformable thorax phantom was developed to investigate accuracy of the DIR with anatomical realistic deformations present as a QA tool.

Compared to traditional 3-point localization for patient positioning, this thesis has shown that SI improve the positioning for both breast and prostate cancer patients. Also, the SI workflow has shown to be time efficient for positioning of prostate cancer

patients. A respiratory motion management technique is deep inspiration breath hold (DIBH), where the patient is instructed to hold his/her breath during the treatment delivery. The aim using DIBH, is to create an anatomical distance between the treatment volume and surrounding organs-at-risk (OARs). Comparative treatment planning studies, within the work of this thesis, showed that DIBH can be an effective method for both left sided breast cancer and Hodgkin's lymphoma (HL) in order to spare dose to the heart. For HL, the combination of IMPT and DIBH was found to spare dose to OARs, however, due to the spread in target localization individual deviations from this treatment technique were observed. The real-time feedback from the surface image system was used to investigate the reproducibility of the DIBH to ensure correct dose distribution during the treatment delivery. High reproducibility of the isocenter position during DIBH was observed, however, for a few breath holds larger deviations occurred which urges the need to use beam control tolerance for the isocenter.

The overall conclusion is that optical imaging systems, developed within the work of this thesis, can be used as an imaging tool for accurate and faster patient setup, intrafractional motion monitoring and reduced dose to OARs during treatment in DIBH.

Populärvetenskaplig sammanfattning

Strålbehandling är en vanlig förekommande behandlingsmetod för att stråla bort cancertumör, bromsa sjukdomen eller lindra symptom. Idag uppskattas det att ungefär hälften av alla som föds i Sveriges någon gång under sin livstid kommer att drabbas av cancer, och att ungefär hälften av dessa cancerfall kommer att erhålla strålbehandling. Inför sin strålbehandling scannas patienten i en datortomograf för att erhålla 3-dimensionella (3D) röntgenbilder över den del av kroppen där strålning ordinerats. Onkologer använder sig ofta av bilder från flera olika typer av bildgivande undersökningar, så som magnetkameraresonansbilder för ökad mjukvävnads-upplösning eller positronemissionstomografi (PET) för att avläsa var tumören är eller var aktiv. Bilderna matchas med varandra, så att onkologen kan rita ut exakt var tumören eller operationsbädden är lokaliserad. Sedan optimerar en dosplanerare behandlingen i ett dosplaneringsprogram, så att stråldosen hamnar i det utritade området samtidigt som omkringliggande frisk vävnad skonas i så lång utsträckning som möjligt. Optimering görs genom att dosplaneraren först väljer energi för strålningen, dvs. dess genomträningsförmåga genom kroppen. Sedan anpassas flertalet strålfält i storlek och riktning till det utritade området med målet att erhålla en hög och jämn stråldos där. Det är vanligt att strålbehandlingen består i flertalet fasta strålfält från olika ingångsriktningar, men på senare år har mer dynamiska behandlingar dominerat strålbehandlingen. De dynamiska strålbehandlingarna erbjuder fler frihetsgrader gällande strålleveransen, där intensiteten i strålen kan moduleras i varje vinkel kring patienten samtidigt som strålfältet hela tiden formas om för att ytterligare skydda intilliggande riskorgan. På detta sätt genereras en unik strålplan för varje patient som presenteras för onkologer och sjukhusfysiker för bedömning. Godkänns strålplanen går den vidare för ytterligare granskning av sjukhusfysiker och sjuksköterskor, och i vissa fall utförs även kontrollmätningar inför behandlingsstart. De behandlingsmaskiner som vanligtvis används för strålbehandling är linjäracceleratorer, som genererar högenergetisk fotonstrålning. Även högenergetiska protoner används vid strålbehandling i Sverige idag, även om denna typ av behandling är ovanligare än behandling med fotonstrålning. Behandling med protoner ges på Skandionkliniken i Uppsala. Den stora skillnaden mellan de två strålslagen för strålbehandling är att protonerna deponerar sin energi mer specifikt och därmed kan frisk vävnad ytterligare

skonas från strålningsbidrag. Detta fenomen är av extra vikt för unga patienter som annars kan riskera sekundära långtidseffekter av strålningen.

Strålbehandling ges vanligtvis dagligen under ca en månads tid och därför krävs det att patienten positioneras identiskt i förhållande till strålfälten från dag till dag under sin behandling. För att säkra en korrekt positionering av patienten används olika indexerade tillbehör som spänns fast i behandlingsbritsen. Det kan exempelvis vara nackkuddar i kombination med en avgjuten plastmask som spänns fast över patientens ansikte och axlar. När patienten positionerats i behandlingsrummet styr personalen behandlingen från ett strålskyddat manöverrum. För att verifiera patientens position används oftast 3D röntgenbilder som matchas mot en referensbild från strålplanen. Ofta resulterar denna matchning i en mindre justering av behandlingsbritsens position som sker automatiskt från manöverrummet och sedan kan behandlingen levereras. Det är viktigt att patienten ligger stilla under leveransen av strålbehandlingen som tar ett par minuter. För att kunna övervaka att patienterna ligger still under sin strålbehandling kan ett optiskt ytskanningssystem användas, vilka har utvecklats för bred klinisk användning de senaste 10 åren. Dessa optiska system skannar av patientens hudyta i realtid med hjälp av ett synligt ljus utan att extra strålbidrag tillförs patienten. I systemet skapas 3D modeller av patienten vilket möjliggör att man kan använda dem för positionering och sedan följa varje rörelse patienten gör under behandlingen. Den här avhandlingen har visat på att optisk ytskanning kan positionera patienter noggrannare än konventionella metoder och därmed användas kliniskt för att positionera bröst- och prostatacancerpatienter. För hyperfraktionerad prostata-behandling, där patienten erhåller en hög stråldos under få behandlingstillfällen, har våra studier visat att positionering med ytskanning även förkortar tiden för positioneringen vilket kan ses som fördelaktigt då det kan medföra en ökad noggrannhet i precision. Andningen är en rörelse som är oundviklig under strålbehandling. I vissa fall önskar man att styra patientens andning för att skapa större avstånd mellan behandlingsområdet och den friska vävnaden. Så är fallet för vänstersidig bröstcancer och för patienter med Hodgkins lymfom där man genom att styra patienten till en djup inandning kan separera behandlingsområdet från hjärtat och lungvävnad. Det ökade avståndet medför att strålarna kan fokuseras till behandlingsområdet samtidigt som den friska vävnaden skonas från strålningen, vilket kan bidra till minskade strålningsrelaterade skador. För att ytterligare fokusera strålningen till behandlingsområdet har vi i denna avhandling visat att det är effektivt att kombinera behandling i djup inandning med protonstrålning för patienter med Hodgkins lymfom. Tack vare studierna publicerade i denna avhandling har optisk ytskanning introducerats kliniskt på Skånes Universitetssjukhus för att dagligen komma våra cancerpatienter till nytta.

List of Papers

I. **Latency Characterization of Gated Radiotherapy Treatment Beams Using a PIN Diode Circuit**
Lempart M., Kügele M., Ambolt L., Blad B. & Nordström F.
Innovation and Research in BioMedical engineering, 37, 3, p. 144-151 (2016)

II. **Dosimetric effects of intrafractional isocenter variation during deep inspiration breath-hold for breast cancer patients using surface-guided radiotherapy**
Kügele M., Edvardsson A., Berg L., Alkner S., Andersson Ljus C., Ceberg S.
Journal of Applied Clinical Medical Physics, 19, 1, p. 25-38 (2018)

III. **Comparative treatment planning study for mediastinal Hodgkin's lymphoma: impact on normal tissue dose using deep inspiration breath hold proton and photon therapy**
Edvardsson A.*, Kügele M.*, Alkner S., Enmark M., Nilsson J., Kristensen I., Kjellén E., Engelholm S., Ceberg S.
*contributed equally to this work.
Acta Oncologica, 58, 1, p. 95-104 (2018)

IV. **Surface Guided Radiotherapy (SGRT) improves breast cancer patient setup accuracy**
Kügele M., Mannerberg A., Nørring Bekke S., Alkner S., Berg L., Mahmood F., Thornberg C., Edvardsson A., Bäck S. Å. J., Behrens F. C., Ceberg S.
Journal of Applied Clinical Medical Physics, 20, 9, p. 61-68 (2019)

V. **Validation of a commercial deformable image registration for surface guided radiotherapy using an ad-hoc developed deformable phantom**
Pallotta S., Kügele M., Redapi L., Ceberg S.
Medical Physics, 47, 12, p. 6310-6318 (2020)

VI. **Faster and more accurate patient positioning with surface guided radiotherapy for ultra-hypofractionated prostate cancer patients**
Mannerberg A., Kügele M., Hamid S., Edvardsson A., Petersson K., Gunnlaugsson A., Bäck ÅJ S., Engelholm S., Ceberg S.
Accepted for publication in Technical Innovations & Patient Support in Radiation Oncology (July 2021)

The author's contributions

Paper I — I initiated the scientific work, took part in the design of the method and contributed to the data acquisition and analysis of the data. I wrote parts of the manuscript and also reviewed and commented on the manuscript.

Paper II — I identified the scientific question and developed the method for data acquisition. I did the data analysis, wrote the manuscript and was the first author.

Paper III — I significantly contributed to the planning of the study, development of the clinical workflow to enable data acquisition, also, treatment planning and interpretations of the result. Me and A. Edvardsson shared the first authorship due to equally contribution of the work and writing of the paper.

Paper IV — I contributed significantly to the development of the method, data acquisition, interpretation of the results. I wrote the paper and was the first author.

Paper V — I contributed to the scientific question, the design of the method and participated in all of the data acquisition. I interpreted the result and significantly contributed to the writing of the paper.

Paper VI — I contributed in the scientific question and data collection. Also, I significantly contributed to the writing of the paper.

Other related publications not included in this thesis

Full papers

VII. **Development of a novel radiotherapy motion phantom using a stepper motor driver circuit and evaluation using optical surface scanning**
Lempart M., Kügele M., Snäll J., Ambolt L., Ceberg S.
Australasian Physical and Engineering Sciences in Medicine, 40, 3, p. 717-727 (2017)

VIII. **Recent advances in Surface Guided Radiation Therapy**
Freislederer P., Kügele M., Öllers M., Swinnen A., Sauer T. O., Bert C., Giantsoudi D., Corradini S., Batista V.
Radiation oncology, 15, 1, 187 (2020)

IX. **Clinical paradigms and challenges in surface guided radiation therapy: Where do we go from here?**
Batista V., Meyer J., Kügele M., Al-Hallaq H.
Radiotherapy and Oncology, 153, p. 34-42 (2020)

X. **Surface-Guided Radiation Therapy as a Tool for Improving Patient Safety**
Al-Hallaq H., Batista V., Kügele M., Ford E., Viscariello N., Meyer J.
Accepted for publication in Radiotherapy and Oncology (Aug 2021)

Conference papers

i. **EP-1687: Reduced fixation with optical monitoring for palliative whole brain radiotherapy treatment**
Kügele M., Thornberg C., Kjellén E., Nordström F., Engelholm S.
Conference: ESTRO. Radiotherapy and Oncology 111, p. 242 (2014)

ii. **PTC17-0493: Clinical Commissioning of Gated Proton Pencil Beam Scanning**
Enmark M., Lundkvist N., Fager Ferrari M., Kügele M., Nyström H., Ceberg S.
Additional Proceedings to the 56th Annual Meeting of the Particle Therapy Cooperative Group (PTCOG). Int J Part Ther. 4:39, (2017).

iii. **PTC17-0288: Patient Positioning and Motion Management Using Optical Surface Scanning – an End-To-End Study within the Swedish National Proton Project**
Enmark M, Kügele M., Bünte K., Ceberg S.
Additional Proceedings to the 56th Annual Meeting of the Particle Therapy Cooperative Group (PTCOG). Int J Part Ther. 4:39, (2017).

iv. **EP-1978: Surface guided coplanar and non-coplanar stereotactic radiotherapy in with open masks – a phantom study**
Konradsson E., Kügele M., Petersson K., Gebre-Medin M., Ceberg S.
Conference: ESTRO. Radiotherapy and Oncology, 133, p. 1079-1080 (2019)

v. **EP-1958: Eight different open face masks compatibility with surface guided radiotherapy**
Kügele M., Konradsson E., Nilsing M., Ceberg S.
Conference: ESTRO. Radiotherapy and Oncology, 133, p. 1068 (2019)

vi. **OC-0352: Increased accuracy in reduced time – surface guided RT for hypofractionated prostate cancer patients**
Mannerberg A., Kügele M., Hamid S., Petersson K., Gunnlaugsson A., Bäck S. Å., Engelholm S., Ceberg S.
Conference: ESTRO. Radiotherapy and Oncology, 152, p. 189 (2020)

Guidelines

Surface Guided Radiotherapy: Report of AAPM Task Group 302

Hania A. Al-Hallaq PhD, University of Chicago, Chicago, IL (Chair)
Laura Cerviño, PhD, Memorial Sloan Kettering Cancer Center, New York, NY (co-Chair)
Alonso N Gutierrez, PhD, MBA, Miami Cancer Institute, Miami, FL
Wolfgang A. Tomé, PhD, Albert Einstein College of Medicine, Bronx, NY
Todd Pawlicki, PhD, University of California, San Diego, San Diego, CA
Laura Padilla, PhD, Virginia Commonwealth University, Richmond, VA
Malin Kügele, MS, Skåne University Hospital/Lund University, Lund, Sweden
Xiaoli Tang, PhD, Yale University, New Haven, CT
Amanda Havnen-Smith, PhD, Mayo Clinic, Northfield, MN
Koren Smith, MS, Mary Bird Perkins Cancer Center, Baton Rouge, LA
Nicholas Remmes, PhD Mayo Clinic, Rochester, MN
Susan A. Higgins, MD, Yale University, New Haven, CT

Abbreviations

3D	three-dimensional
3D-CRT	three-dimensional conformal radiotherapy
AP-PA	anterior-posterior – posterior-anterior
CBCT	cone beam computed tomography
CT	computed tomography
CTV	clinical target volume
CTV-T	primary tumour clinical target volume
DIBH	deep inspiration breath hold
DIR	deformable image registration
D_{mean}	mean dose
DoF	degrees-of-freedom
DVH	dose volume histogram
EPDC	electrical PIN diode circuit
FB	free breathing
FDG	18F-fluoro-deoxyglucose
Gy	Gray
HI	heterogeneity index
HL	Hodgkin's lymphoma
ID	integral dose
IGRT	image guided radiotherapy
IMPT	intensity modulated proton therapy
IMRT	intensity modulated radiotherapy
ISRT	involved site radiotherapy
kV	kilovolt
LAD	left anterior descending coronary artery
LBS	laser based setup

linac	linear accelerator
MCU	micro controller unit
MU	monitor unit
MV	megavolt
OAR	organ at risk
OSS	optical surface scanning
PBS	pencil beam scanning
PET	positron emission tomography
PT	proton therapy
pts	patients
PTV	planning target volume
RPM	real-time position management
RR	rigid registration
RT	radiotherapy
SBS	surface based setup
SGRT	surface guided radiotherapy
SI	surface imaging
TPS	treatment planning system
VMAT	volumetric modulated arc therapy
$V_{X\%/Gy}$	volume that receives a dose ≥X%/Gy
QA	quality assurance

Table of Contents

Abstract 9
Populärvetenskaplig sammanfattning 11
List of Papers 13
Abbreviations 17
Table of Contents 19
1. Introduction 21
2. Aims 25
3. Background 27
3.1 Optical Surface Scanning Technologies 27
3.2 Image registration algorithms 29
3.3 Surface guided patient positioning 30
3.4 Surface guided patient motion monitoring 31
3.5 Surface guided deep inspiration breath hold 32
3.6 Linac integration with beam control 35
3.7 Statistics 35
4. Quality assurance 37
4.1 Beam latency characterization for gated beams 37
4.2 Validation of the image registration algorithms 39
5. Surface guided patient positioning 41
5.1 Patient selection 41
5.2 Target delineation 41
5.3 Treatment planning 42
5.4 Assessment of inter fraction motion 42
5.5 Setup time for surface guided radiotherapy 45

6. Surface guided breathing adapted radiotherapy 47
6.1 Patient selection 47
6.2 CT acquisition 47
6.3 Target delineation 48
6.4 Treatment planning 48
6.5 Assessment of intra fraction motion 49
6.6 Dosimetric analysis and statistical tests 50
7. Conclusions 57
8. Future outlook 59
9. Acknowledgements 61
10. References 63

1. Introduction

Cancer is commonly treated with a combination of surgery, chemotherapy, immunotherapy and radiotherapy (RT). Approximately, half of all diagnosed cancer cases are treated with RT. According to the Swedish cancer statistics, prostate cancer (16,3% of all cancers, 10 474 cases) and breast cancer (14% of all cancers, 8986 cases) are the two most common cancer diseases [1]. For breast cancer, an adjuvant radiotherapy post-surgery, or chemotherapy in combination with surgery, have shown to reduce the risk of locoregional recurrence as well as breast cancer death [2, 3]. The relative five year survival after the diagnosis is 90%, which shows that there is a large group of women that are long-term survivors [1]. Similar survival rates are reported for patients with Hodgkin's lymphoma (HL), although much fewer patients (183 new cases reported in Sweden, 2016) compared to breast cancer patients that gets diagnosed with this disease each year [1, 4, 5]. The diagnosis of HL is mainly divided into two age groups, 25-30 years and after 50 years [1] and for breast cancer the median age for diagnosis is 60 years. For both breast cancer and HL, radiation-sensitive healthy organs are adjacent to the tumour site, primarily the heart and lungs. These healthy organs are inevitably irradiated during RT. Several studies have shown an increased risk of cardiovascular and pulmonary disease for breast cancers [6-12] and for HL [13-15], thus, it is important to reduce the absorbed dose to healthy tissue to minimize the risk of late effects induced by the RT. Efforts have been made for increased conformity of the beam delivery, such as development of intensity modulated radiotherapy (IMRT), volumetric modulated arc therapy (VMAT) and intensity modulated proton therapy (IMPT). These advanced treatment deliveries are often associated with steep dose gradients adjacent to the healthy tissue, and therefor show a higher sensibility to patient position uncertainties and patient motion [16].

For patients with intermediate-to-high-risk prostate cancer, an ultra-hypofractionation protocol has recently become practice in RT [17]. The RT treatment is delivered in fewer treatment sessions and with a higher dose per treatment [17], for which accurate and fast patient positioning is warranted. Also, the beam delivery should preferably be as short as possible due to the increased risk of prostate motion [18-20], which has led to the use of flattening-filter-free (FFF) treatments in order to shorten the treatment times [21]. In order to improve the patient positioning and/or track the patient motion

during the treatment delivery imaging techniques inside the treatment room were developed, either on-board to the linac or imaging systems separate to the linac. The gold standard for image guided radiotherapy (IGRT) is cone beam computed tomography (CBCT), which generates a three-dimensional (3D) volumetric image of the patient. Other imaging modalities commonly used for IGRT are planar kilovolt (kV) x-ray imaging, planar megavolt (MV) imaging, in-room computed tomography (CT), and ultra-sound [22]. IGRT is used to verify the treatment position close in time prior to the treatment delivery [23], and for real-time imaging, fluoroscopy imaging is available with the drawback of increased imaging dose to the patient. Daily verification imaging contributes to increased dose to the patient [24], and therefore several different imaging strategies have been developed to minimize the amount of verification images during the course of the treatment [25]. The current standard of care uses a 3-point localization method for initial patient positioning, where three skin tattoos are matched with in-room lasers. Verification imaging is used to correct for setup deviations in both translational and rotational directions. However, some setup deviations such as the arm position for breast cancer patients requires manual adjustments of the patient posture. Correction of patient posture using verification imaging can be difficult and require multiple imaging which is both time consuming and contribute to increased imaging dose to the patient [24]. In recent years optical surface scanning systems (OSSs) have been included in the IGRT toolbox [26]. Using the principle of optical triangulation, a known structured light pattern is projected onto the patient and the camera-detected images are used to reconstruct a 3D surface image of the patient (figure 1).

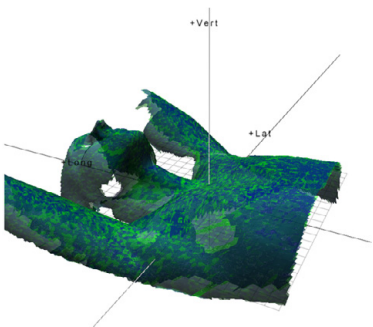

Figure 1. Surface image of a patient's thorax in real time during RT treatment.

The SI is registered to a reference image for calculation of the patient's position. The main advantages of surface guided radiotherapy (SGRT) are that the patient position can be assessed in real time, without the use of ionizing radiation to image the patient. Consequently, daily imaging can be used for both patient positioning and motion monitoring during the treatment. SI provides the largest field of view (FOV) available in RT, and contributes with information about the patient posture and topographical

information [27], as well as rotations [28]. This highlights the use of SGRT in a proactive manner to improve the patient position prior to verification imaging. Improved patient setup accuracy has been observed for both whole [28-32] and partial breast cancer treatments [33, 34]. For breast cancer patients, the SI guidance can improve the breast's surface registration to the reference position (e.g. by carrying out corrections of the patient's arm position) which is not visible in portal film or by the 3-point localization method [28, 29, 35]. Since the patient setup is a multi-step procedure, the use of SGRT have led to various improvement in the clinical workflow, such as transition to 3D verification images for reduced intra-observer subjectivity [28] and improving the immobilization [36]. The SGRT workflow efficiency have also been improved with regards to the overall treatment time for linac [37, 38], closed boar linacs [39] and proton therapy (PT) [36]. There are limitations in the registration accuracy for OSSs, foremost when the target-to-surface displacement increases which is commonly present for deep-seated tumours and targets that are heavily affected by internal motion. This has also been demonstrated in several studies, with the result of a reduced setup accuracy for targets in the pelvic and abdominal regions [30, 35, 40, 41]. However, SI achieved at least the same result as the 3-point localization method and was therefore still considered a valuable tool since SI provides with complimentary information about the patient topography [27, 30, 40]. The registration accuracy could potentially decrease due to target deformations, causing the live surface to be significantly deformed compared to the reference surface. The traditional registration algorithm has been a rigid registration (RR) [42], however, lately a deformable image registration (DIR) [43, 44] was developed in an attempt to reduce the registration error for deformed SIs [45]. The clinical effect of using DIR compared to RR have yet to be further investigated, however, small differences in patient setup was observed by Laaksomaa et al., using two OSSs with a RR and a DIR algorithm implemented, respectively [32]. Real-time SI has also been utilized for motion tracking and respiratory gating. The OSSs motion management capabilities covers both the intra-fraction patient motion and the respiratory motion of the patient, for both linac and computer tomography (CT) beam control. The real-time imaging can be used for SI during treatments in deep inspiration breath hold (DIBH). Treatment in DIBH, has shown to decrease dose for the heart and lung while keeping the target coverage for breast cancer patients [46-48]. The position of the breast is imaged by the OSS system for every DIBH. Compared to conventional IGRT, where images commonly are captured during a single DIBH for each treatment session the OS system provides increased information about the intrafractional patient motion. During a DIBH treatment, rapid respiratory motion into and out of the treatment position occurs. To avoid irradiation outside the planned treatment position, it is important to verify that the system has a fast response to the linac. In combination with 3D volumetric imaging, both at CT

and at the linac, SI can be used as a surrogate for internal anatomical patient motion. This combined imaging strategy is commonly used for patients receiving treatment for mediastinal HL, where efforts recently have been made to reduce dose to organs at risk by combining treatment in DIBH with IMPT [49, 50].

SI has in recent years reconfigured the clinical practice, hence, aids the therapists in the daily workflow to increase the accuracy and efficiency for patient setup. Improvements in patient positioning and real-time monitoring capabilities in combination with increased conformity of the beam delivery result in decreased dose to OARs, which have the potential to reduce long term effects of the RT treatment.

2. Aims

The overall aim was to develop optical surface scanning for clinical application in radiotherapy with regards to motion management; investigate potential improvements in patient setup, intrafractional motion monitoring and dosimetric impact of DIBH.

The specific aims for each study were:

Study I

The aim of this work was to design an electrical PIN diode circuit (EPDC) which is able to measure beam-on and beam-off latencies of gated radiation beams and which can be used with different combinations of accelerators and gating systems. This would provide a usable quality assurance (QA) tool for radiotherapy clinics for latency time measurements.

Study II

The aim of this study was to investigate potential dose reductions to organs at risk (OARs) using DIBH and optical surface scanning for left sided breast cancer, and further evaluate how any dosimetric benefits are affected of possible intrafractional isocenter motion in between breath holds.

Study III

The aim of this study was to investigate the impact on the normal tissue dose and target coverage, using various combinations of intensity modulated proton therapy (IMPT), volumetric modulated arc therapy (VMAT) and three-dimensional conformal radiotherapy (3D-CRT) planned in both deep inspiration breath hold (DIBH) and free breathing (FB) for patients receiving radiotherapy (RT) for Hodgkin's lymphoma (HL).

Study IV

The aim of this study was to retrospectively compare laser based setup (LBS) with surface based setup (SBS) using the optical surface scanning (OSS) system Catalyst™ for both tangential and locoregional breast cancer patients using single and three camera systems.

Study V

The purpose of this study was to investigate the accuracy of deformable image registration (DIR) compared to rigid image registration (RR) using a deformable phantom and CBCT as a reference. The DIR positioning accuracy compared to RR, was investigated for different target positions and anatomical deformations, and also, type of reference surface used.

Study VI

The aim of this study was to investigate if SGRT could improve the setup workflow by reducing the setup time while maintaining the positioning accuracy for prostate patients receiving ultra-hypofractionation flattening-filter-free (FFF)-VMAT treatment.

3. Background

3.1 Optical Surface Scanning Technologies

All optical surface scanning systems uses a combination of a projector and one or several 3D camera units. There are four main technologies used for OSS systems in radiotherapy today; laser scanners, time-of-flight systems, stereovision systems and structured light systems. All systems use an absolute coordinate system that is calibrated to treatment isocenter.

3.1.1 Laser scanning system

Laser scanning systems consists of one unit with a laser emitter, an optical scanner and a camera, and was first presented by Brahme et al. [51] for the use in radiotherapy. The system uses a narrow line laser that is redirected with an optical scanner consisting of a galvanometer and a mirror (figure 2). The fan shaped line laser is swept over the surface to be scanned. A metal-oxide semiconductor camera is capturing the laser light projected onto the object [51]. The 3D contour can be reconstructed by a back projection of the camera recorded laser signal, using the principle of optical triangulation [52]. The advantage of this technology is that the system has a high accuracy, however, the disadvantage is that it is slow (several seconds) when scanning a full patient surface.

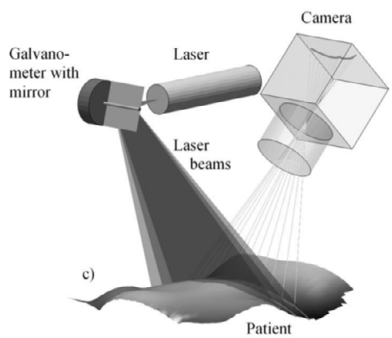

Figure 2. Schematic picture of a laser scanning system with the fan shaped line laser sweeping over the patient surface and the camera detecting the laser signal [51].

3.1.2 Time-of-flight system

Time-of-flight systems use a pulsed light source of intensity modulated near-infrared light that is recorded by a camera. By detecting the time it takes for the emitted light pulse to be reflected back to the detector, the distance to the object being scanned can be determined at each pixel [52, 53]. The advantages of these systems are that a large volume can be scanned with high speed [52]. The main disadvantage is that that accuracy has not yet reached sub millimetre [53, 54].

3.1.3 Stereo vision system

Stereo vision systems consist of two cameras and one projector unit. The system uses the principle of optical triangulation to determine the 3D surface by projecting a speckled pattern onto the object being scanned [52]. The speckled pattern contributes to visual uniqueness to each point of the surface being scanned and the 3D position of a set of points can be recorded by the camera. The system shows high accuracy [55], but moderate speed.

3.1.4 Structure light system

Structure light systems uses a sequence of known patterns projected onto the object being scanned [56]. The pattern gets disrupted by the 3D characteristics of the surface being scanned and the disrupted pattern is recorded by the camera. The reconstruction of the 3D surface is determined by comparison of the projected and captured patterns to identify the coordinated of each pixel in the image. The advantage is that the system has a high accuracy, however, moderate speed.

3.1.5 Registration techniques

For registration of the patient position, the various OSS systems uses different calculation models. A rigid registration is commonly used, and is based on a closest point iteration between the live and the reference surface. The registration technique uses region-of-interest (ROI) to restrict the registration to an anatomical location. A potential disadvantage is that the ROI is subjectively chosen by the user [29]. A deformable registration uses the whole surface scanned, with weighting of the surface closer to the isocenter [43, 57, 58]. In addition, a depth calculation is carried out to compute the isocenter shift [44]. The registration becomes objective, however, a disadvantage is that the registration is more sensitive to the image quality of the surface above the isocenter.

The optical surface scanning systems Sentinel™ and Catalyst™ (C-rad Positioning AB, Uppsala, Sweden), which are laser scanning systems and structured light systems, respectively, were used in the studies presented in this thesis. The Sentinel™ OSS system uses a rigid registration, and the Catalyst™ uses a deformable registration.

3.2 Image registration algorithms

The live surface required by the OSS system is registered to the reference surface in the software to obtain the required couch shifts for correct patient positioning. The alignment of the 3D image pair is an optimization problem, which is commonly solved using rigid image registration (RR) or DIR. The basic input data in the registration are the image pair pre-processed into the shape of a surface mesh with corresponding graph nodes. For RR, the graph nodes corresponding to the live surface are matched to the graph nodes in the reference surface with a closest neighbour approach. The registration summarizes the result from all the graph nodes and provide a global calculation result in 6 degrees-of-freedom (DoF). The method does not take into account local deformations in the live surface, and in a worst case scenario, deformations not related to the target position can heavily affect the calculated shifts. In order to minimize the effect of local deformations, a ROI approach has been developed where the users define areas of interest in the reference surface. The graph nodes included in the ROI are employed with a higher significance than graph nodes outside the ROI, commonly applied to bony anatomy as a surrogate to the target volume.

The Catalyst™ is the only OSS system that has a DIR implemented to account for anatomical deformations in the live surface. DIR starts similar to RR, as the basic input data in the registration are the two surfaces pre-processed into the shape of a surface mesh of triangles. The 3D image pair is assigned with a deformation node graph, and corresponding nodes on each node graph are matched using a closest neighbours' iteration. Further, DIR applies a non-linear algorithm in an iterative optimization process to minimize the sum for each deformation node energy. The rigidity is initially set high and thereafter reduced for each iterative step in order to account for local deformations in the 3D surfaces, and in tandem keep a global maximum rigidity. Local deformations found in this step of the calculation is identified and back projected onto the patient skin in the form of a colour map. In the last step, the isocenter position in calculated using a volumetric mesh consisting of uniformly distributed cubes associated to each graph node of the reference surface mesh and to the deformable node graph mesh preciously calculated. As a result, the isocenter position in 6 DoF with regards to the setup deviation and deformation is calculated.

3.3 Surface guided patient positioning

In a surfaces guided radiotherapy (SGRT) workflow the reference surface for the patient setup can be generated in two different ways; the body surface produced/generated from the automatic contouring in the treatment planning system (TPS) (i.e., DICOM), or a SI from a Sentinel™ or Catalyst™ system at CT. The reference surface used depends on the specific clinical workflow for the patient. Information from the treatment plan is imported to the Catalyst™ work station and a template is assigned to the patient. Templates can be target specific (i.e. thorax, pelvis, head & neck etc.) or patient specific with individual settings. The template contains a tolerance table for the treatment isocenter, surface matching and the surface colour map. In the template the scanning volume, calculation resolution, and smoothing of the breathing motion is set. Once the OSS system has calculated the patient position, an "Auto-Go-To" function can be used to automatically shift the couch into the correct position. The Catalyst™ is connected to the linac for beam control, and hence, if the system detects larger deviations than the once defined in the template the beam is halted.

3.3.1 Tolerances

Tolerances for patient positioning is set in the template. The tolerance should be small, ideally zero, however, the patients are moving during and after the positioning procedure and therefor a small setup tolerance (commonly <2mm) is assigned. The setup tolerances have to be fulfilled, otherwise the operator is not allowed to proceed to treatment delivery.

3.3.2 Scanning volume

The scanning volume used for patient positioning and monitoring is determined in the template. For accurate calculation of the isocenter position, the surface included in the scanning volume needs to include anatomical topography, reflect light, and preferably contain the isocenter. The size of the scanning volume determines how much of the scanning volume that will be included for the isocenter calculation. For faster calculations, a smaller surface is of advantage, however, important anatomical features might be excluded and therefore a larger surface is often used although the calculation time is increased.

3.3.3 Breathing motion mean value

Primarily in the thorax and abdomen, the patient breathing motion is large and can affect the calculated isocenter position. A mean value filter is applied to the live surface to minimize the effect of the breathing motion. Typically, 4-8 seconds is used clinically.

3.3.4 Colour map

Patient posture corrections are carried out manually with the guidance of a projected colour map onto the patient's surface. In the first steps of the Catalyst™ DIR, a closest neighbour iteration in combination with a non-linear algorithm between the SI pair defines local deformations. Local deformations can be visualized onto the patient's skin, if the distance between the live and reference images exceeds a pre-set value defined by the user in the template. The system projects the colour map onto the patient's skin for live updates of the patient posture. Corrections are carried out manually by the therapist.

3.3.5 Single and three camera installations

The Catalyst™ was first produced as a single camera system with a master camera installed in the ceiling by the end of the treatment couch. However, due to camera shadowing important surface above the isocenter could in some clinical cases be lost with a single camera system. The Catalyst™ HD system is a three camera solution, with the master camera in the same position as the single camera system, combined with two side cameras installed in a 120-degree angle from each other. This configuration enables a full 360-degree view of the object being scanned, hence, increased information about the patient posture.

3.4 Surface guided patient motion monitoring

During treatment delivery the OSS system monitors the patient motion. The motion of the patient surface and the calculated isocenter shift are recorded and tolerances for the detected motion are set in the target specific, or patient specific, template prior to treatment.

A daily reference surface is captured prior to treatment delivery. The reference image is acquired over several seconds and a floating mean value of the patient position is applied to minimize effects of the breathing motion. The daily reference surface is matched with the live surface and tolerances for deviations in the patient posture and shifts in

the calculated isocenter controls if the treatment beam should be turned on/off. Shifts in the isocenter caused by patient motion is calculated by the OSS system. The tolerance for the isocenter shift should relate to the accepted intrafractional motion defined by the margins in the treatment plan. The surface tolerance is commonly set to include the FB respiratory motion to avoid frequent beam interruptions One of the limiting factors for patient monitoring, is that the same size of the scanning volume is used for both patient positioning and motion monitoring. Another limiting factor is that the same surface tolerance is applied to the whole surface within the scanning volume, hence, the user cannot define areas that would be more important than others.

3.5 Surface guided deep inspiration breath hold

3.5.1 Deep inspiration breath hold

During a DIBH, the patient is coached to breathe in deep and hold the breath for an extended time, typically 15-20 sec. In the Catalyst™ system's software, a ROI is defined by the user to track the breathing motion. The ROI is tracking the surface motion in the vertical (vrt) direction at the defined coordinate in space. During a DIBH the patient's anatomy is moving both in vrt and longitudinal (lng) direction. It is thus advantageous to define the ROI on an anatomical flat surface to avoid detection of a shift in vrt direction that is due to the patient motion in lng direction during a DIBH, and hence, not the breathing motion. The surface above the xiphoid process is commonly used to track the breathing motion during DIBH. Initially the baseline is tracked, which is defined as the respiratory expiration during FB (figure 3a and b). The baseline is acquired in the beginning of each DIBH treatment session over several FB cycles. During the DIBH, the patient breathes in until reaching the gating window (figure 3a, b and c). The distance between the baseline and the gating window is referred to as the DIBH amplitude. The size of the gating window defined how much residual motion that is allowed during beam-on, typically set to 3 mm (figure 3b and c).

Visual guidance

Visual guidance for DIBH using the Catalyst™ and Sentinel™ systems was first investigated by Berg et al. 2015 (figure 3a) [59] . Audio coached DIBH was compared with audio-video coached DIBH.

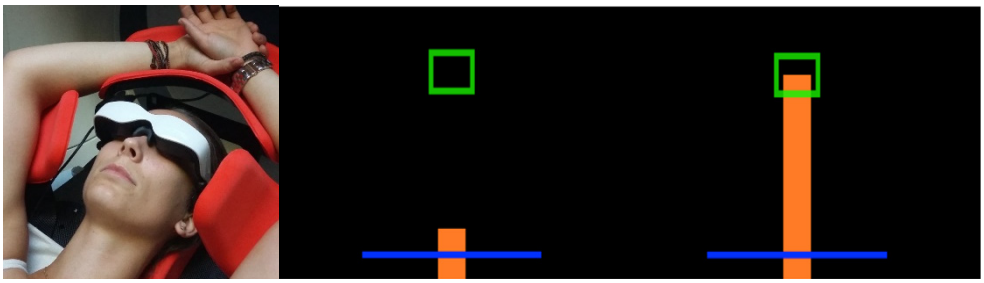

Figure 3. ***a)*** Visual guidance for deep inspiration breath hold (DIBH) using video googles. ***b)*** This image illustrated what the patient see in the googles. The orange bar moves in real time with the recorded breathing motion of the patient. The blue line is the baseline, defined as the expiration phase of the free breathing (FB) motion. ***c)*** The green box visualizes the gating window, set in the optical surface scanning systems software. The distance between the baseline and the gating window is the amplitude of the DIBH.

The reproducibility of the breath holds, i.e. how well the patient can reach the same inspiration level for repeated DIBHs, was significantly improved when introducing the visual guidance. Also the DIBH stability, i.e. for how long the signal was kept in the gating window, was significantly improved compared to audio guided DIBH. Visual guidance also showed that higher DIBH amplitudes could be reached, however, if the amplitude was set too high there was an increased risk for arcing the spine to reach the DIBH amplitude rather than breathing deeper, so called fake breathing. Overall, the visual guidance provided with the surface scanners have improved the reproducibility and stability of the DIBH, which can lead to fewer beam interruptions during treatment delivery. Commonly, the patient is able to hold her/his breath for a full field delivery (10-20 s), depending on the amount of monitor units (MU) and dose rate [59].

3.5.2 CT acquisition

Sentinel™ uses laser divided into three lines that sweep over the patient to create the 3D SI. The Sentinel™ system is a precursor to the more advanced Catalyst™ systems. The laser scanning process takes several seconds and therefore the system cannot be used to monitor an entire patient's surface in real time. On the other hand, this simpler optical surface technique is excellent at the CT, when only a reference SI of the patient is acquired. A reference surface in FB is captured by the Sentinel™ prior to the DIBH practice and CT scan. This reference surface will later be used for patient positioning with the Catalyst™ at the linac. The primarily reason to use a SI as reference image is to apply the As Low As Reasonably Achievable (ALARA) philosophy for minimizing imaging dose [24], thus using the SI reference surface spares a CT scan in FB. Since Sentinel™ is limited to the three laser beams for high speed surface detection, only a

smaller area can be monitored in real time. For monitoring the respiratory movement, an anatomical area of the patient is defined in Sentinel™'s software and the three laser beams are directed to the defined position. During the CT image acquisition, the couch is moved through the CT, and thus the laser projected by the Sentinel™ must follow the couch's movement. This is done by connecting Sentinel™ with another laser system installed behind the CT. The position of the couch is sent to the Sentinel™, which thereby continuously redirects the laser to follow the couch position throughout the scan.

3.5.3 Treatment

During DIBH treatment, the OSS system monitors the surface, the isocenter position and the breathing motion (figure 4). The OSS system has beam control via an interface with the linac, so that the beam is automatically gated. Beam control is triggered by the tolerances for the surface and/or calculated isocenter motion during treatment delivery set in the template. Also, the breathing motion is triggering the beam while entering or exiting the gating window.

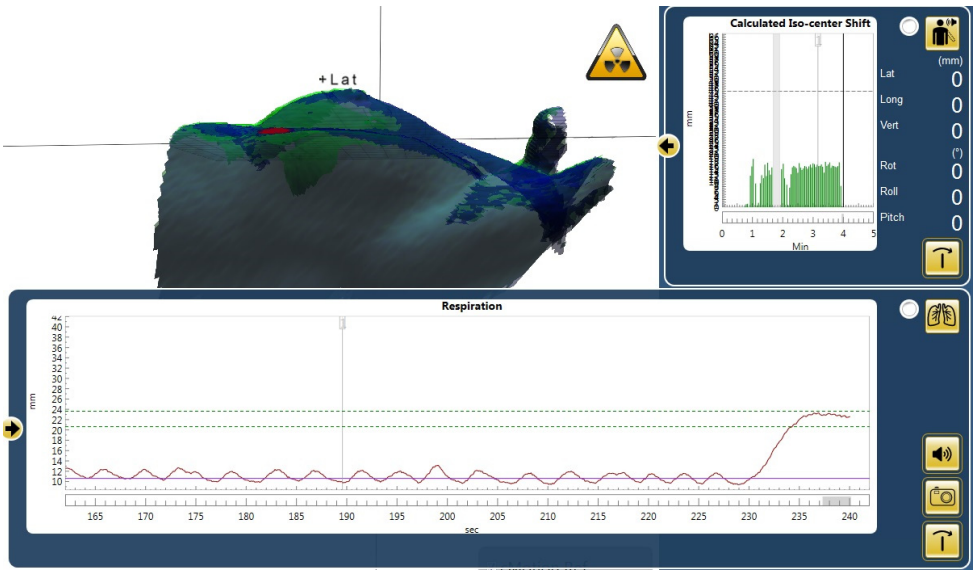

Figure 4. Patient surface imaging (SI) during a deep inspiration breath hold (DIBH) breast cancer radiotherapy treatment. The red marker on the xiphoid process shows the region-of-interest (ROI) that is tracking the patient's breathing motion. In the window "Calculated isocenter shift" the green bars show calculated isocenter position during the treatment, and also, the live values are presented in the right side of the window. In the window "Respiration", the purple line shows the baseline, the green dotted lines show the gating window and the red curve shows the tracked breathing motion in the ROI.

3.6 Linac integration with beam control

The OSS system is interfacing with the linac control to interrupt the beam delivery if the patient motion exceeds the tolerance for the treatment position. For treatments that are delivered in DIBH, the beam is interrupted several times during a single treatment delivery. This requires that the linac must be able to switch between beam-on and beam-off quickly, so that radiation dose is not delivered outside the planned position. According to the American Association of Physics in Medicine (AAPM) Task Group Report 142, the latency of beam-on/-off should be within a 100 milliseconds (ms) for a linac with synchronization of the radiation beam with the patient's respiratory cycle [60]. The new modern OSS systems can be installed on older linacs, however, these linacs were not designed for this type of gated beam delivery. Thus, accurate control of the linac performance is required.

3.7 Statistics

Statistical tests are carried out to evaluate if there is a difference between the means or medians in sets of data, or if the difference occurred by chance. The scaling term and the type of distribution of the data to be tested has to be determined. If two sets of data are of normal distribution with a known scaling term, a parametric test (e.g. Student t-test) can be carried out. If one or both of the data sets have a skew distribution, a non-parametric test (e.g. Wilcoxon test or Mann-Whitney U test) should be carried out. If the data is paired or not needs also to be determined since both parametric and non-parametric tests can be used for unpaired and paired data.

For multiple non-parametric distributions, a Friedman test can be carried out to find significant differences. If significant difference is found, a post hoc paired Wilcoxon test can be carried out between the two distributions. Multiple variable testing increases the risk of finding a difference by chance, and therefore a more stringent significance level should be considered.

In this thesis following statistical tests were used:

Students t-test (**study I**, **study IV**)
Wilcoxon test (**study II**, **study IV**, **study V**)
Mann-Whitney U test (**study V**, **study VI**)
Friedman test (**study III**)

4. Quality assurance

The general concept of QA related to non-radiographic systems was introduced in the AAPM task group report (TG)-147 [22] in 2012. Quality assurance recommendations specific to SI included beam-latency characterization, however, a lack of a standardized method was described. No commercial tool was available to evaluate the beam latency time for gated beams, and additional requirements were that the tool was operational for several linac models and manufacturers. Also, a new QA for the SI system specific calculation algorithms for positioning accuracy needed to be investigated in order to understand the applications of this technology. New necessary QA tests unique for SI systems were developed in **study I** and **study V**.

4.1 Beam latency characterization for gated beams

Beam latency time should be small, <100ms, to ensure safe beam delivery for gated treatments [60]. To be able to measure these small time spans a moving phantom connected to a microcontroller unit (MCU) was in-house developed at the Skåne University Hospital in Lund (**study I**). The requirements were that the motion of the phantom should be fast, to simulate a binary pattern, for a fast beam-on and beam-off signal and to be able to determine the latency times accurately (figure 5). The phantom developed consisted of a spring loaded solenoid with a metal shaft. The 24 Volt direct current (V dc) solenoid was energized and de-energized using the MCU to create a binary motion. On top of the phantom a gating marker block (Varian Medical Systems) was placed. The marker block position was detected by an infrared camera (Polaris Spectra, Northern Digital Medical). On the linac (TrueBeam, Varian Medical Systems, Palo Alto, CA) the beam pulses were measured using the accelerators internal signal of the current produced across the target. However, this signal is not possible to extract from other vendors than Varian, hence, a PIN (p-type, intrinsic type, n-type) diode was placed in the radiation beam as a second independent measurement to evaluate if this method could be a universal solution for measuring beam latency times. Measurements were carried out for 6 MV and 10 MV, with a dose rate of 600 MU/min.

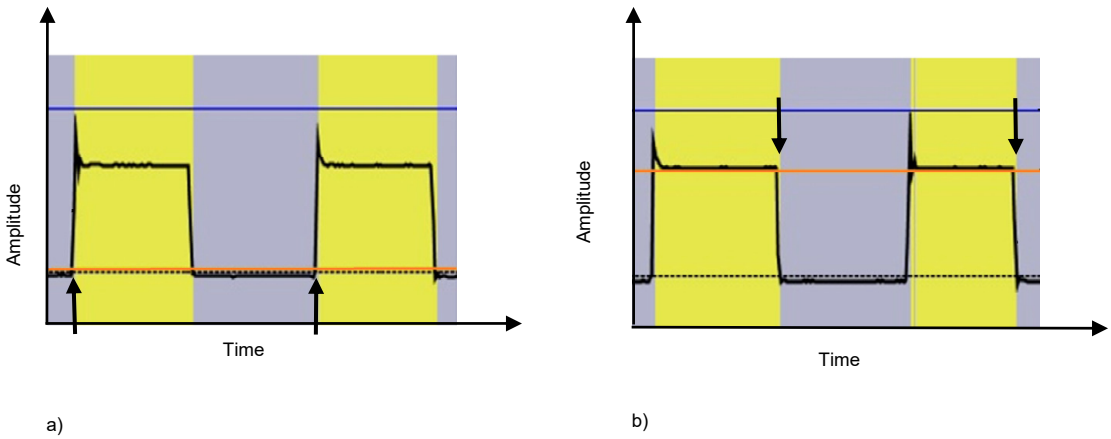

Figure 5. Schematic image of the latency measurements. The signal (black) shows the recorded binary pattern by the infra-red camera. The orange line shows the position of the beam triggering. The yellow fields symbolize the beam-on signal. In figure ***a)*** the beam-on latency is measured with the orange triggering position close to the start of the binary signal. The arrows show where the measurements were carried out. In figure ***b)*** the orange triggering line is close to the start of the beam-off signal. The arrows show where the measurements were carried out.

In **study I**, the latency measurements were carried out 50 times per beam-on and beam-off signal, respectively (figure 5a and b). The measurements were carried out with an Atmega328P microcontroller unit (Atmel™, CA, USA), equipped with three timers. The highest possible time resolution (62.5 ns) were used and considered small compared to the time scale (ms) measured. The latency times measured in **study I,** using both the beam pulses and the PIN diode showed a small beam–on (2.2±1.1 ms) and slightly larger beam-off (57.7±10.1 ms) latency. However, the beam-on signal was much smaller than the beam-off signal, which is unfortunate in a DIBH treatment situation where the delay in the beam-off would cause dose delivery while the patient position is outside the gating window. Still, the small beam-off latency measured in this study would in a clinical situation translate into that the target would be located outside the gating window, by approximately 1 mm during a speed of 20 mm/sec. The latency time should be considered if more advanced gating treatments with multiple beam interruptions are to be delivered, and if higher dose rates would be used. The latency measurements could also be carried out over time to investigate the performance of the linacs, as they age. The results from this study showed that we safely could deliver DIBH treatments to our patients with regards to the beam latency times. In **study I**, one of the drawbacks was that only measurements with the gating marker block were included. However, technical advancement later also enabled beam latency characterization using SI. Ideally, the SGRT systems provides real-time imaging while encompassing the imaging, image reconstruction, image registration and image post-processing chain. In practice, the frame-rate specified for the camera hardware might

not reflect the overall performance, which require latency measurements to be carried out. The QA tool in **study I** has been used to evaluate the beam latency for the several linacs at our depatment, and showed an important role when tuning an older linac into gating mode.

The characterization of the latency times in **study I** was an important step towards the clinical use of DIBH in **study II** and **study III**.

4.2 Validation of the image registration algorithms

The accuracy of the image registration algorithms is commonly evaluated using rigid phantoms in various positions and with various shapes [61]. The Catalyst™ is today the only OSS system that has a DIR algorithm implemented (described in section 3.2 Image registration algorithms), and hence, a new approach was developed in order to evaluate the accuracy of the calculation for deformed surfaces. In **study V**, an anthropomorphic thorax phantom was in-house build at the University of Florence, with the ability to flex and be deformed (figure 6).

Figure 6. Anthropomorphic thorax phantom in different deformed positions, and a 3 dimensional model of the internal structures used for cone beam computed tomography verification.

Rigid image registration (RR) was compared to DIR, using either a reference surface extracted from the TPS or an online captured reference surface by the OSS system. The phantom was positioned using a Catalyst™ HD system, and to verify the phantom position a CBCT was matched with a CT of the phantom as the gold standard. Four

different internal targets were evaluated for all the displacements and deformations for both RR and DIR. The results in **study V**, showed that when the phantom was positioned in different positions on the treatment couch without any deformation applied, the DIR and RR algorithm showed similar accuracy in the positioning calculation. However, when anatomical deformations were applied to the phantom the DIR showed a significant improved positioning accuracy in lateral (lat) direction, lng direction, and pitch ($p < 0.05$) compared to RR. For all four targets and deformations, the mean positioning accuracy was improved from 1.9(±1.5) mm and 1.1(±0.8) mm to 1.1(±1.2) mm and 0.6(±0.5) mm in lat and lng directions, respectively, and from 0.8°(±0.6°) to 0.4°(±0.4°) in pitch, using DIR compared to RR.

In one case, the stomach volume was enhanced on the phantom while the target was stuck to bony anatomy. In that case, the RR image registration reached out of its capabilities and was not able to provide a calculation result. The DIR image registration could calculate a result, however, the surface did not represent the target position, and hence, the CBCT match showed a larger shift. This highlights the importance of understanding the limitations of the image registration. In a SGRT clinical workflow the system has to be able to calculate positioning result for all patients, however, in the presence of large deformations SI has to be combined with 3D volumetric imaging. In **study V**, we found that the DIR accurately calculates the position even in the presence of deformations, however, larger deformations contributes with uncertainties in the image registration and needs to be combined with other imaging modalities. The findings in **study V** has been considered in the clinical workflow in two ways; a colour map which highlights deformations larger than 5 mm and cropping of anatomical topography that commonly deforms during RT. Both these strategies have been applied in **study II**, **study IV** and **study VI**.

5. Surface guided patient positioning

The clinical paradigm shift from 3-point localization to SGRT required thorough investigation, both with regards to accuracy and overall workflow. In **study IV** and **study VI**, SGRT was investigated for breast and prostate cancer patients which are the two largest patient groups receiving RT in Sweden [1].

5.1 Patient selection

In **study IV**, 63 patients receiving tangential treatment after breast conserving surgery and 76 patients with locally advanced breast cancer receiving locoregional treatment after mastectomy or breast conserving surgery were enrolled. The median age was 62 years (range: 34-83 years) for patients receiving tangential treatment and 64 years (range: 33-87 years) for the breast cancer patients receiving locoregional treatment, respectively. In **study VI**, a total of 40 localized prostate cancer patients with gold fiducial markers implanted at least two weeks prior to start of radiotherapy treatment were enrolled.

5.2 Target delineation

In **study IV**, target delineation and treatment planning were performed according to the Swedish national guidelines from the Swedish Breast Cancer Group [62]. For the prostate patients in **study VI**, the target delineation followed the HYPO-RC-PC trial [63], thus the CTV was delineated with MR guidance and included the prostate only. All patients had an isotropic 7 mm CTV to PTV margin.

5.3 Treatment planning

3D-CRT treatment plans were created for both the tangential and locoregional treatments, in **study IV**. For the tangential treatment, two opposing tangential 6 MV fields to cover the breast tissue and supplementary fields or wedges for dose homogenization purposes were used. The isocenter was placed central in the breast tissue. For the locoregional treatments, opposing tangential fields to cover the breast tissue and additional 6MV anterior-posterior (AP) field and a 10 MV posterior-anterior (PA) fields were used to cover the locoregional axillary lymph nodes. Also, a supplementary 10 MV PA field was used shielding for the lung tissue. The treatment isocenter was positioned in the junction between the tangential and AP-PA fields. For mastectomy patients, a 0.5 cm thick and 6 cm wide bolus (Superflab, Mick Radio-Nuclear Instruments, Inc. An Eckert & Ziegler BEBIG Company) was placed over the operation scar.

In **study VI**, 6 MV FFF VMAT treatment plans were created for each patient. The treatment was delivered in 7 fractions, every other day, with a total absorbed dose of 42.1 Gy, delivered with a TrueBeam linear accelerator (ver 2.5, Varian Medical Systems, Palo Alto, CA).

5.4 Assessment of inter fraction motion

In **study IV**, all patients were initially aligned to a three point based tattoo setup, whereas in **study VI** this procedure was only done during the first treatment fraction. In both **study IV** and **study VI**, the patient positioning was carried out either with 3-point localization or SI for comparison purposes. The surface tolerance for the patient posture in the SI group were 5 mm (figure 7) in both studies.

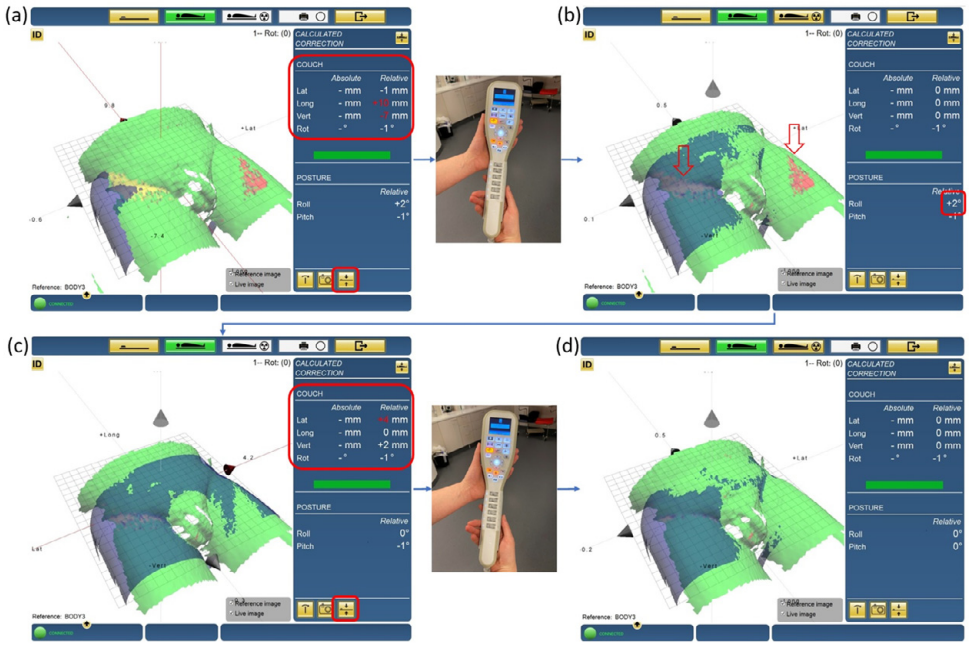

Figure 7. Patient setup procedure using a surface imaging (SI) workflow for a hypofractionation prostate patient. The blue and green surfaces are the reference and live surfaces, respectively. Initially, the couch was shifted to isocenter position using saved couch parameters. The shift indicated by Catalyst™ (lat -1 mm, lng +10 mm, vrt -7 mm) **(a)** was then applied using the Auto-Go-To function. The color map and the positioning result indicated a roll **(b)**, which was corrected for by asking the patient to adjust himself. Once the roll was corrected for, residual translations (lat +4 mm, lng 0 mm, vrt +2 mm) **(c)** were applied using Auto-Go-To into the correct treatment position **(d)**.

In **study IV,** the tolerance for patient positioning was set to ≤2 mm in all translational directions (vrt, lat and lng) and ≤3° in all rotational directions (rotation (rot), roll and pitch). In **study VI**, the aim was to use the Auto-Go-To function integrated to the linac to achieve a SI guided setup close to zero in all translations and rotations. In both **study IV** and **study VI**, the isocenter position was drawn onto the patient's skin, using room lasers and skin marker pens for the patients using 3-point localization. The patient positioning was evaluated using on-board imaging for all patients included. In **study IV**, a total of 677 and 632 verification images for tangential treatments and locoregional treatments were included, respectively, and in **study VI**, 240 verification images were included.

The inter fraction motion in lat, lng and vrt direction, respectively, and the total vector offset v, were evaluated (eq. 1).

$$v = \sqrt{lat^2 + lng^2 + vrt^2} \quad (1)$$

In **study IV**, a comparison between a single camera and a three camera scanning system was carried out for the locoregional treatments. Comparison of the vector offset using 3-point localization and SI for both tangential and locoregional treatments and the use of a single camera scanning system compared to a three camera scanning system was carried out using a two-sided Wilcoxon sum rank test with a significance level of 0.01. In **study IV** and **study VI**, SI guided setup significantly improved the patient setup for patients receiving tangential and locoregional breast cancer treatments, as well as for prostate cancer patients receiving ultra hypofractionation treatment, compared to laser based setup ($p<0.01$) (figure 8a, b, d).

In **study IV**, the median vector offset was 4.2 mm (range: 0-19.7 mm) and 4.7 (0-18.7 mm) for tangential and locoregional treatments, respectively, using 3-point localization. A significant improvement in patient setup was observed using SI ($p<0.01$), hence, the median vector offset was reduced to 2.4 mm (range: 0 – 8.1 mm) and 4.0 (range: 0 -13.5 mm) for tangential and locoregional treatments, respectively (figure 8a and b). Comparison of a single camera system to a three camera system for locoregional treatments showed a small, but not significant difference ($p=0.02$) (figure 8c). In **study VI**, the median vector offset was decreased from 5.2 mm (range: 0.41 – 17.3 mm) for 3-point localization to 4.7 mm (range: 0 – 10.4 mm) for SI ($p= 0.01$). For SI, only a single fraction had a total vector offset larger than 10 mm, whereas the corresponding number for 3-point localization was 14 fractions.

For breast cancer patients, improvements in patient setup using SI could potentially lead to reduced amount of verification imaging, and hence, less imaging dose to the patients. The surface tolerance of 5 mm highlighted patient posture errors that the therapists manually corrected for. In **study IV**, posture errors larger than 5mm were in some cases observed as a displacement of the arm position. Due to stiffness in the arm or shoulder the posture could not be corrected for, which led to larger setup deviations. For the prostate patients, the use of the colour map mitigated the RTTs' subjectivity on the accuracy of the patient setup, hence the SI system works as an operator-independent check for the patient setup. In both **study IV** and **study VI**, potential patient motion in the time span between patient positioning and verification imaging could have contributed to a reduced setup accuracy. In **study IV**, degraded SI quality was observed for a few patients, due to nonoptimal camera settings. For locoregional treatments degraded SIs was more pronounced compared to tangential treatments, due to the lower pitch the patients were positioned in and the use of bolus. The bolus was in all cases overexposed, leading to a loss of surface over the isocenter position which is disadvantageous for the DIR due to the loss of the most important surface for the isocenter position calculation. Setup deviations up to 11 mm were observed using SI for locoregional treatments, which has also been reported by Stanley et al. [30].

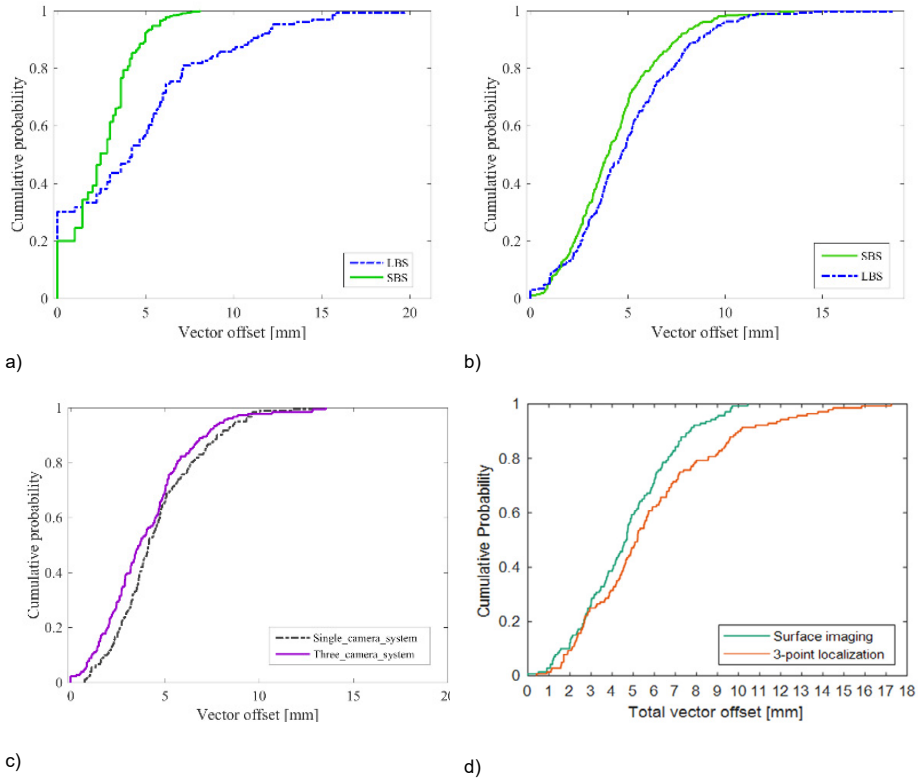

Figure 8. Setup deviation for breast cancer patients receiving ***(a)*** tangential treatment, ***(b)*** locoregional treatment and ***(d)*** hypofractionation prostate cancer patients using 3-point localization (LBS) and surface imaging (SBS). The cumulative probability of the vector offset showed a significantly improved patient setup using a surface image guided workflow for all patients ($p<0.01$) ***(c)***. For the breast cancer patients receiving locoregional treatment, patients were positioned using a single camera and a three camera system. The cumulative probability of the vector offset show a non-significant improved patient setup for three camera compared to single camera system ($p=0.02$).

5.5 Setup time for surface guided radiotherapy

The initial motivation for implementing SGRT was to replace lasers and skin marks for patient positioning [64], as shown effective in **study IV** and **study VI**. Further the time efficiency using a SGRT workflow was investigated in **study VI**, using the time-stamped log files in ARIA for the tags of "in-room lasers on" or "start moving the couch", whichever occurred first, and "image acquisition" as an end-point. The median setup time was reduced from 3:28 min (range: 1:42 – 12:57 min) using 3-point localization to 2:50 minutes (min) (range: 1:32 – 6:56 min) using SGRT ($p < 0.001$) (figure 9). On average the setup time decreased with 49 s for each fraction, which shows that a SGRT not only increase the accuracy of the patient initial setup, but also provide a time effective workflow. The time reductions observed could potentially lead to a

higher patient comfort since the maximum setup time was reduced from 12:57 min to 6:56 min and reduced risk of wrongful treatment due that prostate motion increase linearly over time for all prostate cancer patients [19].

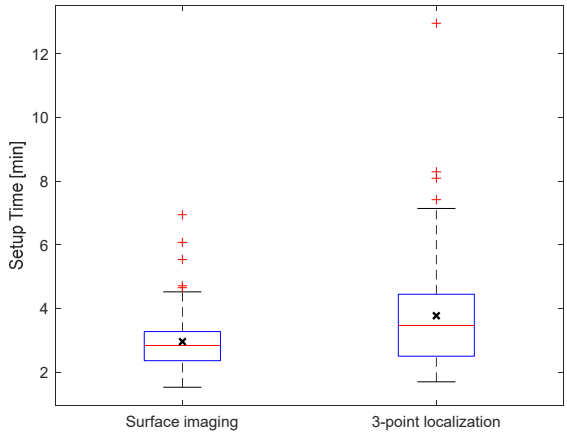

Figure 9. Setup time for surface imaging (SI) and 3-point localization setup for ultra-hypofractionated prostate cancer radiotherapy treatment. The red horizontal lines represent the median setup time, the black crosses show the mean setup time and the red plus signs are outliers.

6. Surface guided breathing adapted radiotherapy

The respiratory motion primarily affects the tumour sites in the thorax and abdomen, which addresses the urges for management of the respiratory motion [65]. In **study II** and **study III**, treatment in DIBH were investigated for both left sided breast cancer and HL. For left sided breast cancer patients, the isocenter position was tracked using SI during DIBH to evaluate the reproducibility. With the new technical advancements using SI in combination with scanned proton beam RT, the possible dosimetric benefits for HL treated in DIBH were investigated.

6.1 Patient selection

In **study II**, a total of 40 patients receiving radiotherapy for left-sided breast cancer in DIBH were enrolled. 20 patients received tangential treatment after breast-conserving surgery and 20 patients received locoregional treatment after either breast-conserving surgery or mastectomy. The median age was 59 years (range: 45-77 years) for the group receiving tangential treatment and 46 years (35-85 years) for the group receiving locoregional treatment.

In **study III**, 18 patients (10 females and 8 male) with mediastinal HL were enrolled. The disease location was i) mediastinum above the diaphragm (3 pts), ii) mediastinum and supraclavicular fossa (5 pts), iii) mediastinum, supraclavicular fossa and neck (7 pts) and iv) mediastinum, supraclavicular fossa, neck and axilla (3 pts). The median age was 34 years (range: 15-71 years).

6.2 CT acquisition

In both **study II** and **study III** all patients underwent CT data acquisition in FB and in DIBH, for comparison purposes. For all patients in **study II**, the Sentinel^{TM} with visual guidance was used at the CT to acquire the DIBH CT set. In **study III**, the first ten

patients was audio-coached into enhanced inspiration breath hold (EIG) using the real-time positioning management system (RPM™, Varian Medical Systems, Palo Alto, CA) consisting of a marker block and infrared camera, which has been described elsewhere [66]. For the last nine patients included in the study, the Sentinel™ with visual and audio guidance was used. Both deep inspiration techniques result in a CT set in deep inspiration. For all patients, the bony anatomy above the xiphiod process was used as a surrogate for the target position. In the Sentinel™ software, the patients surface was scanned in the FB reference position for patient positioning purposes. A ROI, shaped as a circle with a 2 cm diameter was placed on the xiphiod process to track the breathing motion.

6.3 Target delineation

Target delineation was carried out in the TPS (Eclipse, Varian Medical Systems, Varian). In **study II** and **study III**, the lung tissue was automatically delineated using the segmentation wizard and then manually verified. To reduce inter-observer variability, all other structures were delineated by the same radiation oncologist in both the FB and DIBH CT sets. In **study II**, the PTV and CTV-T were delineated in the treatment planning CT set. No CTV-T was delineated for patients that had received mastectomy. The OARs delineated were the heart, left anterior descending coronary artery (LAD) and the ipsilateral lung. In **study III,** the PTV and CTV were delineated using the involved site radiotherapy (ISRT) technique [67]. Information from a 18F-fluoro-deoxyglucose (FDG) positron emission tomography (PET)/CT image acquired during FB (GE Discovery 690, General Electric Healthcare and Philips Gemini TF 16, Philips Medical Systems) was visually transferred to the FB and DIBH planning CTs. The PTV was defined as the CTV with an 8 mm isotropic margin, cropped 4 mm from the skin surface for all patients and treatment plans. The OARs delineated were the heart, LAD, lung and female breasts.

6.4 Treatment planning

All treatment plans in **study II** and **III** were created in the Eclipse TPS (Varian Medical Systems, Palo Alto, CA). Photon treatment plans were created for all patients in **study II** and **III** and the dose was calculated using the anisotropic analytic algorithm. Also, in **study III** IMPT treatment plans were created for an IBA PT System (Proteus Plus, IBA, Louvain-la-Neuve, Belgium) with a pencil beam scanning (PBS) beam delivery in the TPS. Beam data from the Swedish Proton Center the Skandion Clinic (Uppsala,

Sweden) was used in the Proton Convolution Superposition algorithm (PCS, version 13.7) for dose calculations.

In **study II**, the prescribed dose was 50 Gray (Gy) in 25 fractions, normalized to the PTV mean dose in for both the patients receiving tangential and patients receiving locoregional treatments for comparison purposes. In **study II**, the treatment plans were created to fulfil the national guidelines from the Swedish Breast Cancer Group [62]. For all patients, treatment plans were created for both DIBH and FB. For comparison purposes between FB and DIBH only minor differences in the beam arrangement were allowed to achieve comparable target coverage.

In **study III**, photon and proton treatment plans were created in both FB and DIBH for patients with mediastinal HL. 3D-CRT and VMAT was used for photon treatment planning and IMPT for proton treatment planning, resulting in six treatment plans for each patient. For all treatment plans, the prescribed dose was 29.75 Gy/Gy(RBE) (relative biological equivalent) in 17 fractions normalized to the mean dose of the PTV, with a RBE of 1.1 for protons. The main goal was to cover 100% of the PTV volume with 95% of the prescribed dose, while keeping volumes receiving >105% as low as possible. Each treatment plan was individually optimized to achieve the required PTV coverage and sparing of dose to the OARs.

For the 3D-CRT plans, two 6 MV AP/PA parallel opposed fields were generally used with supplementary fields or wedges for dose homogenization purposes. 6 MV VMAT plans using two, three or four (1 pts) arcs to fulfil optimal target coverage while sparing OARs. Full arcs with collimator angles 5 and 355° were typically used, the arc length was modified if it would cause patient or couch collision. For the IMPT plans, two beam arrangements were used, either AP/PA or two oblique AP fields in 10 and 350° and the plan considered to best fulfil the target coverage while sparing the OARs was chosen. An additional margin for the range uncertainty was calculated as 3.5% of the range to the distal edge of the CTV plus 1 mm. If the range uncertainty exceeded the CTV-to-PTV margin of 8 mm, an additional margin was added (1 pts in FB and 4 pts in DIBH). Otherwise the same PTV as for the photon plans was used.

6.5 Assessment of intra fraction motion

In **study II**, the patient monitoring (described in section 3.4) was used to assess the intrafractional motion of the isocenter position during the DIBH treatment. For all patients included in the study the three camera OSS system was used. Since the patients were treated using DIBH, both the respiratory monitoring and the patient monitoring were active simultaneously. In the beginning of the treatment the respiratory baseline

was determined as the expiration position during FB. The signal of the breathing motion was tracked at the surface above the xiphoid process (figure 10a and b). During the treatment session a daily reference image was captured in the middle of the gating window. The reference image was matched with the live SI during the treatment delivery. To assess the calculated isocenter shift during DIBH the log files from the OSS system were extracted. The intrafractional isocenter reproducibility was calculated as the difference between the average isocenter positions during beam-on for two DIBHs during a treatment session. For each patient, the isocenter reproducibility was retrieved for five treatment sessions. In total, 195 DIBHs for tangential treatments and 195 DIBHs for locoregional treatments were included in the study. The intra fractional motion of the patient isocenter position during DIBH was used to shift the dose plans, to carry out an evaluation of the dosimetric effects.

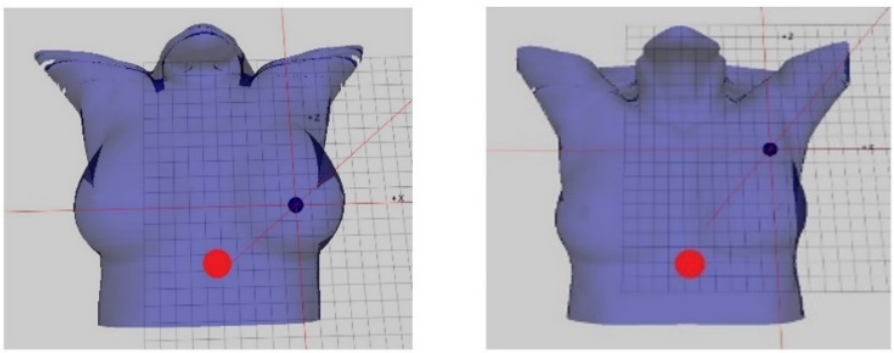

a) b)

Figure 10. The signal of the breathing motion was tracked in the region-of-interest (red marker) on the surface above the xiphoid process for both ***a)*** patients receiving tangential treatment and ***b)*** locoregional treatment. The position of the region-of-interest was used as a surrogate for the target position. The back sphere shows the treatment isocenter position for both treatment types.

6.6 Dosimetric analysis and statistical tests

In **study II** and **study III**, the dose volume histogram (DVH) from all treatment plans for each patient were extracted from the TPS. Average DVHs were calculated for all treatment techniques for comparison purposes. In **study II**, the treatment techniques used were FB-3DCRT and DIBH-3D-CRT. Also, the intrafractional motion was applied to the treatment plans to evaluate the dosimetric effects. In **study III**, all possible combination of breathing- and radiation delivery techniques, i.e. FB-3D CRT, DIBH-3D CRT, FB-VMAT, DIBH-VMAT, FB-IMPT and DIBH-IMPT, were used for each patient, respectively. To compare the dose distributions for the different

treatment techniques in **study II** and **study III**, several dosimetric parameters were evaluated. In both **study II** and **study III**, the mean dose to the heart ($D_{mean,heart}$), LAD ($D_{mean,LAD}$) and the dose received by 2% of the volume for the heart ($D_{2\%,heart}$) and LAD ($D_{2\%,LAD}$) were evaluated. In **study II**, the volume receiving 20 Gy for the ipsilateral lung ($V_{20Gy,lung}$) and the dose received by 98% of the PTV volume ($D_{98\%,PTV}$) were retrieved from the TPS. In **study III**, the mean dose to the lungs ($D_{mean,lungs}$), the lung volume receiving 5 and 20 Gy ($V_{5Gy,lungs}$ and $V20_{Gy,lungs}$), the mean dose to the right breast ($D_{mean,right\ breast}$) and mean dose to the left breast ($D_{mean,left\ breast}$) were included. In **study III**, the CTV and PTV volume covered by 95% of the prescribed dose ($V_{95\%,CTV}$ and $V_{95\%,PTV}$) were evaluated. In **study III**, a heterogeneity index (HI) was calculated to compare the PTV dose uniformity (eq. 2) [68].

$$HI = \frac{D_{2\%} - D_{98\%}}{D_{mean}} \quad (2)$$

where $D_{2\%}$ and $D_{98\%}$ are the doses to 2% and 98% of the volume.

To compare the healthy tissue dose between the treatment techniques used, the integral dose was calculated (eq. 3).

$$ID = \rho \cdot V \cdot D_{mean} \quad (3)$$

where the V is the full CT scanned body volume minus the PTV volume, ρ is the tissue density with correction for the lung tissue density. Generic density values of 0.26 g/cm^3 and 1.06 g/cm^3 were used for the lung and all other tissues, respectively [68].

For comparison of the plan conformity, the Paddick's conformity index was used (eq. 4) [69].

$$CI_{Paddick} = \frac{TV_{PIV}^2}{TV \cdot PIV} \quad (4)$$

where TV is the target volume, PIV is the prescription isodose volume and TV_{PIV} is the target volume covered by the prescribed isodose level.

In **study II** and **study III**, treatment in DIBH generally showed beneficial dosimetric effects for the OARs investigated compared to FB. However, for individual cases an increased dose to OARs were observed in both **study II** and **study III.**

In **study II**, two-sided paired Wilcoxon tests were carried out to investigate if the differences between DIBH and FB were statistically significant, using a significance level of 0.05. Treatment in DIBH significantly reduced the median mean dose to the heart, LAD and lungs, as well as $D_{2\%}$ to the heart and LAD, while maintaining the

target coverage, for both tangential and locoregional treatment. The dose to the OARs were reduced for all dose levels (figure 11a and b). An increased $D_{mean,heart}$, $D_{2\%,heart}$, $D_{mean,LAD}$, $D_{mean,lung}$ and $V_{20Gy,lung}$ was observed for a few individual cases for DIBH compared to FB. Further dosimetric details can be found in **study II**. For 90% of the DIBHs, the intrafractional DIBH isocenter reproducibility was within 3.2 and 2.3 mm for tangential and locoregional treatments, respectively (figure 12a and b). The maximum values of the DIBH isocenter reproducibility were 5.4, 5.3 and 3.8 mm (lat, long, and vrt) and 3.4, 5.6 and 2.7 mm, for tangential and locoregional treatments, respectively (figure 12a and b). The dosimetric effect of applying the intrafractional isocenter shifts resulted in degraded target coverage and increased dose to OARs. For example, the median $D_{mean,heart}$ increased from 0.71 Gy to 0.84 Gy when applying the shift observed for the 90% level, for tangential treatments (figure 13a). The corresponding value for locoregional treatments were 1.34 to 1.75 Gy (figure 13b). An even larger increased dose was observed for the maximum shifts, however, unlikely to have any major clinical relevance since it is a worst-case scenario only observed for a few percent of the DIBHs.

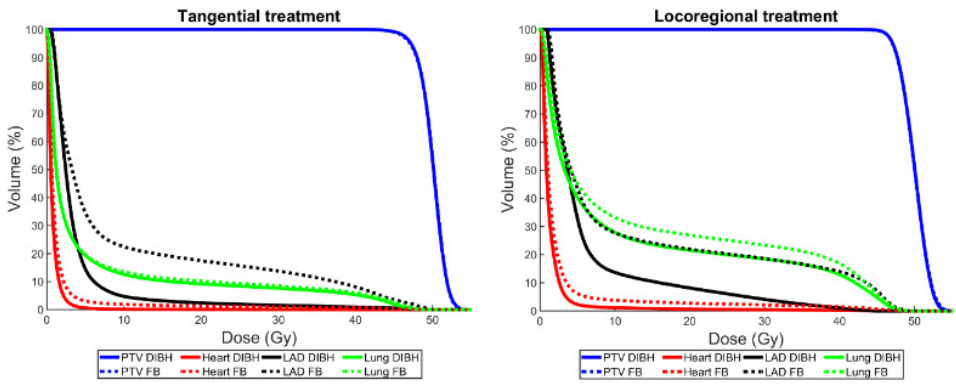

Figure 11. Average dose volume histograms for tangential ***(a)*** and locoregional ***(b)*** treatment for the heart (red), left anterior descending coronary artery (LAD) (black), ipsilateral lung (green) and PTV (blue) comparing deep inspiration breath hold (DIBH, solid lines) and free breathing (FB, dashed lines).

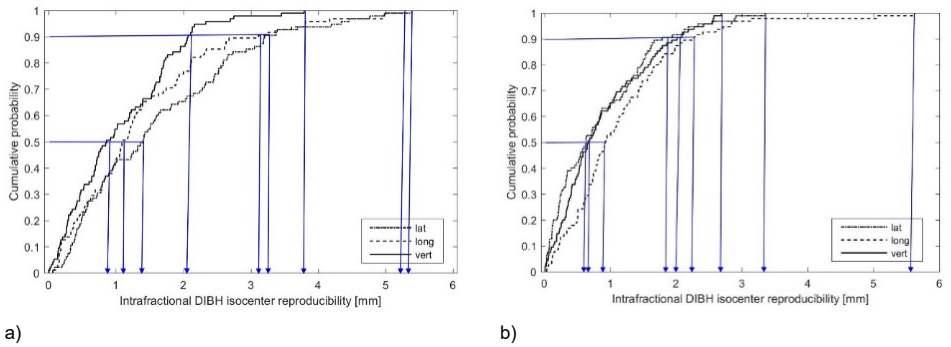

Figure 12. Cumulative probability of the intrafractional deep inspiration breath hold (DIBH) isocenter reproducibility for the tangential treatment ***(a)*** and locoregional treatment ***(b)***. The intrafractional DIBH isocenter reproducibility in lat, long and vrt directions corresponding to the cumulative probability of 50%, 90% and maximum value are marked with blue arrows.

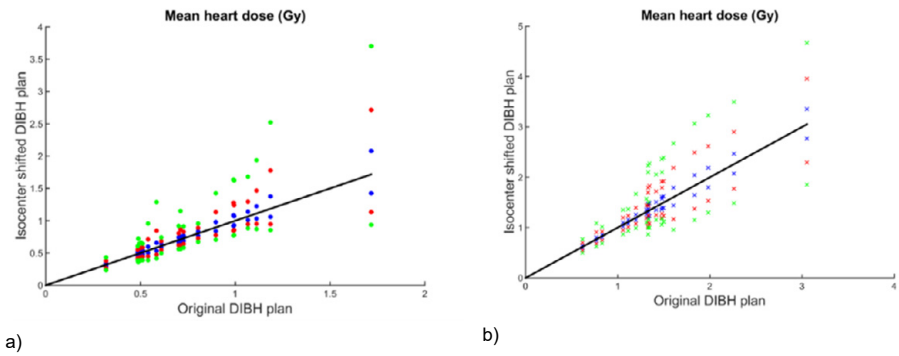

Figure 13. The minimum and maximum values of $D_{mean,heart}$ for the isocenter shifted deep inspiration breath hold (DIBH) plans versus the original DIBH plans. The results are presented for each individual patient receiving tangential treatment ***(a)*** and locoregional treatment ***(b)*** and for all three cumulative probability levels, 50% (blue), 90% (red) and maximum (green). The lines are for illustration purpose only, and represent where the dosimetric parameters are equal for the isocenter shifted and original DIBH plans.

In **study III**, for the majority of the patients the dose to the OARs was reduced for DIBH compared to FB within the same treatment planning technique (3D-CRT, VMAT and IMPT) (figure 14a, b and c). Comparison of the six different treatment techniques was carried out using a Friedman test. If a statistically significant difference was found, a post hoc two sided paired Wilcoxon test were carried out with a significance level of 0.05. Treatment in DIBH reduced the lung dose for the vast majority of the patients, however, a larger variety in the dose to the heart and LAD was observed (figure 14b and c).

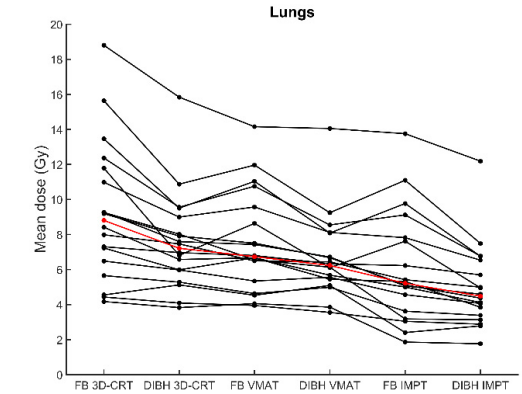

a)

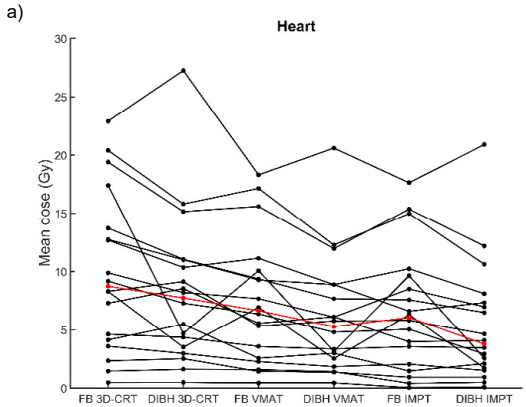

b)

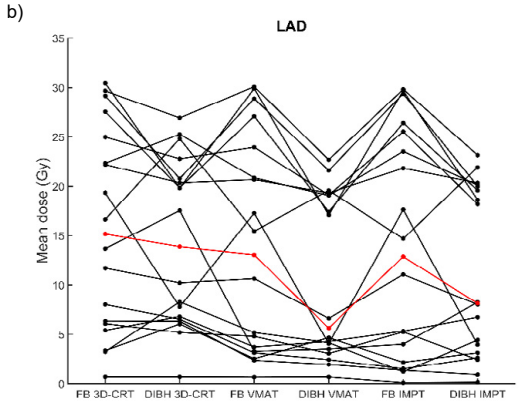

c)

Figure 14. The mean dose to the ***(a)*** lungs, ***(b)*** heart, ***(c)*** LAD, for free breathing (FB) 3-dimensional conformal radiotherapy (3D-CRT), deep inspiration breath hold (DIBH) 3D-CRT, FB volumetric modulated arc therapy (VMAT), DIBH VMAT, FB intensity modulated proton therapy (IMPT) and DIBH IMPT. The values for each individual Hodkin's lymphoma patient are shown in black and the median values for the whole patient cohort in red.

In a few cases, increased heart and LAD doses were observed for treatment in DIBH (figure 14 b and c). The possible reason for this effect was that the heart position shifted during the DIBH into a disadvantageous position in relation to the treatment fields, compared to the heart position in FB. The dose to the female breasts showed no significant difference comparing FB with DIBH (table 1). Improved target coverage, reduced ID and reduced dose to OARs were observed for IMPT. Overall, the most beneficial combination was DIBH IMPT. However, if only photon therapy is available DIBH VMAT showed improved target coverage, higher conformity, and generally lower doses to the OARs, except the female breasts where no significant difference were observed, compared to 3D-CRT (table 1). Of a clinical interest, a comparison of FB IMPT and DIBH VMAT was carried out, since PT was not locally available. The median $D_{mean,lungs}$ and $D_{mean,heart}$ showed no significant difference. Significant differences were observed in favour of DIBH VMAT in $V_{20Gy,lungs}$ and $D_{mean,LAD}$ (table 1). However, FB IMPT showed significantly lower doses to $V_{5Gy,lungs}$, $D_{mean,\ right\ breast}$ and $D_{mean,\ left\ breast}$ (table 1).

Table 1. Dosimetric parameters for free breathing (FB) and deep inspiration breath hold (DIBH) 3-dimensional conformal radiotherapy (3D-CRT), volumetric modulated arc therapy (VMAT) and intensity modulated proton therapy (IMPT). The data are presented as median value and range, with the results of the Friedman and pairwise Wilcoxon tests.

Parameter	FB 3D-CRT	DIBH 3D-CRT	FB VMAT	DIBH VMAT	FB IMPT	DIBH IMPT	p-value Friedman
$V_{95\%,\,CTV}$ (%)	97.7 [90.9-100.0]^{c,d,e,f}	97.3 [91.1-99.9]^{c,d,e,f}	100.0 [100.0-100.0]^{a,b,e,f}	100.0 [100.0-100.0]^{a,b,e,f}	99.9 [97.8-100.0]^{a,b,c,d,f}	99.6 [98.4-100.0]^{a,b,c,d,e}	<0.001
$V_{95\%,\,PTV}$ (%)	91.9 [85.3-99.2]^{c,d,e,f}	90.2 [84.7-98.5]^{c,d,e,f}	98.0 [96.1-99.5]^{a,b,e}	98.0 [96.5-99.2]^{a,b,e}	99.1 [97.2-99.8]^{a,b,c,d,f}	98.8 [96.1-99.7]^{a,b,e}	<0.001
HI_{PTV} (%)	14.1 [8.8-18.9]^{c,d,e,f}	15.0 [9.2-17.6]^{c,d,e,f}	7.7 [5.5-9.9]^{a,b,e}	7.8 [5.7-10.0]^{a,b,e}	6.3 [4.3-9.5]^{a,b,c,d,f}	7.5 [4.2-11.3]^{a,b,e}	<0.001
$D_{mean,Heart}$ (Gy/Gy(RBE))	8.8 [0.5-22.9]^{c,d,e,f}	7.7 [0.5-27.3]^{d,e,f}	6.7 [0.4-18.3]^{a,d,e,f}	5.3 [0.5-20.6]^{a,b,c,f}	6.1 [0.0-17.6]^{a,b,c}	3.8 [0.1-20.9]^{a,b,c,d}	<0.001
$D_{2\%,\,Heart}$ (Gy/Gy(RBE))	29.2 [1.3-30.5]	29.1 [1.4-30.7]	29.8 [1.1-30.8]	29.5 [1.2-30.9]	30.0 [0.5-30.3]	29.6 [0.8-30.4]	0.935
$D_{mean,LAD}$ (Gy/Gy(RBE))	15.2 [0.7-30.4]^{c,d,e,f}	13.9 [0.7-26.9]^{d,f}	13.0 [0.7-30.1]^{a,d,f}	5.6 [0.7-22.7]^{a,b,c,e}	12.9 [0.1-29.8]^{a,d}	8.1 [0.1-23.1]^{a,b,c}	<0.001
$D_{2\%,\,LAD}$ (Gy/Gy(RBE))	28.3 [1.1-30.9]	28.5 [1.2-31.0]	29.9 [1.0-31.2]	22.7 [1.1-31.2]	30.3 [0.4-30.9]	26.6 [0.6-31.2]	0.215
$D_{mean,\,lungs}$ (Gy/Gy(RBE))	8.8 [4.2-18.8]^{b,c,d,e,f}	7.2 [3.8-15.8]^{a,d,e,f}	6.7 [4.0-14.2]^{a,d,e,f}	6.2 [3.6-14.1]^{a,b,c,f}	5.2 [1.9-13.8]^{a,b,c,f}	4.5 [1.8-12.2]^{a,b,c,d,e}	<0.001
$V_{20Gy,lungs}$ (%)	21.3 [8.4-57.0]^{b,c,d,e,f}	16.8 [7.6-44.8]^{a,c,d,e,f}	10.3 [3.2-29.8]^{a,b,d,e}	8.9 [3.1-25.5]^{a,b,c,e,f}	12.7 [3.8-35.8]^{a,b,c,d,f}	10.9 [3.6-32.8]^{a,b,d,e}	<0.001
$V_{5Gy,lungs}$ (%)	37.1 [16.3-76.1]^{b,c,e,f}	31.4 [15.1-70.9]^{a,c,d,e,f}	42.5 [22.7-83.5]^{a,b,e,f}	39.8 [20.0-91.1]^{b,e,f}	26.4 [9.7-66.4]^{a,b,c,d,f}	22.4 [9.1-58.0]^{a,b,c,d,e}	<0.001
$D_{mean,breastL}$ (Gy/Gy(RBE))[1]	2.1 [0.3-10.0]^{e,f}	1.6 [0.5-5.6]^{e,f}	2.2 [0.5-7.0]^{e,f}	2.3 [0.5-5.3]^{e,f}	0.5 [0.0-2.6]^{a,b,c,d}	0.7 [0.0-2.1]^{a,b,c,d}	<0.001
$D_{mean,breastR}$ (Gy/Gy(RBE))[1]	1.9 [0.4-8.5]^{e,f}	2.3 [0.5-9.9]^{e,f}	1.4 [0.4-5.3]^{e,f}	2.1 [0.4-5.1]^{e,f}	0.3 [0.0-3.0]^{a,b,c,d}	0.5 [0.0-4.2]^{a,b,c,d}	<0.001
ID (Gy·kg/Gy(RBE)·kg)[2]	80.6 [42.2-217.3]^{c,e}	85.8 [43.5-211.4]^{d,f}	79.8 [38.3-189.8]^{a,e}	84.9 [40.3-180.4]^{b,f}	42.2 [13.6-119.5]^{a,c}	44.9 [14.2-118.2]^{b,d}	<0.001
$CI_{Paddick}$	0.40 [0.35-0.56]^{b,c,d,e,f}	0.39 [0.31-0.59]^{a,c,d,e,f}	0.88 [0.85-0.90]^{a,b,e,f}	0.88 [0.84-0.91]^{a,b,e,f}	0.84 [0.74-0.87]^{a,b,c,d,f}	0.81 [0.71-0.86]^{a,b,c,d,e}	<0.001

CTV, clinical target volume; PTV, planning target volume; HI, heterogeneity index; LAD, left anterior descending coronary artery; ID, integral dose; CIPaddick, Paddick's conformity index

Statistically significant difference ($p<0.05$) for the pairwise comparison of each treatment technique vs alternatives: a vs FB 3D-CRT, b vs DIBH 3D-CRT, c vs FB VMAT, d vs DIBH VMAT, e vs FB IMPT, f vs DIBH IMPT

1For the ten female patients

2Comparison only within the same breathing technique

7. Conclusions

The overall conclusion is that optical surface imaging systems, developed within the work of this thesis, can be used as an imaging tool for accurate and faster patient setup, intrafractional motion monitoring and reduced dose to OARs during treatment in DIBH.

The use of a DIR algorithm compared to a RR algorithm was compared using an in-house developed anthropomorphic phantom, capable of anatomical deformations and torsions (**study V**). Both algorithms showed similar positioning accuracy compared to CBCT while the phantom only underwent translations, however, when deformations were applied the DIR algorithm showed a significant improved positioning accuracy in both lat and lng directions, and in pitch ($p < 0.05$) (**study V**). Still, SI registration affected by larger deformations and should be combined with other imaging modalities to establish the correlation with an internal target volume.

The impact of the system latency has to be understood, especially for treatments with fast motion gradients such as respiratory gating. In **study I**, a QA tool was in-house developed in order to measure such times for different gating systems and independent of linac vendor. The accuracy of the time measurements of the electrical PIN diode circuit (EPDC) were cross checked with the Target-I signal at a TrueBeam, showing that the QA tool can further be used for both SI systems and for other linac vendors. An important to verify latency times, especially since camera properties such as integration time, and camera gain can be manipulated for SI systems.

Study IV and **VI**, concludes that using the optical surface scanning system significantly improves the patient setup for both breast cancer and prostate cancer treatments, compared to 3-point localization. Further, the occlusion experienced by single camera systems did not show any reduced positioning accuracy for the isocenter calculation (**study IV**) compared to 3-point localization. However, a challenge for locoregional breast cancer treatments is a frequent mismatch between the alignment of bony landmarks and the chest wall surface images. Often the discrepancy is due to a combination of anatomical changes (i.e. seroma or lymphedema), errors in patient posture or bolus position. The correlation between an internal target, i.e. the prostate,

and SI was found to be significantly improved compared to 3-point localization, however, might have a small clinical effect (**study VI**). The major benefits found using SI was that the patient setup workflow became more effective, with a time saving around 1 minute, while keeping positioning accuracy for prostate patients receiving ultra-hypofractionation FFF-VMAT treatment. The faster workflow could potentially benefit the patients, since it is previously shown that the prostate moves over time [19].

The patient motion can be controlled using respiratory gating at deep-inspiration breath hold (DIBH) (**study II** and **study III**). The technique aims to reduce dose to OAR, while keeping the target coverage, which was observed for heart, left anterior descending artery and lung (**study II**). The optical SI systems capability of a large FOV was to investigate the isocenter reproducibility while triggering the treatment beam on a small ROI at the xiphiod process (**study II**). Overall, small isocenter shifts were observed for most DIBH treatments (**study II**). However, larger shifts (up to 5.6 mm) were observed which resulted in reduced target coverage and/or increased dose to OARs. To avoid such effects, a motion management strategy with tolerances also for the isocenter position should be practised. Further, treatment in deep inspiration in combination with different treatment delivery techniques were investigated for mediastinal HL (**study III**). In conclusion, the combination of intensity modulated proton therapy and deep inspiration showed the largest dose reductions to OARs and improved target coverage. However, since there is a large spread in the tumour localization, the treatment technique chosen should be individually determined for each patient.

8. Future outlook

Surface guided radiotherapy has in recent years shown to be a powerful imaging tool, with its non-invasive and real-time capabilities for patient positioning, motion tracking and respiratory gating. For future work, new phantoms for SI should be designed in order to test the registration algorithm in a routine manner both for rigid and deformable algorithms to establish standardized QA program. This would enable clinics to compare the results of the system performance with each other. In a future outlook, there are no imaging system that is standing by itself covering both inter- and intrafraction motion. The key is to in a seamless way combine the imaging systems to complement each other in an optimal way. The large FOV provided by SI can in many cases work as a complement to other imaging modalities (CBCT/kV-kV/MV) in RT, and for future image matching processes the surface information could be included in the same software. Larger anatomical changes observed in the SIs could potentially indicate if the changes would cause non-acceptable dose deviations in the treatment plan. To further optimize the treatment delivery, the tolerances for beam interruption in the OS system could be triggered by live dose deviations. For this to be realized, correlations between detected patient motion by the OSS system during beam delivery and dose deviations have to be investigated, preferably with an imaging system that can provide information about the internal anatomy over time. It would therefore be of interest to combine four dimensional MRI imaging with SI. Also, with regards to **study III** where large internal targets are not always fully covered and the target position with every breath hold cannot be observed in 3D using the gold standard of CBCT. Hence, it would be of interest to observe the internal target and OARs motion during several DIBHs with the combination of 4D magnetic resonance imaging (MRI) and SI. Another future excellent application for SI is during FLASH radiotherapy, where the treatment might be off-isocenter and therefor the SGRTs large FOV can be used to monitor the patients during the beam delivery. The treatment is delivered with an ultra-high dose rate electron beam, resulting in that the full RT treatment is delivered in just a fraction of a second [70, 71]. Hence, a real-time patient monitoring approach is highly warranted which might require improvements in the time resolution provided by todays SGRT.

9. Acknowledgements

Det har varit oerhört utvecklande och ett privilegium att ha fått möjligheten att forska inom extern strålterapi. Det är tack vare ett strålande samarbete med mina kollegor på Strålbehandlingen i Lund, teknisk utveckling tillsammans C-rads team, styrning och inspiration från Medicinsk Strålningsfysik och support från Skandionkliniken som den här avhandlingen har kunnat skrivas. Det är många som har bidragit med sin kompetens, i stort och smått, och det är jag ytterst tacksam för.

Till min huvudhandledare Sofie Ceberg,
Du har uppmanat till att finna det som väckt min nyfikenhet. Studera det noggrant, på mitt eget vis. Med ett rikt idéliv och i forskningens framkant har du varit en stor inspirationskälla. Önskar att jag blir lika klok som dig en dag.

Till min biträdande handledare Sven ÅJ Bäck,
Med dina dubbla roller som både min chef och handledare har du alltid varit lyhörd för mina forskningsstudier. Du har givit stöd både gällande tekniska förutsättningar och att multidisciplinära team har kunnat bildas då det behövts. Det är jag tacksam för.

Till min biträdande handledare Charlotte Thornberg,
Du var med och fick mig intresserad av optisk ytskanning och gating tidigt. Tack för att du så generöst delade med dig av din kompetens. Det har blivit många trevliga pratstunder på kafferasterna under dessa år!

Till medförfattare och doktorandkollega Anneli Edvardsson,
Emellanåt korsars våra forskningsintressen, och då har vi haft ett fint samarbete där vi kompletterat varandra. För det mesta har vi riktigt kul när vi skriver tillsammans! (Okej, vissa dagar raderar vi mer än vad vi skrivit nytt). Som doktorander tillsammans fick även livet komma emellan, med sovande bebis på kontoret eller standup show i New York. Tack för den fina balansen mellan hårt arbete och roliga saker.

Till medförfattare Annika Mannerberg,
Det har varit kul att tillsammans med dig titta på nya applikationer för ytskanning, där spannet minst sagt varit brett – från prostata positionering till positionering av hundar! Jag hoppas att jag får fortsätta att hänga med på ett hörn.

Tack till alla mina medförfattare, i Sverige, Danmark och Italien, som har bidragit med sin tid och sitt kunnande för att tillsammans utforska de möjligheter och begränsningar vi har med optisk ytskanning. Jag känner mig hedrad av det stora intresset och det engagemang som alla har visat under dessa år.

Tack till C-rads team, Tim Turn, Åsa Kronander, Mattias Nilsing, Daniel Lundgren och Cristina Svensson, som har lyssnat på våra önskemål och samarbetat kring att utveckla tekniken. Jag är tacksam för den stora friheten jag har haft i mina forskningsstudier.

Till Per Munck av Rosenschöld och Silke Engelholm,
Ni alltid är positiva till forskning och utveckling, som till sist kommer våra patienter till nytta. Tack för visat stöd.

10. References

1. Olle Bergman, L.F., Gabor Hont, Elizabeth Johansson, Per Ljungman, and H.N. Eva Munck-Wikland, Jan Zedenius, *Cancer i siffror.* Socialstyrelsen, 2018(ISBN: 978-91-88161-18-5).
2. Early Breast Cancer Trialists' Collaborative, G., et al., *Effect of radiotherapy after breast-conserving surgery on 10-year recurrence and 15-year breast cancer death: meta-analysis of individual patient data for 10,801 women in 17 randomised trials.* Lancet, 2011. **378**(9804): p. 1707-16.
3. Ebctcg, et al., *Effect of radiotherapy after mastectomy and axillary surgery on 10-year recurrence and 20-year breast cancer mortality: meta-analysis of individual patient data for 8135 women in 22 randomised trials.* Lancet, 2014. **383**(9935): p. 2127-35.
4. Eich, H.T., et al., *Intensified chemotherapy and dose-reduced involved-field radiotherapy in patients with early unfavorable Hodgkin's lymphoma: final analysis of the German Hodgkin Study Group HD11 trial.* J Clin Oncol, 2010. **28**(27): p. 4199-206.
5. Engert, A., et al., *Reduced treatment intensity in patients with early-stage Hodgkin's lymphoma.* N Engl J Med, 2010. **363**(7): p. 640-52.
6. Darby, S.C., et al., *Long-term mortality from heart disease and lung cancer after radiotherapy for early breast cancer: prospective cohort study of about 300,000 women in US SEER cancer registries.* Lancet Oncol, 2005. **6**(8): p. 557-65.
7. Clarke, M., et al., *Effects of radiotherapy and of differences in the extent of surgery for early breast cancer on local recurrence and 15-year survival: an overview of the randomised trials.* Lancet, 2005. **366**(9503): p. 2087-106.
8. Darby, S.C., et al., *Risk of ischemic heart disease in women after radiotherapy for breast cancer.* N Engl J Med, 2013. **368**(11): p. 987-98.
9. Giordano, S.H., et al., *Risk of cardiac death after adjuvant radiotherapy for breast cancer.* J Natl Cancer Inst, 2005. **97**(6): p. 419-24.
10. Boero, I.J., et al., *Modern Radiation Therapy and Cardiac Outcomes in Breast Cancer.* Int J Radiat Oncol Biol Phys, 2016. **94**(4): p. 700-8.
11. van den Bogaard, V.A., et al., *Validation and Modification of a Prediction Model for Acute Cardiac Events in Patients With Breast Cancer Treated With Radiotherapy Based on Three-Dimensional Dose Distributions to Cardiac Substructures.* J Clin Oncol, 2017. **35**(11): p. 1171-1178.

12. Boekel, N.B., et al., *Cardiovascular Disease Risk in a Large, Population-Based Cohort of Breast Cancer Survivors.* Int J Radiat Oncol Biol Phys, 2016. **94**(5): p. 1061-72.
13. Aleman, B.M., et al., *Long-term cause-specific mortality of patients treated for Hodgkin's disease.* J Clin Oncol, 2003. **21**(18): p. 3431-9.
14. Castellino, S.M., et al., *Morbidity and mortality in long-term survivors of Hodgkin lymphoma: a report from the Childhood Cancer Survivor Study.* Blood, 2011. **117**(6): p. 1806-16.
15. Ng, A.K., et al., *Long-term survival and competing causes of death in patients with early-stage Hodgkin's disease treated at age 50 or younger.* J Clin Oncol, 2002. **20**(8): p. 2101-8.
16. Edvardsson, A., et al., *Motion induced interplay effects for VMAT radiotherapy.* Phys Med Biol, 2018. **63**(8): p. 085012.
17. Widmark, A., et al., *Ultra-hypofractionated versus conventionally fractionated radiotherapy for prostate cancer: 5-year outcomes of the HYPO-RT-PC randomised, non-inferiority, phase 3 trial.* Lancet, 2019. **394**(10196): p. 385-395.
18. Langen, K.M., et al., *Observations on real-time prostate gland motion using electromagnetic tracking.* Int J Radiat Oncol Biol Phys, 2008. **71**(4): p. 1084-90.
19. Ballhausen, H., et al., *Intra-fraction motion of the prostate is a random walk.* Phys Med Biol, 2015. **60**(2): p. 549-63.
20. Tong, X., et al., *Intrafractional prostate motion during external beam radiotherapy monitored by a real-time target localization system.* J Appl Clin Med Phys, 2015. **16**(2): p. 5013.
21. Benedek, H., et al., *The effect of prostate motion during hypofractionated radiotherapy can be reduced by using flattening filter free beams.* Phys Imaging Radiat Oncol, 2018. **6**: p. 66-70.
22. Willoughby, T., et al., *Quality assurance for nonradiographic radiotherapy localization and positioning systems: report of Task Group 147.* Med Phys, 2012. **39**(4): p. 1728-47.
23. Greco, C. and C. Clifton Ling, *Broadening the scope of image-guided radiotherapy (IGRT).* Acta Oncol, 2008. **47**(7): p. 1193-200.
24. Ding, G.X., et al., *Image guidance doses delivered during radiotherapy: Quantification, management, and reduction: Report of the AAPM Therapy Physics Committee Task Group 180.* Med Phys, 2018. **45**(5): p. e84-e99.
25. de Boer, H.C. and B.J. Heijmen, *A protocol for the reduction of systematic patient setup errors with minimal portal imaging workload.* Int J Radiat Oncol Biol Phys, 2001. **50**(5): p. 1350-65.
26. Freislederer, P., et al., *Recent advanced in Surface Guided Radiation Therapy.* Radiat Oncol, 2020. **15**(1): p. 187.
27. Carl, G., et al., *Optical Surface Scanning for Patient Positioning in Radiation Therapy: A Prospective Analysis of 1902 Fractions.* Technol Cancer Res Treat, 2018. **17**: p. 1533033818806002.

28. Padilla, L., et al., *Assessment of interfractional variation of the breast surface following conventional patient positioning for whole-breast radiotherapy.* J Appl Clin Med Phys, 2014. **15**(5): p. 4921.
29. Shah, A.P., et al., *Clinical evaluation of interfractional variations for whole breast radiotherapy using 3-dimensional surface imaging.* Pract Radiat Oncol, 2013. **3**(1): p. 16-25.
30. Stanley, D.N., et al., *Comparison of initial patient setup accuracy between surface imaging and three point localization: A retrospective analysis.* J Appl Clin Med Phys, 2017. **18**(6): p. 58-61.
31. Hattel, S.H., et al., *Evaluation of setup and intrafraction motion for surface guided whole-breast cancer radiotherapy.* J Appl Clin Med Phys, 2019. **20**(6): p. 39-44.
32. Laaksomaa, M., et al., *AlignRT((R)) and Catalyst in whole-breast radiotherapy with DIBH: Is IGRT still needed?* J Appl Clin Med Phys, 2019. **20**(3): p. 97-104.
33. Zhao, H., et al., *Comparison of surface guidance and target matching for image-guided accelerated partial breast irradiation (APBI).* Med Phys, 2019. **46**(11): p. 4717-4724.
34. Chang, A.J., et al., *Video surface image guidance for external beam partial breast irradiation.* Pract Radiat Oncol, 2012. **2**(2): p. 97-105.
35. Bert, C., et al., *Clinical experience with a 3D surface patient setup system for alignment of partial-breast irradiation patients.* Int J Radiat Oncol Biol Phys, 2006. **64**(4): p. 1265-74.
36. Batin, E., et al., *Can surface imaging improve the patient setup for proton postmastectomy chest wall irradiation?* Pract Radiat Oncol, 2016. **6**(6): p. e235-e241.
37. Jimenez, R.B., et al., *Tattoo free setup for partial breast irradiation: A feasibility study.* J Appl Clin Med Phys, 2019. **20**(4): p. 45-50.
38. Mannerberg, A., et al., *Increased accuracy in reduced time - surface guided RT for hypofractionated prostate cancer patients.* ESTRO Abstract Book, 2020(https://cld.bz/8huStZo/214/): p. 204-205.
39. Haraldsson, A., et al., *Surface-guided tomotherapy improves positioning and reduces treatment time: A retrospective analysis of 16 835 treatment fractions.* J Appl Clin Med Phys, 2020.
40. Walter, F., et al., *Evaluation of daily patient positioning for radiotherapy with a commercial 3D surface-imaging system (Catalyst).* Radiat Oncol, 2016. **11**(1): p. 154.
41. Crop, F., et al., *Surface imaging, laser positioning or volumetric imaging for breast cancer with nodal involvement treated by helical TomoTherapy.* J Appl Clin Med Phys, 2016. **17**(5): p. 200-211.
42. PJ, B. and M. ND, *A method for registration of 3-D shapes.* IEEE Trans Pattern Anal Mach Intell, 1992(14): p. 239-256.
43. Li, H., R.W. Sumner, and M. Pauly, *Global correspondence optimization for non-rigid registration of depth scans.* Computer Graphics Forum, 2008. **27**(5): p. 1421-1430.

44. Nutti, B., et al., *Depth Sensor-Based Realtime Tumor Tracking for Accurate Radiation Therapy.* Eurographics, 2014: p. 10–13.

45. Meyer, J., et al., *Characterizing a deformable registration algorithm for surface-guided breast radiotherapy.* Medical Physics, 2020. **47**(2): p. 352-362.

46. Korreman, S.S., et al., *Breathing adapted radiotherapy for breast cancer: comparison of free breathing gating with the breath-hold technique.* Radiother Oncol, 2005. **76**(3): p. 311-8.

47. Borst, G.R., et al., *Clinical results of image-guided deep inspiration breath hold breast irradiation.* Int J Radiat Oncol Biol Phys, 2010. **78**(5): p. 1345-51.

48. Vikstrom, J., et al., *Cardiac and pulmonary dose reduction for tangentially irradiated breast cancer, utilizing deep inspiration breath-hold with audio-visual guidance, without compromising target coverage.* Acta Oncol, 2011. **50**(1): p. 42-50.

49. Rechner, L.A., et al., *Life years lost attributable to late effects after radiotherapy for early stage Hodgkin lymphoma: The impact of proton therapy and/or deep inspiration breath hold.* Radiother Oncol, 2017. **125**(1): p. 41-47.

50. Edvardsson, A., et al., *Comparative treatment planning study for mediastinal Hodgkin's lymphoma: impact on normal tissue dose using deep inspiration breath hold proton and photon therapy.* Acta Oncologica, 2019. **58**(1): p. 95-104.

51. Brahme, A., P. Nyman, and B. Skatt, *4D laser camera for accurate patient positioning, collision avoidance, image fusion and adaptive approaches during diagnostic and therapeutic procedures.* Med Phys, 2008. **35**(5): p. 1670-81.

52. Blais, F., *Review of 20 years of range sensor development.* Electronic Imaging, 2004. **13**(1): p. 231-240.

53. Placht, S., et al., *Fast time-of-flight camera based surface registration for radiotherapy patient positioning.* Med Phys, 2012. **39**(1): p. 4-17.

54. Pycinski, B., et al., *Time-Of-Flight Camera, Optical Tracker and Computed Tomography in Pairwise Data Registration.* PLoS One, 2016. **11**(7): p. e0159493.

55. N. Smith, I.M., G. Hale, R. Howe, L. Johnson, P. Edwards, D. Hawkes, M. Bidmead, D. Landau, *Real-Time 3D Surface Imaging for Patient Positioning in Radiotherapy.* Int Jornal of Radiation Oncology, Biology, Physics, 2003. **57**(2): p. 187.

56. Lindl, B.L., et al., *TOPOS: a new topometric patient positioning and tracking system for radiation therapy based on structured white light.* Med Phys, 2013. **40**(4): p. 042701.

57. Hao Li, et al., *Robust single-view geometry and motion.* ACM Trans. Graph., 2009. **28(5)**(1).

58. Sumner, R.W., Johannes Schmid, and M. Pauly, *Embedded deformation for shape manipulation.* ACM Trans. Graph., 2007. **26(3):80**.

59. Bergh, L., *Breathing adapted radiotherapy of breast cancer: Investigation of two different gating techniques and visual guidance, using optical surface scanning and pressure monitoring*, in *Department of Medical Radiation Physics, Clinical Sciences*. 2014, Lund University: lu.se. p. 50.

60. Klein, E.E., et al., *Task Group 142 report: quality assurance of medical accelerators.* Med Phys, 2009. **36**(9): p. 4197-212.
61. Stieler, F., et al., *A novel surface imaging system for patient positioning and surveillance during radiotherapy. A phantom study and clinical evaluation.* Strahlenther Onkol, 2013. **189**(11): p. 938-44.
62. Group, S.B.C., www.swebcg.se.
63. Widmark, A., et al., *Ultra-hypofractionated versus conventionally fractionated radiotherapy for prostate cancer: 5-year outcomes of the HYPO-RT-PC randomised, non-inferiority, phase 3 trial.* The Lancet, 2019. **394**(10196): p. 385-395.
64. Johnson, L.S., et al., *Initial clinical experience with a video-based patient positioning system.* Int J Radiat Oncol Biol Phys, 1999. **45**(1): p. 205-13.
65. Keall, P.J., et al., *The management of respiratory motion in radiation oncology report of AAPM Task Group 76.* Med Phys, 2006. **33**(10): p. 3874-900.
66. Edvardsson, A., et al., *Comparison of doses and NTCP to risk organs with enhanced inspiration gating and free breathing for left-sided breast cancer radiotherapy using the AAA algorithm.* Radiat Oncol, 2015. **10**: p. 84.
67. Specht, L., et al., *Modern radiation therapy for Hodgkin lymphoma: field and dose guidelines from the international lymphoma radiation oncology group (ILROG).* Int J Radiat Oncol Biol Phys, 2014. **89**(4): p. 854-62.
68. Flejmer, A.M., et al., *Respiratory gating for proton beam scanning versus photon 3D-CRT for breast cancer radiotherapy.* Acta Oncol, 2016. **55**(5): p. 577-83.
69. Paddick, I., *A simple scoring ratio to index the conformity of radiosurgical treatment plans. Technical note.* J Neurosurg, 2000. **93 Suppl 3**: p. 219-22.
70. Lempart, M., et al., *Modifying a clinical linear accelerator for delivery of ultra-high dose rate irradiation.* Radiother Oncol, 2019.
71. Konradsson, E., et al., *Establishment and Initial Experience of Clinical FLASH Radiotherapy in Canine Cancer Patients.* Front Oncol, 2021. **11**: p. 658004.

Paper I

Disponible en ligne sur
ScienceDirect
www.sciencedirect.com

Elsevier Masson France
EM|consulte
www.em-consulte.com

IRBM 37 (2016) 144–151

IRBM

Original Article

Latency Characterization of Gated Radiotherapy Treatment Beams Using a PIN Diode Circuit

M. Lempart [a,*], M. Kügele [a,b], L. Ambolt [a], B. Blad [a], F. Nordström [a,b]

[a] *Department of Oncology and Radiation Physics, Skåne University Hospital, Lund, Sweden*
[b] *Department of Medical Radiation Physics, Lund University, Lund, Sweden*

Received 23 October 2015; received in revised form 24 January 2016; accepted 8 February 2016

Available online 23 February 2016

Graphical abstract

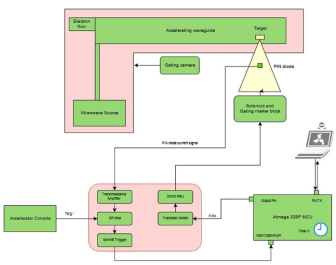

Abstract

Background: Radiotherapy is based on the premise of accurate dose delivery to target volumes within a patient, while minimizing dose to surrounding tissues. Recent developments in the treatment of breast cancer have focused on "gating" the delivery of the treatment beams to minimize the effect of patient motion during treatment, and increasing separation between the target volume and organs at risk (OAR), such as lung, heart and left anterior descending coronary artery. The basic principle involves rapidly switching the treatment beam on or off depending on the patient breathing cycle. It is therefore important to know the characteristics of gated treatments such as latency.

Methods: In this work an electrical PIN diode circuit (EPDC) was designed for quality assurance (QA) purposes to examine beam latency timing properties. Evaluation of the EPDC was performed on a TrueBeam™ (Varian, Palo Alto) linear accelerator and its internal gating system. The EPDC was coupled to a moving stage to simulate a binary pattern with fast beam triggering within predefined limits, the so called "gating window". Pulses of radiation were measured with the PIN diode and the results were compared to measurements of current produced across the linac target. Processing of the beam pulses and calculation of the latency timings was performed by an Atmega328P microcontroller.

Results: For beam-on latencies, 2.11 ms (6 MV) and 2.12 ms (10 MV) were measured using the PIN diode, compared to 2.13 ms (6 MV) and 2.15 ms (10 MV) using the target current signal. For beam-off latencies, 57.69 ms (6 MV) and 57.73 ms (10 MV) were measured using the PIN diode, compared to 57.33 ms (6 MV) and 56.01 ms (10 MV) using the target current.

Conclusions: PIN diodes can be used for accurate determination of the beam-on and beam-off latency characteristics, which could potentially lead to improvements in gated radiotherapy treatments, for example optimizing the gating windows and in estimating dosimetric errors associated with treatment beam latencies.

* Corresponding author at: Klinikgatan 5, 22242 Lund, Sweden.
E-mail address: michael.lempart@skane.se (M. Lempart).

http://dx.doi.org/10.1016/j.irbm.2016.02.002
1959-0318/© 2016 AGBM. Published by Elsevier Masson SAS. All rights reserved.

© 2016 AGBM. Published by Elsevier Masson SAS. All rights reserved.

Keywords: Linear accelerator; Respiratory gating; Radiation detectors; Radiotherapy; Clinical engineering

1. Introduction

The main premise of radiation therapy is to maximize the dose delivered to the target volume while minimizing the dose given to the surrounding healthy tissue. Developments of new treatment techniques in conjunction with advances in equipment technology seek to improve this ratio even further. Respiratory motion represents one of the major challenges in radiation therapy, especially in abdominal or lung treatments [1]. Additionally, separation between target volume and OAR can be strongly affected by breathing motion.

Optical systems for monitoring respiratory motion and controlling beam-on and beam-off are common and are based on either tracking markers attached to the patient, or scanning the patient surface directly in order to compensate for respiratory motion and organ shifting by interrupting the treatment beam when the patient surface (and by extension, the target volume) is outside predefined limits. Some gating devices, like the Real-time Position Management™ (RPM™) system (Varian, Palo Alto), are already integrated into the linear accelerator, while others are external. External devices like the Sentinel™ (C-Rad, Sweden) and Catalyst™ (C-Rad, Sweden) systems require an interface to connect to the Linac. Quality control (QC) methods like measurement of beam energy, output and geometry is needed to ensure optimal functionality of the accelerator. In addition to this, gating functionality requires monitoring of other factors relating to temporal accuracy of phase/amplitude, gating windows used, calibration of the phantom used for respiratory phase/amplitude and also tests of the interlock system [2]. Of particular importance regarding gated treatments is the beam-on and beam-off latency characteristic of the radiation beam. Beam-off latency is the most critical of these parameters to ensure that dose is not delivered when the target volume is assumed to be outside of the planned treatment position. The latency depends on the type of linear accelerator and the type of gating system used. Any delays can have undesired effects on the planned dose distribution of the treatment. Latency is also an important factor to consider in 'tracking' treatment modes e.g. Cyberknife™ (Accuray, Madison) [3].

Radiation produced by the linear accelerator consists of beam pulses, generated in the beam-on state. To produce radiation, electrons have to be accelerated inside the linacs waveguide. The so called electron gun serves as an electron source and consists of a filament, a cathode and a grid. By applying a voltage to the filament, the cathode is indirectly heated, resulting in thermionic emission of electrons. Electrons are boiled off the cathode into the space charge region, located between the cathode and the grid. Electrons remain in the space charge region as long as the grid bias voltage is more negative than the cathode. A positive voltage pulse with a width of about 4–5 μs applied to the grid, makes it more positive with respect to the cathode and electrons pass into the accelerating waveguide, which is filled with radiofrequency (RF) produced by the klystron. The electrons are accelerated close to the speed of light ($0.99c$) while propagating through the waveguide. At the end of the waveguide their path is changed with the help of a bending magnet and the electrons hit a target disk of high density, high Z material (typically tungsten). When electrons hit this target, high-energy Bremsstrahlung photons are produced. Without a high-voltage pulse applied to the grid, no electrons are injected into the accelerating waveguide and therefore no radiation is produced. For gated treatment beams, radiation should only be produced within certain predefined limits, also known as the "gating window" which is specific to each patient. In most of the common gating techniques like amplitude gating, phase gating or breath-hold gating, radiation is produced when the patients breathing pattern passes the lower limit of this gating window during inhalation, and should interrupt when the breathing pattern falls below the lower limit of the gating window during exhalation. In the beam hold state of the accelerator, the gun pulses are offset relative to the RF power pulse from the radiofrequency source of the linac so that no radiation is produced. In this way the linac remains in a stable state whereby the beam can be quickly switched back on.

Different approaches to measure the beam-on and beam-off latencies have been made.

Freislederer et al. used radiographic film and a moving phantom to simulate a patient's breathing pattern and measure the associated dose distribution [1]. The same method was used in the approach of Smith and Becker [4]. Chugh et al. also used a film based method and compared different gating techniques and motion shapes [5].

According to the American Association of Physicists in Medicine (AAPM) task groups 142 report, beam latencies should be within a recommended tolerance of 100 ms (corresponding to an error of ∼1 dose monitor unit (MU) for typical clinical linacs operating at standard dose rates). To our knowledge, no commercial tools are available at this time to measure the beam latency characteristics of medical linear accelerators with high accuracy [2,4,6].

The aim of this work was to design an electrical PIN diode circuit (EPDC) which is able to measure beam-on and beam-off latencies of gated radiation beams and which can be used with different combinations of accelerators and gating systems. This would provide a usable QA tool for radiotherapy clinics that want to examine latencies with a direct measurement method. To verify the functionality of the circuit, beam-on and beam-off timings were calculated by using two independent signals for comparison purposes.

2. Material and methods

In this work, the linacs internal gating system consisting of a gating marker block (Varian, Paolo Alto) and an infrared Polaris

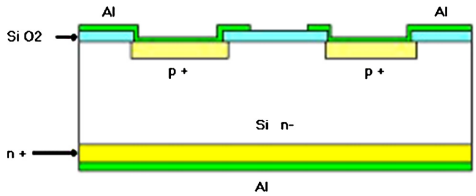

Fig. 1. PIN diode layers.

Spectra™ camera system (NDI Medical, Canada) was used to measure beam-on and beam-off latencies [7].

To be able to measure the beam-on and beam-off latencies of the gating system, the EPDC consisting of a PIN diode, an electrical circuit and a microcontroller unit (MCU), was connected to a moving phantom to simulate a binary breathing pattern and to measure the pulsed beams of radiation produced by the linac.

Beam pulses were measured by using the accelerators internal signal representing the current produced across the target (Targ I) and by using a PIN diode placed in the radiation beam as an independent measurement device. The target current serves as an indication that the radiation beam is 'on'. The target current has a value of zero if the linac is in the beam-off state. In the beam-on state a negative voltage pulse can be observed for each beam pulse. The signal can be obtained via a Bayonet Neill–Concelman (BNC) contact at the accelerator console. It should be noted that the target current signal is not available or easy to access on every type of accelerator but is present on the TrueBeam™ machines used in this study. As a suitable independent component for radiation detection, a PIN (P-type, Intrinsic type, N-type) diode (see Fig. 1) was used. These types of diodes have good sensitivity, good position resolution and are affordable [8].

A PIN diode consists of a p-type semiconductor region, an n-type semiconductor region and a wider, undoped intrinsic *i*-region inbetween. The *i*-region provides high resistance and reduces the leakage current, which would occur with the use of a normal diode. PIN diodes can be used as detectors for X-Ray and gamma ray photons [9,10]. When the diode is exposed to radiation, electron–hole pairs are generated across the *i*-layer. In reverse biased mode, generated electrons are moved to the P+ layer while the generated holes are moved to the N+ layer.

This movement of the electron–hole pairs out of the *i*-layer is measured as photocurrent [10,11]. To measure the pulsed radiation produced by a linear accelerator a sufficiently fast responding PIN diode is necessary, which is able to detect every single beam pulse. The output signals of a PIN diode can be measured as a current or as a voltage, though current measurements have a better linearity, bandwidth performance and offset [9–11]. PIN diode radiation detection circuits can be driven in photoconductive mode (PC), where the diode is biased, or in photovoltaic mode (PV), where the diode is connected to ground [12]. The operating mode of the diode is chosen to suit the demands of the application. For this application the PV mode was sufficient. The output signal of the PIN diode is relatively small, and therefore needs to be amplified to be useful. To simulate a patients breathing pattern, an in-house built phantom

Fig. 2. Left: Gating marker box made by Varian Medical System™ (Palo Alto). Right: Experimental assembly consisting of a gating phantom, solenoid and a PIN diode.

was used, which consists of a 24 Vdc, spring-loaded solenoid with a metal shaft connected to a standard gating marker block made by VARIAN Medical Systems®. The gating marker block is made of ABS757 (plastic) and consists of four infrared reflectors, which are detected by a Polaris® Spectra® infrared camera system from Northern Digital Medical® (NDI) (see Fig. 2). The marker block is usually placed on the patient's thorax during gated treatments. The movement of the marker block is controlled through a MCU and recognized by the infrared camera of the gating system, which records a set of position and orientation values [7]. By energizing and de-energizing the solenoid, an up and down movement is generated, which moves the gating marker block inside and outside the gating window. A radiation beam is only produced when the marker block is inside the gating window as detected by the infrared camera. In addition, the phantom is used to 'teach' the accelerators gating software the breathing pattern for calculation of the baseline values [7]. All measurements were performed in amplitude gating mode with photon energies 6 MV and 10 MV, both with the same PRF level of 360 Hz, and a dose rate of 600 MU/min (equivalent to a reference dose in water of 6 Gy/min). For every measurement, a total of 50 data points were collected and the results compared by calculating the arithmetic mean value and the standard deviation.

2.1. Latency measurement

All beam pulses produced by the linear accelerator are measured by an electrical circuit. The time between the marker block appearing inside the gating window and the leading edge of the first beam pulse is defined as the beam-on latency:

$$\Delta t_{beam\_on} = t_{first\_pulse} - t_{start} \quad (1)$$

The time between the gating marker block moving outside of the gating window and the falling edge of the last incoming measured beam pulse, is defined as the beam-off latency:

$$\Delta t_{beam\_off} = t_{last\_pulse} - t_{stop} \quad (2)$$

All beam-on measurements were performed with the lower limit of the gating window as close as possible to the baseline

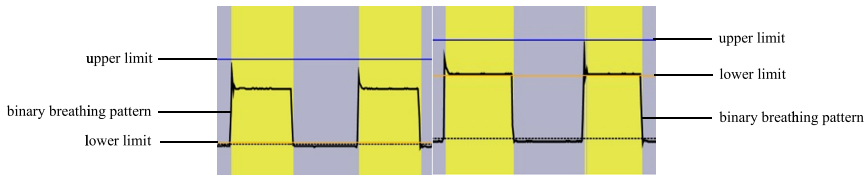

Fig. 3. Left: Setting for the lower limit of the gating window used for beam-on latency measurements. Right: Setting for the lower limit of the gating window used for beam-off latency measurements.

of the breathing pattern which keeps the marker blocks distance of travel as short as possible. For the beam-off latency measurements, the solenoid was turned by 180°, to avoid time delays caused by the magnetic field established around the coil when the solenoid is energized. In this case, the lower limit of the gating window was set as close the breathing patterns maximum as possible (see Fig. 3). Turning the solenoid by 180° during beam-off measurements ensures that requirements for beam-on and beam-off are the same, and also that the effect of inductive kickback due to the magnetic field of the solenoid is limited. When the coil is deenergized the current does not fall directly to zero. It falls exponentially and after one time constant τ the current trough the coil reaches 36.4% of the previous steady value. First after five time constant periods, the current through the coil can be considered as zero [13].

2.2. The electrical circuit

Both the target current signal and the signal from the PIN diode need to be amplified for further processing. Fig. 4 shows a block diagram of the electrical circuit used to measure the beam pulses. The output signal of the PIN diode signal is a very small electrical current fed into a two stage amplifier circuit. The chosen operational amplifiers of type NE/SE 538 are high slew rate operational amplifiers (60 V/μs) which are fast enough to measure the radiation pulses.

The first stage of the amplifier circuit consists of a transimpedance pre-amp to convert the output electrical current from the PIN diode into a voltage. Gain and bandwidth are determined by a feedback resistor R3. A feedback capacitor Cf connected in parallel to R3 avoids gain peaking and limits the frequency response. The second stage is used for further amplification. The gain of the second stage is determined by two resistors R4 and R5 (see Fig. 5). To produce a 5 V logical signal used as an input for the Atmega328P microcontroller, the amplified signal is fed into a Schmitt-Trigger, whose output is connected to the microcontroller to process the beam pulses. When the Targ I signal from the linac is used to measure the radiation beam pulses, the signal is fed into an NE538 operational amplifier. The amplifier is designed so that it is driven into saturation with every incoming beam pulse. The output of the amplifier is connected to a Schmitt trigger which connects to the MCU. In addition, the electrical circuit includes a transistor which serves as a switch to connect a 24 Vdc supply voltage to the solenoid. A diode is connected parallel to the solenoid, to avoid inductive kickback caused by the magnetic field around the coil. The solenoid is triggered by a windows based software which sends a signal in the form of a character via a virtual COM port to the MCU. If the start character is received, one of the MCUs output pins goes high and the solenoid is triggered. When the stop character is send the output pin goes low, which prevents voltage from being supplied to the solenoid. During measurement all processed beam pulse data are sent from the MCU to the software to display every single beam pulse measured.

Table 1
Timer prescalers and resolutions.

Prescaler value	Timer resolution
1	62.5 ns
8	0.5 μs
64	4 μs
256	16 μs
1024	64 μs

2.3. The Atmega328P microcontroller unit

The heart of the latency measurement system is an Atmega328P single chip Microcontroller Unit (MCU) by Atmel™ (California, USA). The Atmel 8-bit AVR RISC-based Microcontroller (Advanced Virtual reduced instruction set computing) operates between 1.8–5.5 volts and has three timers: Timer0, Timer1 and Timer2, with separate prescaler and compare mode [14]. Timer0 is an 8 bit timer, whereas Timer1 and Timer2 are 16 bit Timers.

All three Timers consists of a couple of registers which can be configured to achieve different timer functions. The clock source of the timer is tied to the frequency f_{clk} of the MCU.

Timers can be used with prescalers of 1, 8, 64, 256 or 1024 to work in different frequency ranges.

Using a prescaler affects the resolution T of the Timer (see Table 1), which is given by:

$$T = \frac{1}{fclk} * prescaler \tag{3}$$

To achieve the best possible resolution a prescaler of 1 is chosen which results in a timer resolution and overflow every 62.5 ns. Every overflow must be taken care of with help of an overflow vector implemented in the MCUs software, written in C++ and stored in the internal memory of the Atmega328P. Once the

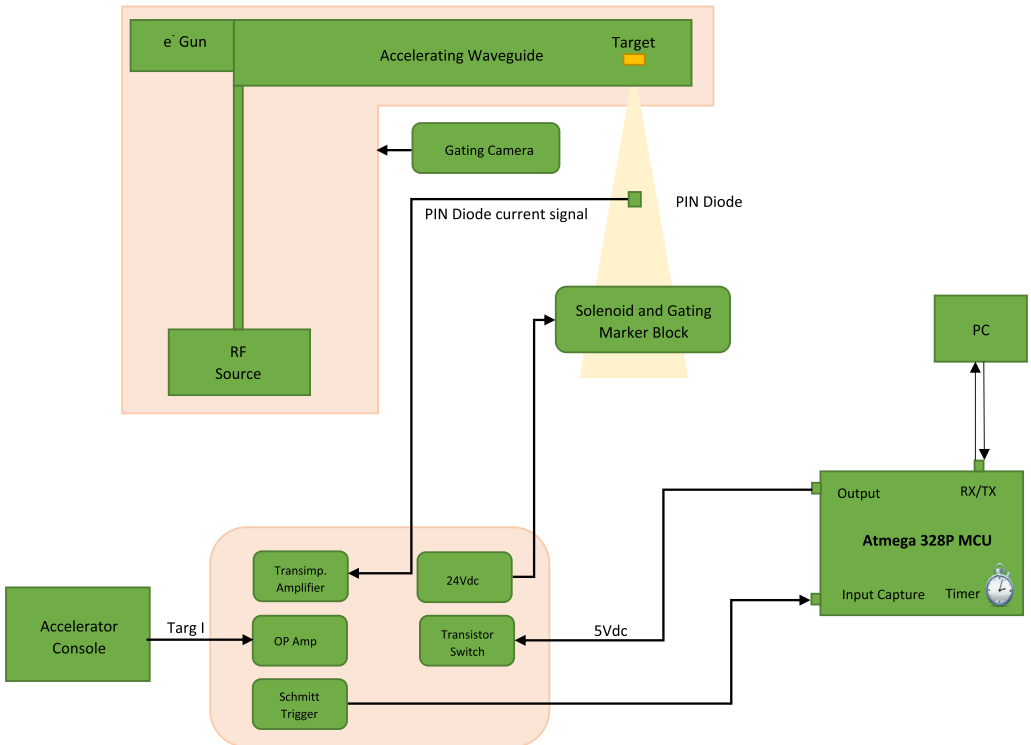

Fig. 4. Block diagram of the gating latency measurement system.

supply voltage is applied to the microcontroller the program is compiled. The processed signals from the PIN diode or the tungsten target are connected to the microcontrollers external interrupt pin INT0. An external interrupt is considered as a pin changing event, where the interrupt pin goes from high to low or from low to high. When this occurs, the main routine of the MCU is interrupted and an Interrupt Service Routine (ISR) is executed.

The ISR is used to save the time stamps of the incoming beam pulses. The timer of the MCU toggles between triggering the rising and falling edges of the radiation pulses when a measurement has been started. When the measurement has been stopped the triggering is changed to falling edges only, waiting for eventually incoming pulses during a certain amount of time.

3. Results

Table 2 shows the results of the comparison between the two different signals for two different photon energies, 6 MV and 10 MV. It can be seen that the beam-on latency time of the TrueBeam™ linear accelerator in combination with its gating system is shorter compared to the beam-off time in all cases. The results of the latency measurements were statistically tested with a students t-test. No significant difference could be seen in the comparison ($p < 0.01$).

4. Discussion

Measuring beam latencies with a PIN diode in combination with the in-house built electrical circuit seems to be a much more accurate method than using a radiation sensitive film, where beam-on latencies of 215 ± 69 ms and beam-off latencies of 851 ± 100 ms have been reported by other groups [1]. Their method led to a relatively high standard deviation, uncertainties in determination of a suitable starting point and was limited by the performance of the overall scanning procedure [1]. In addition, using a PIN diode is a direct measurement without the need to wait as it is the case with film dosimetry (exposure, scanning and processing).

When measuring beam-on and beam-off latencies, parameters like the overall system latency of the gating system and linear accelerator, the magnetic field of the solenoid and the accurate positioning of the lower limit of the gating window have to be taken into consideration. The overall latency of the gating system, which can be considered as the time the gating camera needs to send image data to the XI imaging system of the

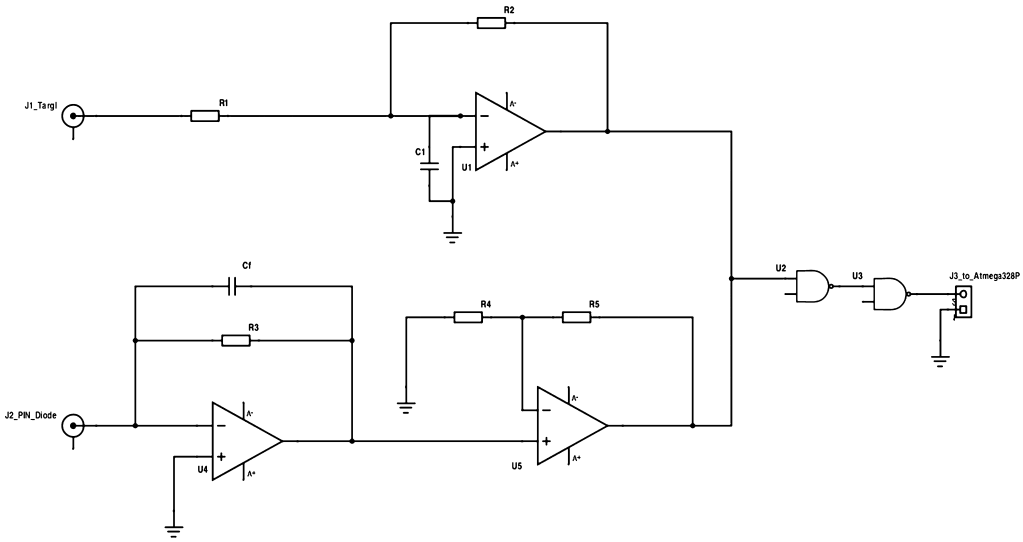

Fig. 5. Circuit diagram of the latency measurement system.

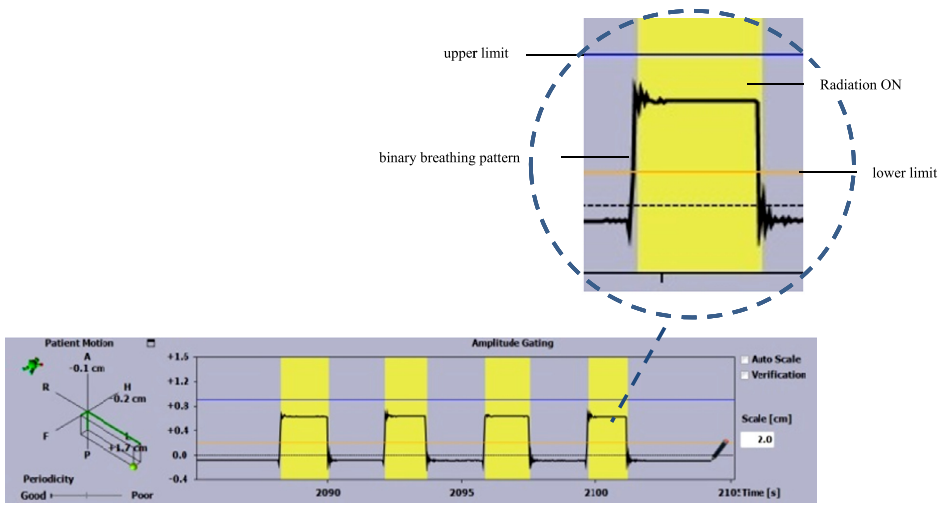

Fig. 6. Filtered breathing pattern of the TrueBeam™ software.

Table 2
Results of the latency measurements.

Energy	Beam-on latency (ms)		Beam-off latency (ms)	
	Targ I	PIN diode	Targ I	PIN diode
6 MV	2.13 ± 1.15	2.11 ± 1.05	57.33 ± 10.01	57.69 ± 9.59
10 MV	2.15 ± 1.06	2.12 ± 1.09	56.01 ± 10.10	57.73 ± 10.06

linear accelerator to process and analyze the data is considered as negligible for conventional radiotherapy, but might be taken into consideration for Flattening Filter Free (FFF) beams and multiple interruptions of the beam. By setting the lower limit of the gating window as close to the breathing patterns baseline as possible while measuring beam-on latencies and by setting the lower limit close to the patterns peak for beam-off measurements, minimal travel and minimum time delay is achieved

for the gating marker block positioned on top of the solenoids shaft.

The results show that beam-on response is about twenty times shorter than the beam-off response.

By analyzing the gating graphs, plotted by the accelerators system software, it can be seen that the actual radiation span shows a noticeable offset compared to the original breathing pattern produced by the gating phantom (see Fig. 6). This offset could result in significant delays when measuring beam-on and beam-off latencies.

An explanation for the offset of the radiation span could be that the gating software makes use of a moving average (MA) filter, which is a simple finite impulse response (FIR) or low-pass filter commonly used in digital signal processing. These types of filters are used to remove unwanted signal noise. This is done by taking a sequence of data points and replacing it by a local average [15,16]. Each point of the processed sequence is given by:

$$y[n] = \frac{1}{N}\sum_{k=0}^{N-1} x[n-k] \tag{4}$$

where $y[n]$ is the output signal, $x[n-k]$ the input signal and N the amount of data points used to calculate the moving average. The smoothing effect of the MA filter is dependent on the amount of data points N. Because every output value of the filter is an average of a certain sequence $y[n]$ with N data points, the calculated average is a value in the middle of the sequence, thus introducing a delay of $N/2$ which grows with the number of data points used [17,18]. That delay caused by the MA filter could explain the long beam-off latency. Because of the fast response when measuring beam-on, it can be assumed, that the filter is not used in the beginning of the breathing pattern to achieve a fast response. Even if the MA filter seems to affect the latency measurements, it can be assumed that there is no significant effect on treated gating beams. The breathing pattern produced by the solenoid is noisy because of its fast rise and fall time and because of the fact that the solenoid is spring-loaded, which adds oscillation to the beginning and the end of the signal. The risks of adding such an offset and with that unwanted additional beam pulses during normal gated treatments is presumably small, because the patients breathing pattern is slower and smoother than the artificial phantom motion. All of the results are within the tolerance of 100 ms recommended by the AAPM task group 142 report [2].

Because time delays and internal system latencies strongly depend on the type of linear accelerator and the type of gating system used, further measurements have to be done so that different combinations can be compared. Additionally the characteristics of different gating techniques, like phase- and amplitude-based gating have to be compared. In the work of Chugh et al it can be seen that there is a possibility that time delays in phase-based gated radiation treatment beams are substantially higher than in amplitude-based gated treatment beams [5].

Once beam latencies in gated treatments are calculated accurately, additional functions could potentially be added to the gating system for compensation purposes. This could include adjusting the upper and lower limits of the gating window to compensate for latency, leading to an even more accurate treatment.

Optimal tuning of the linear accelerator is also critically important. A slightly mistuned accelerator tends to exhibit poorer startup characteristics, affecting the beam delivery and introducing unwanted deviations in delivered dose compared to the planned treatment. To ensure long-term stability of the linear accelerator and the gating system, regular QA measurements and examination of the equipment is crucial.

The EPDC was evaluated using two independent signals to verify the accuracy of the system and the statistical tests applied to the measured data showed no significant difference ($p < 0.01$). This implies that the EPDC is a stable QA tool that can be used to evaluate beam latencies for all models of radiotherapy linear accelerators. This is useful when examining the latency characteristics of gated treatment beams, but could also have a more general function in monitoring overall linac performance by measurement of both beam-on and beam-off times.

5. Conclusions

Measuring beam-on and beam-off latencies of a linear accelerator via beam pulse analyses with the help of an in-house developed EPDC has shown good agreement with measurements from the accelerator target current signal. The PIN diode provided a good response when using different beam energies. The evaluation of the TrueBeam™ (Varian, Palo Alto) accelerator and its gating system shows a fast response for both beam-on and beam-off timing.

The EPDC is the first independent QA tool developed that is able to measure beam latencies accurately. The system can be connected to either the target current signal or to a PIN diode as an independent device, which allows the EPDC to be used on different gating systems and types of accelerators.

References

[1] Freislederer P, Reiner M, Hoischen W, Quanz A, Heinz C, Walter F, et al. Characteristics of gated treatment using an optical surface imaging and gating system on an Elekta linac. Radiat Oncol 2015;19:10–68.
[2] Klein EE, Hanley J, Bayouth J, Yin F-F, Simon W, Dresser S, et al. Task Group 142 report: quality assurance of medical accelerators. Med Phys 2009;36(9):4197–212.
[3] Ernst F. Compensating for quasi-periodic motion in robotic radiosurgery. New York, NY: Springer; 2012.
[4] Smith WL, Becker N. Time delays and margins in gated radiotherapy. J Appl Clin Med Phys 2009;10(3):140–54.
[5] Chugh BP, Quirk S, Conroy L, Smith W. Measurement of time delays in gated radiotherapy for realistic respiratory motions. Med Phys 2014;41(9):091702.
[6] Bourland JD. Image-guided radiation therapy. Boca Raton: Taylor & Francis; 2012.
[7] Varian medical systems. TrueBeam technical reference guide, vol. 2: Imaging. 2014.
[8] Mondragón-Contreras L, Ramírez-Jiménez FJ, Aguilera-Reyes EF, Ojeda-Nava CE. In: PIN photo-diodes as radiation detectors in accelerator applications. 2012.

[9] Ahmed SN. Physics and engineering of radiation detection. Amsterdam: Academic Press; 2007.
[10] Knoll GF. Radiation detection and measurement. New York: Wiley; 2000.
[11] Ramírez-Jiménez FJ, Mondragón-Contreras L, Cruz-Estrada P. Application of PIN diodes in physics research. AIP Conf Proc, vol. 857. 2006. p. 395.
[12] Yoon J-Y. Introduction to biosensors. New York, NY: Springer; 2013.
[13] Horowitz P, Hill W. The art of electronics. Cambridge, England: Cambridge University Press; 1989.
[14] Atmel Corporation, Atmega48PA/88PA/168PA/328P datasheet. Rev. 8161D-AVR-10/09; 2009.
[15] Smith SW. Digital signal processing. Amsterdam: Newnes; 2003.
[16] Semmlow JL, Griffel B. Biosignal and medical image processing. 3rd edition. Hoboken: CRC Press; 2014.
[17] Prandoni P, Vetterli M. Signal processing for communications. Lausanne, Switzerland: EPFL Press; 2008.
[18] Whitaker JC. The electronics handbook. CRC Press; 2005.

Paper II

Received: 20 June 2017 | Revised: 26 August 2017 | Accepted: 15 September 2017

DOI: 10.1002/acm2.12214

RADIATION ONCOLOGY PHYSICS

WILEY

Dosimetric effects of intrafractional isocenter variation during deep inspiration breath-hold for breast cancer patients using surface-guided radiotherapy

Malin Kügele[1,2] | Anneli Edvardsson[2] | Lovisa Berg[1] | Sara Alkner[1] | Carina Andersson Ljus[1] | Sofie Ceberg[1,2]

[1]Department of Hematology, Oncology and Radiation Physics, Skåne University Hospital, Lund, Sweden

[2]Medical Radiation Physics, Department of clinical sciences, Lund University, Lund, Sweden

Author to whom correspondence should be addressed. Sofie Ceberg
E-mail: sofie.ceberg@med.lu.se

Abstract

The aim of this study was to investigate potential dose reductions to the heart, left anterior descending coronary artery (LAD), and ipsilateral lung for left-sided breast cancer using visually guided deep inspiration breath-hold (DIBH) with the optical surface scanning system Catalyst™, and how these potential dosimetric benefits are affected by intrafractional motion in between breath holds. For both DIBH and free breathing (FB), treatment plans were created for 20 tangential and 20 locoregional left-sided breast cancer patients. During DIBH treatment, beam-on was triggered by a region of interest on the xiphoid process using a 3 mm gating window. Using a novel nonrigid algorithm, the Catalyst™ system allows for simultaneous real-time tracking of the isocenter position, which was used to calculate the intrafractional DIBH isocenter reproducibility. The 50% and 90% cumulative probabilities and maximum values of the intrafractional DIBH isocenter reproducibility were calculated and to obtain the dosimetric effect isocenter shifts corresponding to these values were performed in the treatment planning system. For both tangential and locoregional treatment, the dose to the heart, LAD and ipsilateral lung was significantly reduced for DIBH compared to FB. The intrafractional DIBH isocenter reproducibility was very good for the majority of the treatment sessions, with median values of approximately 1 mm in all three translational directions. However, for a few treatment sessions, intrafractional DIBH isocenter reproducibility of up to 5 mm was observed, which resulted in large dosimetric effects on the target volume and organs at risk. Hence, it is of importance to set tolerance levels on the intrafractional isocenter motion and not only perform DIBH based on the xiphoid process.

PACS
87.55.D

KEY WORDS
breath hold, intrafractional isocenter variation, optical surface scanning, treatment planning

This is an open access article under the terms of the Creative Commons Attribution License, which permits use, distribution and reproduction in any medium, provided the original work is properly cited.
© 2017 The Authors. *Journal of Applied Clinical Medical Physics* published by Wiley Periodicals, Inc. on behalf of American Association of Physicists in Medicine.

1 | INTRODUCTION

Adjuvant radiotherapy for breast cancer reduces the risk of locoregional recurrence as well as breast cancer death.[1,2] However, some radiation is inevitably delivered to normal tissue, such as the heart and lungs, which has been shown to increase the risk of cardiovascular and pulmonary disease.[3–9] Darby et al.[5] have shown that the relative risk of ischemic heart disease increases with 7.4% per Gy increased mean heart dose, with no apparent threshold. This relationship was recently validated by van den Bogaard et al.[8] for more modern radiotherapy techniques. Also, a higher incidence of coronary artery disease has been observed for the left anterior descending coronary artery (LAD) for left-sided compared to right-sided breast radiotherapy.[10] This could possibly reduce the survival benefit of breast cancer radiotherapy.

Since a large proportion of the breast cancer patients are cured from their disease and hence become long-term survivors, with the 5-year survival being approximately 90%,[11] it is important to reduce the late side-effects as much as possible. Therefore, there has been much focus in the last years in breast cancer radiotherapy to develop treatment techniques that reduce the dose to normal tissues, such as treatment during deep inspiration, prone patient positioning, intensity modulated radiotherapy, proton radiotherapy, and partial breast radiotherapy.[12] Treatment during deep inspiration has been shown to decrease the cardiopulmonary doses without compromising target coverage, due to increased spatial distance between the organs at risk and the target as well as decreased lung density.[13–16] Treatment in deep inspiration breath-hold (DIBH) requires patient compliance and the use of visual guidance has been shown to improve intrafractional reproducibility of the inspiration level.[17,18] Several techniques for tracking the breathing motion have been introduced in radiotherapy, such as measuring the motion extent of external markers or the pressure in a belt or the variation in air flow. The latest techniques involve optical surface (OS) scanning systems such as the Sentinel™ and Catalyst™ (C-rad Positioning AB, Uppsala, Sweden) or AlignRT (VisionRT, London, UK). The systems project light onto the patients' skin surface and reconstruct a three-dimensional surface of the patient. The OS system detects the patients' position and movements and is used to trigger the beam for treatment delivery in DIBH.[19] Several studies have evaluated patient setup accuracy during DIBH for left-sided breast cancer for 3D surface matching,[20–22] but few have investigated any dosimetric effects due to potential positioning deviations. For instance, Tang et al.[23] evaluated the dosimetric impact of motion during DIBH for an iterative closest point (ICP)-based algorithm for surface matching with the AlignRT system, using a $\pm$ 3 mm and $\pm 3^{\circ}$ tolerance for translational and rotational differences. They reported very small (<1 mm) breath-hold motion and the dosimetric consequences were found to be small. However, only the rigid motion of the surface was investigated.

By using a novel nonrigid registration algorithm as well as finite element simulation of underlying tissues, the real-time isocenter position can be determined from the surface motion. Thus, the optical surface scanning system (Catalyst™) can not only track the surface but also the real-time isocenter position.[24,25] Several studies have shown dosimetric benefits of the DIBH treatment technique for breast cancer patients[13–15] and several studies have shown increased accuracy in patient positioning using optical surface scanning.[20–22] However, to the best of our knowledge, no investigation of potential dosimetric effects due to intrafractional isocenter motion during DIBH has been carried out and are thus highly desirable.

In this study, audio and visual guidance were used for the patients to achieve reproducible DIBHs. The surface over the xiphoid process worked as the surrogate for the target position for beam triggering during both CT imaging and treatment. During DIBH at the treatment machine, the Catalyst™ system was used for triggering the beam when the xiphoid process entered the gating window and simultaneously tracked the isocenter position. The intrafractional DIBH isocenter reproducibility in between breath holds was investigated and the subsequent dosimetric effects evaluated for both tangential and locoregional treatment of left-sided breast cancer.

The aim of this study was to investigate potential dose reductions to organs at risk (OARs) using DIBH and optical surface scanning, and further evaluate how any dosimetric benefits are affected by possible intrafractional isocenter motion in between breath holds.

2 | MATERIAL AND METHOD

2.A | Ethical consideration and consent

The use of the radiotherapy database for retrospective research has been approved by the Regional Ethical Review Board in Lund (No. 2013/742).

2.B | Patient selection

A total of 40 patients receiving radiotherapy for left-sided breast cancer in DIBH were enrolled in this study, 20 patients received tangential treatment after breast-conserving surgery and 20 patients received locoregional treatment after either breast-conserving surgery or mastectomy. The patients started treatment between September 2015 and August 2016. The median age was 59 yr (range: 45–77 yr) for the group receiving tangential treatment and 46 yr (35–85 yr) for the group receiving locoregional treatment.

2.C | Computed tomography simulations and treatment planning

All patients underwent supine computed tomography (CT) in separate scans for free breathing (FB) and DIBH. Images with a slice thickness of 3 mm were acquired using a Siemens Somatom definition AS plus (Siemens Medical Solutions, Erlangen, Germany). The prospective DIBH study was performed with the Sentinel™ system (C-rad Positioning AB, Uppsala, Sweden) using laser (λ = 635–690 nm) to create

a reference surface of the patient in FB and record the breathing motion.[26] The patients were scanned with the Sentinel™ system in FB and a region of interest (ROI) was defined on the surface of the skin above xiphoid process in a shape of a circle with a diameter of 2 cm. Motion in the vertical direction in the ROI was registered as the breathing signal. Since the registered motion was in the vertical direction only, the rather flat and stable surface on sternum was chosen. The position of the end-expiration for FB level, that is, the baseline, was automatically tracked and the amplitude was individually set for each patient at the maximum comfortable and reproducible breath hold level. The gating window was 3 mm for all patients included. Visual guidance with video goggles was used to help the patients keep the inspiration level in the gating window during the CT acquisition. To avoid abdominal breathing or so-called fake breathing, that is, arching the back, the patients were asked to breathe with their chest during a short training session of a few breath holds using visual feedback prior to CT imaging. For patients receiving locoregional treatment after mastectomy, a bolus (Superflab, Mick Radio-Nuclear Instruments, Inc. An Eckert & Ziegler BEBIG Company) was placed on the thoracic wall over the operation scar with a 3 cm margin at CT.

2.C.1 | Structure delineation

All structures were delineated in both the DIBH and FB CT sets by the same radiation oncologist, to reduce the interobserver variability. For tangential breast irradiation after breast-conserving surgery, the PTV was defined as the clinical limits of the remaining breast including all glandular tissue. For cases receiving locoregional treatment after breast-conserving surgery, ipsilateral axillary lymph nodes level II-III and lymph nodes in the supra- and infraclavicular fossa were included in the PTV. Thus, the internal mammary nodes were not included. The CTV-T was delineated as the tumor's position in the breast with at least 10 mm margin, approximately equivalent to a quadrant of the breast. After mastectomy, the PTV was defined as the part of the thoracic wall where the breast had been located (visualized on CT scans by markers), including ipsilateral lymph node stations as above. No CTV-T was delineated for these patients. For all patients, the PTV was cropped 5 mm from the skin surface.

The OARs delineated were the heart, LAD, and the ipsilateral lung. The lung was automatically delineated using the segmentation wizard in the treatment planning system (TPS, Eclipse, version 13.6.30, Varian Medical Systems, Palo Alto, CA, USA) and then manually verified. The heart was defined as the entire myocardium including the large vessels up to the departure of the coronary arteries from aorta ascendens. LAD was delineated with a 6 mm diameter from the vessels departure from aorta as far as it could be visualized, often to the middle of the heart. The heart and LAD were delineated manually and all OARs were delineated without margins.

2.C.2 | Treatment planning

The treatment plans were created in the Eclipse TPS for an Elekta Synergy (Elekta AB, Stockholm, Sweden) and the dose was calculated using the anisotropic analytic algorithm (AAA, version 10.0.28 and 13.6.23). The prescribed dose was 50 Gy in 25 fractions, normalized to the PTV mean dose. All treatment plans were made by one dosimetrist, for the plans to be comparable between DIBH and FB. The main goal when creating the treatment plans was to fulfill the constraints presented in Table 1, based on national guidelines for 2014–2016 from the Swedish Breast Cancer Group (www.swebcg.se). At the same time, the OAR doses were kept as low as possible.

TABLE 1 Constraints aimed to be fulfilled when creating the treatment plans.

Structure	Constraint
CTV-T	$V_{95\%} = 100\%$
CTV-T	$D_{mean} \geq 100\%$
PTV	$D_{98\%} \geq 93\%$
PTV	$V_{105\%}$ minimized

Essentially identical three-dimensional conformal radiotherapy (3D-CRT) isocentric treatment plans were created for both DIBH and FB, where only minor differences in the beam arrangement were allowed to achieve comparable target coverage. For tangential treatment, two tangential opposing fields were used to irradiate the breast. If needed for dose homogenization, wedges and/or supplementary fields were used. The energy 6 MV was used for all fields. For locoregional treatment, 6 MV tangential opposing fields were used to irradiate the breast and, if necessary, supplementary fields were added (6 MV). The lymph nodes were irradiated using a 6 MV anterior–posterior (AP) field and a 10 MV posterior–anterior (PA) field. Additionally, a 10 MV PA field shielding the lung was added. For tangential treatment, the isocenter was placed in the center of the breast, and for locoregional treatment, the isocenter was placed in the junction between the tangential and AP/PA fields.

2.D | Dosimetric comparison between DIBH and FB treatment plans

For the comparison between the DIBH and FB treatment plans, the mean dose to the heart ($D_{mean,heart}$), LAD ($D_{mean,LAD}$), and ipsilateral lung ($D_{mean,lung}$), the dose received by 2% of the volume for the heart ($D_{2\%,heart}$) and LAD ($D_{2\%,LAD}$), the volume receiving 20 Gy for the ipsilateral lung ($V_{20Gy,lung}$) and the dose received by 98% of the PTV volume ($D_{98\%,PTV}$) were retrieved from the TPS. Two-sided paired Wilcoxon tests were carried out to investigate if the differences between DIBH and FB were statistically significant, using a significance level of 0.05.

2.E | The DIBH treatment workflow using Catalyst™

When the treatment plan was finished, the plan isocenter, treatment fields, and plan UID were exported in DICOM format from the TPS to the Catalyst™ system. To assess the treatment isocenter for patient positioning in FB, the reference surface from the Sentinel™

system was connected to the isocenter of the treatment plan. The commissioning of the Catalyst™ system demonstrated an intrinsic accuracy of 0.2 mm isocenter localization at various isocenter depths confirmed by CBCT. The Catalyst™ system was used for the treatment sessions at the linear accelerator. The system uses a near invisible violet light (λ = 405 nm) projected onto the patient during surface imaging and measurement.[27] The other wavelengths available, that is, green (λ = 528) and red (λ =624) lights, were used to project a color map onto the patient's surface indicating any setup deviations. The treatment workflow was divided into two modules, one positioning module and one treatment module. All patients were initially positioned in FB using a nonrigid algorithm for patient positioning.[24,25] The live surface of the patient being scanned on the treatment couch in FB was matched with the reference surface obtained with the Sentinel™ system at the CT session. Posture correction was manually performed with the help of the color map projected onto the patient's skin indicating deviations between the planned and real-time position larger than 5 mm. The couch was shifted to the treatment position according to the calculations made by the OS system. A floating mean value filter over 4 s was used for the calculation to minimize the effect of the FB motion.

Once the patient was positioned correctly, the Catalyst™ treatment module was entered. The breathing baseline was established at the beginning of each treatment fraction, ensuring that the breathing amplitude was identical for every DIBH session, regardless of any daily residual setup deviation. Thus, the distance between the tumor volume and the heart could be maintained during irradiation, as well as the level of decreased lung density within the beam. If the setup needed to be corrected for prior to treatment, the baseline was recalculated. A daily surface reference image, $REF_{(Treat\ in\ DIBH)}$, was captured the first time when the patient was breathing into the gating window. The live surface obtained during the rest of the treatment fraction was matched with $REF_{(Treat\ in\ DIBH)}$, and hence these surfaces should coincide during DIBH [Fig. 1(a)]. This means that differences between the live surface and $REF_{(Treat\ in\ DIBH)}$ do not include the residual setup errors, which are thus not transferred from the positioning module to the treatment module.

Two of the three algorithms provided by the Catalyst™ system with calculations for beam triggering for DIBH treatments were used in this study.[24] The first algorithm was calculating the separation in z-direction between the $REF_{(Treat\ in\ DIBH)}$ and the live surfaces in an area predefined by the ROI. When the respiratory signal recorded in the ROI was within the gating window, the treatment beam was triggered [Fig. 1(b)]. Simultaneously, the Catalyst™ system's nonrigid algorithm was used to calculate any isocenter shifts by matching the $REF_{(Treat\ in\ DIBH)}$ and the live surfaces [Fig. 1(c)]. However, no tolerances for beam triggering based on the isocenter shifts were set in this study and this was used for retrospective evaluation purposes

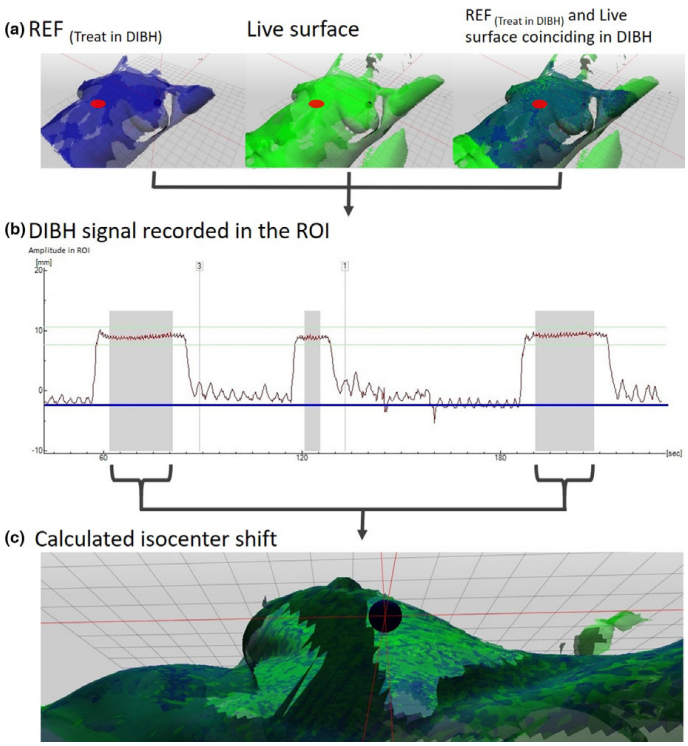

FIG. 1. Workflow in the treatment module. The ROI shown as a red circle at xiphoid process was triggering beam-on when the reference surface ($REF_{(treat\ in\ DIBH)}$) was coinciding with the live surface (a). The DIBH signal in the ROI was tracked (b) and the isocenter shifts during beam-on (gray fields in b) simultaneously recorded (c).

only. Thus, the calculations within the ROI above the xiphoid process resulted in one-dimensional breathing motion, presented to the patient by visual guidance, and triggered the beam within the narrow gating window. At the same time, the three-dimensional motion data of the isocenter were passively collected.

2.F | Assessment of the intrafractional DIBH isocenter reproducibility

In this study, the intrafractional DIBH isocenter reproducibility during beam-on was investigated. The real time calculated isocenter position during beam-on was obtained from the log files of the OS system. The intrafractional DIBH isocenter reproducibility was then calculated as the difference between the average isocenter positions during beam-on for two DIBHs during each session. The two DIBHs were selected from the delivery of the two main fields, which represents the position for which the main part of the treatment was given. The intrafractional motion, that is, the relative shift between two DIBHs, was analyzed for five treatment sessions per patient. In total, 195 DIBHs per group were included in the analysis. One patient in each patient group was excluded due to treatment interruptions on the linear accelerator, causing the log files to be incomplete. For the tangential treatments, the isocenter shift between the two main fields were used and for the locoregional treatments, isocenter shifts from one of the tangential fields and one of the AP/PA fields were used. The intrafractional DIBH isocenter reproducibility in the lateral (lat), longitudinal (long), and vertical (vert) directions were analyzed separately for the two patient groups.

2.G | Analysis of dosimetric effects induced by intrafractional DIBH isocenter reproducibility

The intrafractional DIBH isocenter reproducibility was applied to the treatment plans in the TPS as a set of isocenter shifts to generate dose distributions, resulting in an approximation of the dosimetric effects of the intrafractional isocenter DIBH motion. The intrafractional DIBH isocenter reproducibility in lat, long, and vert directions corresponding to a cumulative probability of 50% of the DIBHs, 90% of the DIBHs and the maximum (max) value, was used for the two patient groups. The cumulative probability means that for X% of the DIBHs, the intrafractional DIBH isocenter reproducibility is less or equal to Y mm. For example, the 50% cumulative probability represents the median isocenter reproducibility for the whole patient group. For each shift, the dose was recalculated in the original DIBH plan which, since all combination of directions were simulated, resulted in eight plans per shift level (50%, 90%, and max). In total, 960 isocenter-shifted plans were obtained. For each isocenter-shifted plan, the dose was recalculated keeping the same number of monitor units. From the resulting DVHs, the $D_{mean,heart}$, $D_{mean,LAD}$, $D_{mean,lung}$, $D_{2\%,heart}$, $D_{2\%,LAD}$, $V_{20Gy,lung}$, and $D_{98\%,PTV}$ were obtained and the minimum and maximum values for each patient and probability level were considered for the motion-induced dose effect evaluation.

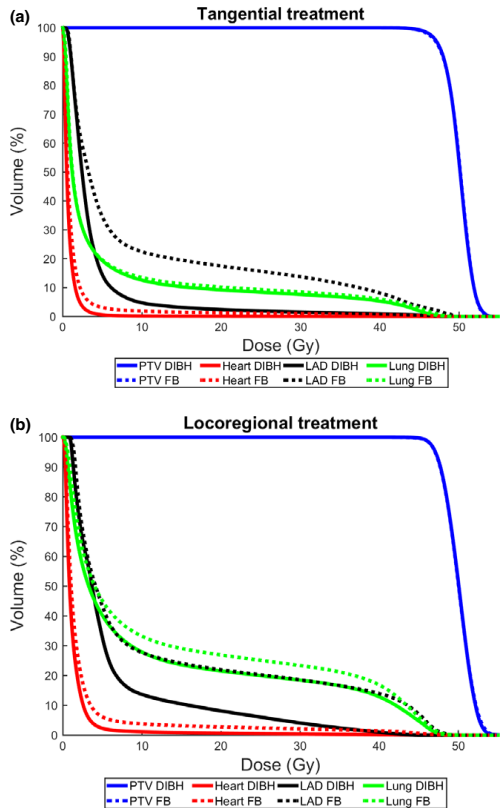

FIG. 2. Average relative dose volume histograms for tangential (a) and locoregional (b) treatment for the heart (red), LAD (black), ipsilateral lung (green), and PTV (blue) comparing DIBH (solid lines) and FB (dashed lines).

3 | RESULTS

3.A | Dosimetric comparison between DIBH and FB treatment plans

Overall, the dose to the heart, LAD, and ipsilateral lung was reduced for all dose levels with comparable target coverage for DIBH compared to FB for both tangential and locoregional treatment [Fig. (2)]. The heart and LAD mean doses and $D_{2\%}$ were reduced for essentially all patients using DIBH and the mean lung dose and V_{20Gy} were reduced for the majority of the patients [Fig. (3)]. For patients with high OAR doses in FB, larger reductions of the dosimetric parameters were generally observed with DIBH [Fig. (3)]. The median deep inspiration amplitude during CT, measured with the Sentinel™ system at the xiphoid process, was 10.5 mm (range: 5.4–19.6 mm) for tangential treatment and 10.3 mm (8.2–13.0 mm) for locoregional treatment.

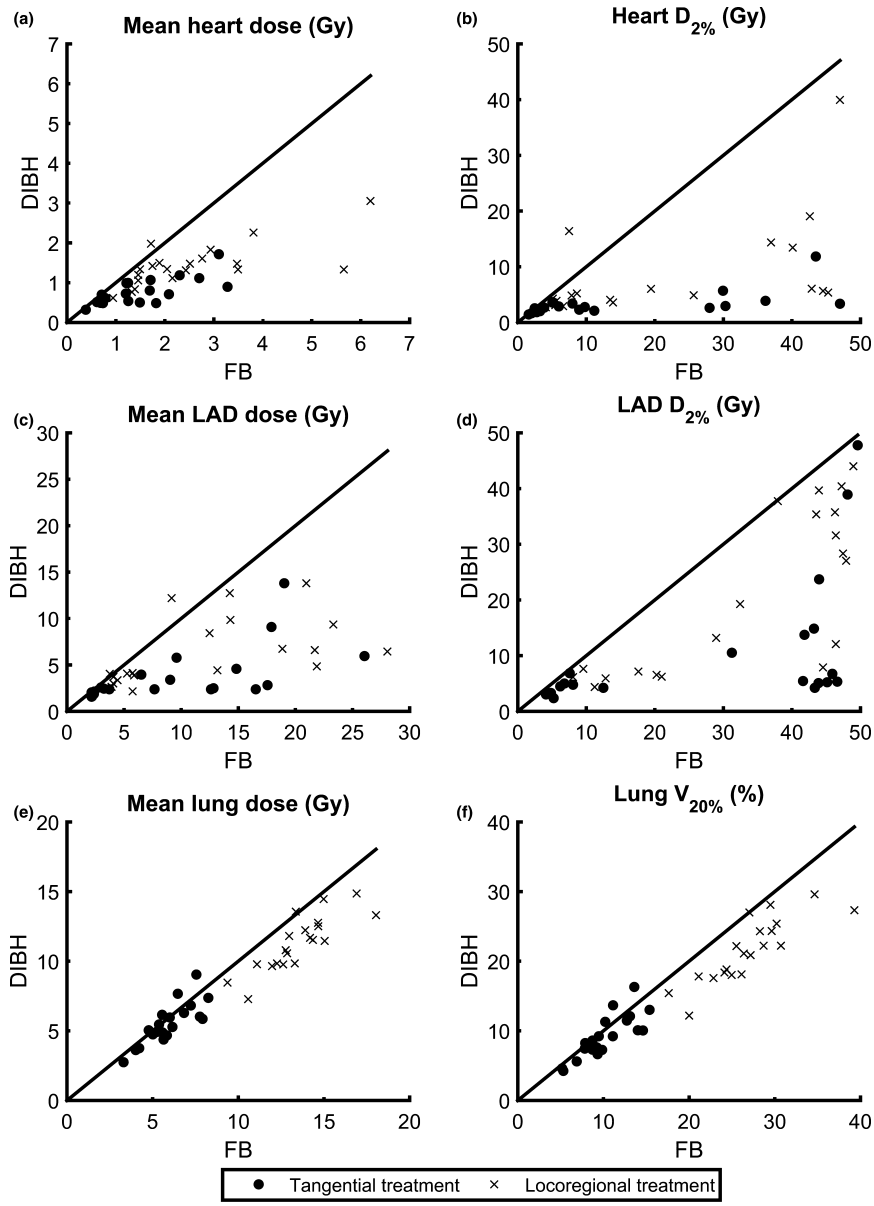

FIG. 3. Individual values for each patient of $D_{mean,heart}$ (a), $D_{2\%,heart}$ (b), $D_{mean,LAD}$ (c), $D_{2\%,LAD}$ (d), $D_{mean,lung}$ (e), and $V_{20Gy,lung}$ (f) for deep inspiration breath-hold (DIBH) versus free breathing (FB), for both tangential (circles) and locoregional (crosses) treatment. The lines are for illustration purpose only, and represent where the dosimetric parameters are equal for DIBH and FB. Hence, for points below the line, DIBH is superior to FB and for points above the line, FB is superior to DIBH.

For tangential treatment, the median mean heart and LAD doses were reduced by 44% (1.25 to 0.71 Gy, $P < 0.001$) and 70% (8.35 to 2.47 Gy, $P < 0.001$) for DIBH compared to FB (Table 2). Regarding near-maximum doses, the $D_{2\%}$ to the heart and LAD were reduced by 61% (6.98 to 2.70 Gy, $P < 0.001$) and 87% (41.72 to 5.27 Gy, $P < 0.001$). For the ipsilateral lung, the median mean dose

TABLE 2 Comparison of dosimetric parameters between DIBH and FB for tangential and locoregional treatment, presented as median values [range] and *P*-values for paired Wilcoxon tests.

	Tangential treatment			Locoregional treatment		
	FB	DIBH	*P*	FB	DIBH	*P*
$D_{mean,heart}$	1.25 [0.39–3.28]	0.71 [0.32–1.72]	<0.001*	2.10 [0.94–6.20]	1.34 [0.62–3.05]	<0.001*
$D_{2\%,heart}$	6.98 [1.61–47.00]	2.70 [1.45–11.85]	<0.001*	13.68 [4.08–47.01]	5.05 [2.72–39.95]	<0.001*
$D_{mean,LAD}$	8.35 [2.15–26.05]	2.47 [1.58–13.81]	<0.001*	10.82 [3.75–28.06]	4.63 [2.15–13.81]	<0.001*
$D_{2\%,LAD}$	41.72 [4.14–49.59]	5.27 [2.38–47.77]	<0.001*	40.74 [8.06–48.96]	16.22 [4.38–44.00]	<0.001*
$D_{mean,lung}$	5.74 [3.30–8.26]	5.36 [2.75–9.05]	0.044*	13.32 [9.37–18.03]	11.49 [7.29–14.86]	<0.001*
$V_{20Gy,lung}$	9.66 [5.17–15.39]	8.92 [4.25–16.30]	0.025*	26.72 [17.63–39.28]	21.63 [12.18–29.60]	<0.001*
$D_{98\%,PTV}$	92.06 [90.47–92.94]	92.47 [90.58–94.64]	0.117	93.07 [91.54–93.82]	92.97 [91.48–93.86]	0.433

*Statistical significant difference ($P < 0.05$).

and V_{20Gy} were reduced from 5.74 to 5.36 Gy ($P = 0.044$) and from 9.66% to 8.92% ($P = 0.025$), respectively using DIBH, corresponding to relative reductions of 6% and 8%.

For locoregional treatment, the median mean heart and LAD doses were reduced by 36% (2.10 to 1.34 Gy, $P < 0.001$) and 57% (10.82 to 4.63 Gy, $P < 0.001$) for DIBH compared to FB (Table 2). Regarding near-maximum doses, the $D_{2\%}$ to the heart and LAD were reduced by 63% (13.68 to 5.05 Gy, $P < 0.001$) and 60% (40.74 to 16.22 Gy, $P < 0.001$). For the ipsilateral lung, the median mean dose and V_{20Gy} were reduced from 13.32 to 11.49 Gy ($P < 0.001$) and from 26.72% to 21.63% ($P < 0.001$), respectively using DIBH, corresponding to relative reductions of 14% and 19%.

3.B | Assessment of the intrafractional DIBH isocenter reproducibility

The cumulative probability of having an intrafractional DIBH isocenter reproducibility less or equal to a certain value was calculated in the lat, long, and vert directions and are presented for the two patient groups in Fig. 4. For tangential treatment, 50%/90% cumulative probabilities of having intrafractional DIBH isocenter reproducibility less or equal to 1.4/3.2, 1.1/3.1, and 0.9/2.1 mm in the lat, long, and vert directions, respectively, were observed (Fig. 4). The corresponding values for locoregional treatment were 0.6/1.8, 0.9/2.3, and 0.7/2.0 mm. The maximum values for the intrafractional DIBH isocenter reproducibility were 5.4, 5.3, and 3.8 mm (lat, long, and vert) for tangential treatment and 3.4, 5.6, and 2.7 mm for locoregional treatment (Fig. 4).

3.C | Analysis of dosimetric effects induced by intrafractional DIBH isocenter reproducibility

The dosimetric effect of the intrafractional DIBH isocenter reproducibility is presented in Table 3 and Fig. 5 for tangential treatment and in Table 4 and Fig. 6 for locoregional treatment. Large interpatient variability in the dosimetric effect of the intrafractional DIBH isocenter reproducibility was observed, for both the PTV and OARs.

The minimum values of the PTV $D_{98\%}$ were always observed when the isocenter shifts were applied in the left, cranial and anterior directions, since the combination of these directions correspond to the maximum movement of the PTV out of the treatment fields. For tangential treatment, the median values of the minimum $D_{98\%,PTV}$ decreased from 92.47% in the original DIBH plan to 92.19, 90.61, and 85.29% when isocenter shifts corresponding to the 50%, 90%, and maximum cumulative probabilities were applied (Table 3). For locoregional treatment, the corresponding values decreased from 92.97% to 92.79, 91.87, and 88.83% (Table 4).

For all OARs, the maximum values of the dosimetric parameters were always observed when the isocenter shifts were applied in the right, caudal and posterior directions, since the combination of these directions correspond to the maximum movement of the OARs into the treatment fields. Correspondingly, the minimum values of the dosimetric parameters for the OARs were always observed when the isocenter shifts were applied in the left, cranial and anterior directions, since this combination of directions correspond to a maximum separation of the OARs and the treatment fields. For example, for tangential treatment, the median values of the maximum $D_{2\%,heart}$ were increased from 2.70 Gy in the original DIBH plan to 3.00, 3.37, and 4.54 Gy when isocenter shifts corresponding to the 50%, 90%, and maximum cumulative probabilities were applied (Table 3). The corresponding values for $D_{2\%,LAD}$ increased from 5.27 Gy to 5.79, 6.83, and 9.93 Gy and the median value of the maximum $V_{20Gy,lung}$ increased from 8.92 Gy to 10.17, 11.01, and 14.08 Gy. For locoregional treatment, the median values of the maximum $D_{2\%,heart}$ were increased from 5.05 Gy in the original DIBH plan to 5.58, 7.59, and 13.55 Gy when the isocenter shifts corresponding to the 50%, 90%, and maximum cumulative probabilities were applied (Table 4). The corresponding values for $D_{2\%,LAD}$ increased from 16.22 Gy to 22.24, 33.64, and 42.37 Gy and the median value of the maximum $V_{20Gy,lung}$ increased from 21.63 Gy to 22.66, 24.40, and 26.97 Gy.

4 | DISCUSSION

This study showed that using the Catalyst™ system for DIBH treatments with visual guidance significantly reduces both the mean dose to the heart and LAD and high dose volumes, for both tangential and locoregional treatment (Fig. 2). Also, the dose to the ipsilateral lung could be reduced. This may reduce the risk of long-term

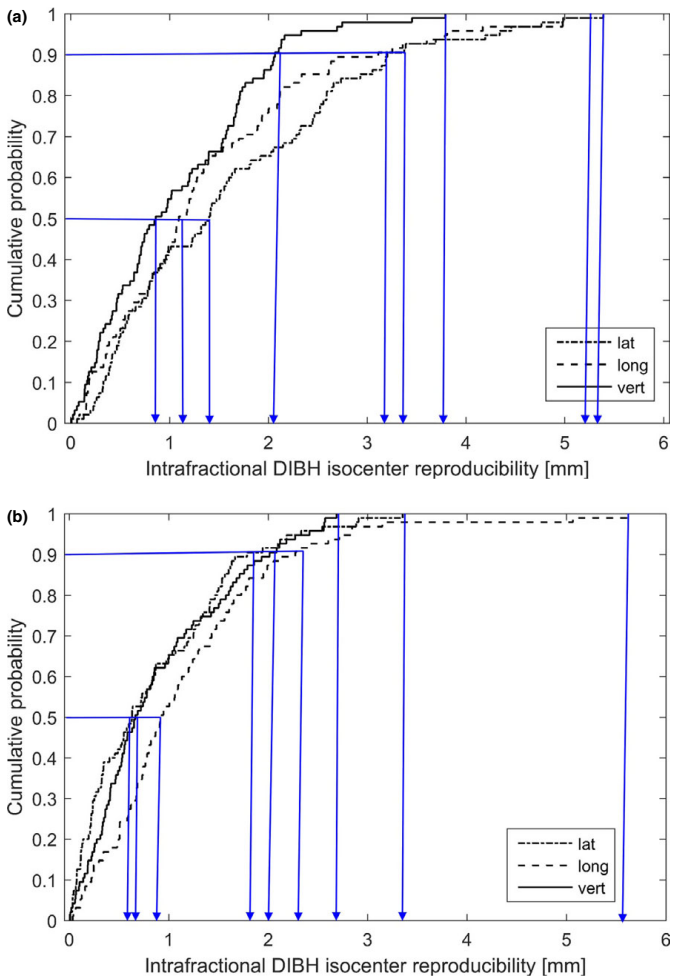

FIG. 4. Cumulative probability of the intrafractional DIBH isocenter reproducibility for the tangential treatment (a) and locoregional treatment (b). The intrafractional DIBH isocenter reproducibility in lat, long, and vert directions corresponding to the cumulative probability of 50%, 90%, and maximum value are marked with blue arrows.

cardiovascular and pulmonary mortality and morbidity. The heart and LAD dose reductions observed in this study using DIBH was comparable to the dose reductions previously observed.[13–15] Smyth et al.[14] reviewed ten treatment planning studies comparing DIBH and FB, all showing a significant reduction of the mean heart and LAD dose using DIBH. The relative reduction in the mean dose was between 38% and 65% for the heart and between 31% and 71% for LAD. The relative reductions in the mean heart dose observed in our study (44% and 36%) were in the lower part or slightly below the range presented by Smyth et al. This could, however, be explained by the fact that the absolute mean heart dose in both FB and DIBH were lower in our study compared to all studies included in the review. For the mean LAD doses, the relative reductions observed in our study (70% and 57%) were within or slightly larger than the range presented by Smyth et al.[14] However, also the mean LAD doses presented in our study were lower than the smallest values presented by Smyth et al.[14] In a large systematic review of cardiac doses by Taylor et al.,[13] it was shown that when the internal mammary node was not included in the target, the average mean dose to the heart could be reduced from 3.8 Gy in FB to 1.3 Gy using DIBH. Also, compared to that review, our study generally demonstrated lower mean heart doses. In the review by Smyth et al.,[14] there was a large variety in heart and LAD doses between the different studies, which may, for example, depend on variations in the delineation of the target and OARs and the treatment technique used, making it difficult to compare the doses from the different studies. To reduce the interobserver variability in this study, all structures were delineated by the same oncologist and all treatment plans were created by the same dosimetrist, minimizing the uncertainties in the dosimetric comparison between FB and DIBH as much as possible.

TABLE 3 The dosimetric effect of the intrafractional DIBH isocenter reproducibility for tangential treatment. The median values and ranges for the minimum and maximum values of the various dosimetric parameters for the three cumulative probability levels: 50%, 90%, and maximum (M) are presented for the isocenter-shifted plans. The corresponding values for the original DIBH plans are included for comparison.

		Isocenter shifted plan					
	Original plan	$50\%_{min}$	$50\%_{max}$	$90\%_{min}$	$90\%_{max}$	M_{min}	M_{max}
$D_{mean,heart}$	0.71 [0.32–1.72]	0.67 [0.30–1.42]	0.75 [0.34–2.08]	0.62 [0.27–1.14]	0.84 [0.38–2.72]	0.56 [0.23–0.94]	0.96 [0.43–3.71]
$D_{2\%,heart}$	2.70 [1.45–11.85]	2.50 [1.35–7.46]	3.00 [1.56–22.60]	2.31 [1.21–5.10]	3.37 [1.73–39.61]	2.09 [1.05–3.92]	4.54 [1.99–46.03]
$D_{mean,LAD}$	2.47 [1.58–13.81]	2.34 [1.51–11.48]	2.61 [1.65–16.01]	2.18 [1.40–7.94]	2.92 [1.76–18.76]	1.99 [1.25–4.34]	3.67 [1.92–21.75]
$D_{2\%,LAD}$	5.27 [2.38–47.77]	4.84 [2.27–46.34]	5.79 [2.51–48.68]	4.31 [2.10–40.93]	6.83 [2.71–49.47]	3.71 [1.93–20.00]	9.93 [3.06–49.97]
$D_{mean,lung}$	5.36 [2.75–9.05]	4.85 [2.43–8.34]	5.79 [3.09–9.76]	4.18 [2.03–7.43]	6.71 [3.55–10.73]	3.46 [1.57–6.34]	7.74 [4.18–11.97]
$V_{20Gy,lung}$	8.92 [4.25–16.30]	7.67 [3.60–14.73]	10.17 [4.96–17.89]	6.21 [2.81–12.62]	11.01 [5.99–20.02]	4.37 [1.82–10.06]	14.08 [7.41–22.75]
$D_{98\%,PTV}$	92.47 [90.58–94.64]	92.19 [30.35–94.46]	92.64 [90.66–94.73]	90.61 [87.23–94.24]	92.72 [90.73–94.79]	85.29 [55.08–92.69]	92.81 [90.83–94.76]

Comparing the results of this study and our previous study investing the benefits of enhanced inspiration gating (EIG),[15] lower relative reductions of the doses to the heart and LAD could generally be observed (except for the LAD $D_{2\%}$), which is likely because overall higher absolute doses were observed in the previous study. The reason for this may be differences in the delineations of the structures and the creation of the treatment plans, since these tasks were carried out by different physicians and dosimetrists in the two studies. A significant reduction in the lung dose for tangential treatment was observed for DIBH in this study, which was not seen for EIG in our previous study. This was also observed by Damkjær et al.[28] comparing DIBH and EIG, and is probably due to the higher breathing amplitude achieved using DIBH.

In a study by Chung et al.,[29] 32 patients underwent cardiac SPECT-CT before and after left-sided breast cancer radiotherapy, where no part of the heart was allowed inside the treatment beams. No perfusion defects were observed, which has been seen in previous studies where parts of the heart were located inside the treatment fields.[30] This may indicate that it is the inclusion of the heart in the primary beam that is of concern. It is therefore of importance to remove the entire heart from the primary beam, shown to be possible using DIBH. In this study, the number of patients with the heart completely outside the treatment fields was increased from 4 for FB to 16 for DIBH for tangential treatment and from 0 for FB to 9 for DIBH for locoregional treatment.

In this study, we have shown that it is possible to reduce OAR doses using the Catalyst™ system for DIBH treatments with visual guidance, but when using this technique, it is of utmost importance not to introduce motion-induced uncertainties during the treatment delivery. We have, therefore, assessed and estimated the dosimetric effect of intrafractional DIBH isocenter reproducibility for the two patient groups, using real-time tracking of the isocenter position during the treatment delivery. The intrafractional DIBH isocenter reproducibility was found to be very good for the majority of the treatment sessions observed in this study, with a typical median value around 1 mm (Fig. 4). These results are in the same order as reported previously from similar studies, showing discrepancies of approximately 2 mm.[20,22] In these studies, however, the surface was used as a surrogate during DIBH, and hence, the isocenter position was not investigated. However, for a few occasional treatment sessions in this study, the intrafractional DIBH isocenter reproducibility was found to be approximately 5 mm, which resulted in large effects on the target coverage and OARs doses (Tables 3 and 4, Figs. 5 and 6). However, reduced OAR doses were maintained compared to FB in most cases, with some exceptions observed for the maximum isocenter shifts. There is also motion during FB, but this has not been taken into account in this study. Despite only allowing beam-on within a 3 mm gating window based on the movement of the xiphoid process, larger differences in the isocenter position between two different DIBHs were observed, in either of the three translational directions, for 16 patients and 26 treatment sessions in total. This implies that the motion of the target volume differs from the xiphoid process, used to trigger the

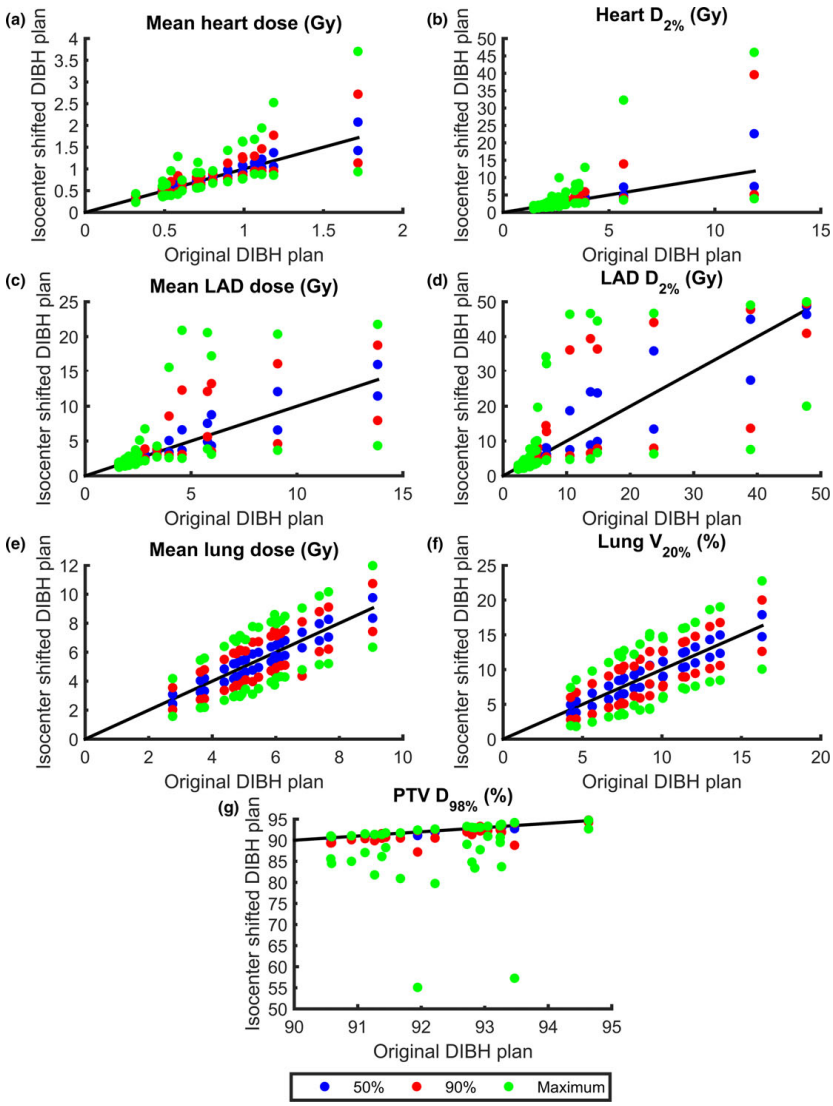

FIG. 5. The minimum and maximum values of $D_{mean,heart}$ (a), $D_{2\%,heart}$ (b), $D_{mean,LAD}$ (c), $D_{2\%,LAD}$ (d), $D_{mean,lung}$ (e), $V_{20Gy,lung}$ (f), and $D_{98\%,PTV}$ (g) for the isocenter-shifted DIBH plans versus the original DIBH plans. The results are presented for each individual patient receiving tangential treatment and for all three cumulative probability levels (50%, 90%, and maximum). The lines are for illustration purpose only, and represent where the dosimetric parameters are equal for the isocenter-shifted and original DIBH plans.

beam. Hence, it is of importance not to only perform DIBH based on the bony anatomy of the xiphoid process but also set tolerance levels on the isocenter position. Using the nonrigid algorithm, the Catalyst™ system provides the possibility to set tolerances on the allowed isocenter shift and rotation, which would be more representative of the target position. Then large isocenter shifts with the associated dosimetric impact shown in our study could be avoided. For example, using the results from our study, it can be observed that using the same tolerance of 3 mm as for xiphoid process for the isocenter shift in lat, long, and vert direction, respectively, would result in isocenter tolerance failure in 1.0%/3.2%/0.0% of the treatment sessions for locoregional treatment, and in 14.7%/

TABLE 4 The dosimetric effect of the intrafractional DIBH reproducibility for locoregional treatment. The median values and ranges for the minimum and maximum values of the various dosimetric parameters for the three cumulative probability levels: 50%, 90%, and maximum (M) are presented for the isocenter-shifted plans. The corresponding values for the original DIBH plans are included for comparison.

	Original plan	Isocenter-shifted plan					
		$50\%_{min}$	$50\%_{max}$	$90\%_{min}$	$90\%_{max}$	M_{min}	M_{max}
$D_{mean,heart}$	1.34 [0.62–3.05]	1.29 [0.59–2.77]	1.48 [0.65–3.35]	1.18 [0.55–2.30]	1.75 [0.70–3.96]	1.03 [0.50–1.85]	2.10 [0.77–4.67]
$D_{2\%,heart}$	5.05 [2.72–39.95]	4.65 [2.59–37.16]	5.58 [2.86–41.63]	4.11 [2.36–28.81]	7.59 [3.13–43.28]	3.75 [2.12–17.66]	13.55 [3.48–44.37]
$D_{mean,LAD}$	4.63 [2.15–3.81]	4.29 [2.07–12.90]	5.15 [2.24–14.95]	3.89 [1.90–10.74]	6.03 [2.19–18.93]	3.48 [1.75–8.35]	10.27 [2.86–22.28]
$D_{2\%,LAD}$	16.22 [4.38–44.00]	12.13 [4.24–43.55]	22.24 [4.60–44.38]	8.23 [4.01–42.09]	33.64 [5.22–45.90]	6.74 [3.79–38.11]	42.37 [6.62–47.25]
$D_{mean,lung}$	11.49 [7.29–14.86]	11.01 [6.84–14.33]	11.97 [7.74–15.40]	10.18 [6.08–13.39]	12.82 [8.57–16.33]	8.97 [4.16–12.18]	13.94 [9.77–17.64]
$V_{20Gy,lung}$	21.63 [12.18–29.60]	20.32 [11.03–28.33]	22.66 [13.25–30.80]	18.39 [9.33–26.24]	24.40 [15.18–32.91]	15.53 [7.04–23.45]	26.97 [17.99–35.84]
$D_{98\%,PTV}$	92.97 [91.48–93.86]	92.79 [91.20–93.72]	93.10 [91.72–93.98]	91.74 [90.36–93.30]	93.15 [91.82–94.25]	88.83 [83.80–91.15]	92.78 [91.42–93.85]

10.5%/2.1% of the treatment sessions for tangential treatments (Fig. 4).

Worse intrafractional DIBH isocenter reproducibility was observed for tangential treatment compared to locoregional treatment, probably due to the different positioning of the isocenter. For tangential treatment, the isocenter was positioned in the center of the breast, whereas for the locoregional treatment, the isocenter was positioned in the junction between the breast and the AP/PA fields. The breast is more deformable, while the junction between breast and the AP/PA fields is a more rigid structure, and therefore, the two isocenter positions move differently relative to the xiphoid process. However, the breast tissue is also a part of the PTV for the locoregional treatment. The time between the two DIBHs could potentially also be a reason for the difference in reproducibility. However, this was found to be similar for the two patient groups as the median time between the two analyzed DIBHs were 2.5 (range: 0.6–8.0) min and 2.3 (0.5–9.5) min for tangential and locoregional treatment, respectively.

Large interpatient variability in the dosimetric effect was observed (Figs. 5 and 6), especially for heart and LAD, due to differences in the patient anatomy and the placement of the treatment fields relative to the target volume and OARs in the original plan. For some patients, the heart and LAD were well out of the treatment fields in the original DIBH plan. For these cases, the applied isocenter shifts did not bring the heart and LAD into the treatment fields and hence only small dosimetric effects were observed. Similarly, for some patients, a large part of the heart and LAD was already inside the treatment fields in the original DIBH plan and the applied isocenter shifts did not bring the heart and LAD out of the treatment fields. The largest dosimetric effects were observed for the patients where the treatment field edges were contiguous with the edge of the heart and LAD, since for these patients, the applied isocenter shifts would either bring the heart and LAD into or out of the treatment fields. This effect was most pronounced for $D_{2\%}$, since this represents the near-maximum dose. In Figs. 5 and 6, it can also be observed that the dosimetric effect of the applied isocenter shifts is not symmetrical for $D_{98\%,PTV}$. Underdosage is more common than overdosage, since target coverage will remain (but not increase) if the isocenter shifts result in the treatment fields being located too deep. However, if the treatment fields are too shallow, the $D_{98\%,PTV}$ will decrease rapidly, resulting in an underdosage of the target volume. To reduce the OAR and target volume dose deviations for individual treatment sessions, it would be of great importance to introduce tolerances for the isocenter deviation, which could, for example, correspond to the 90% cumulative probability level. If such tolerance is applied, the results from this study show that the dose deviations for the maximum and 90% cumulative probability level compared to the original plan could be reduced from 35% to 18% for the median $D_{mean,heart}$, 68% to 25% for the median $D_{2\%,heart}$, 49% to 18% for the median $D_{mean,LAD}$, and 88% to 30% for the median $D_{2\%,LAD}$ for tangential treatment (Table 3). The corresponding values for locoregional treatment were 57% to 31% for the median $D_{mean,heart}$, 168% to 50% for the median $D_{2\%,heart}$, 122% to 30%

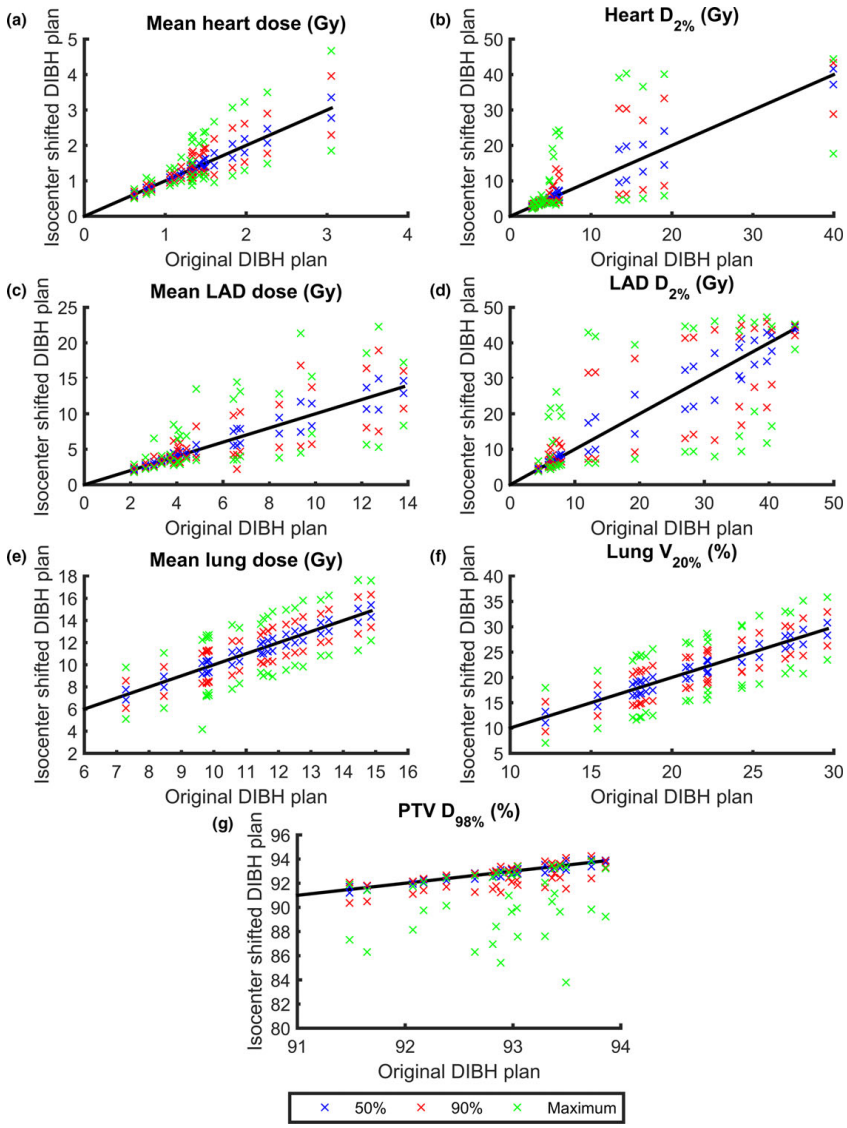

FIG. 6. The minimum and maximum values of $D_{mean,heart}$ (a), $D_{2\%,heart}$ (b), $D_{mean,LAD}$ (c), $D_{2\%,LAD}$ (d), $D_{mean,lung}$ (e), $V_{20Gy,lung}$ (f), and $D_{98\%,PTV}$ (g) for the isocenter-shifted DIBH plans versus the original DIBH plans. The results are presented for each individual patient receiving locoregional treatment and for all three cumulative probability levels (50%, 90%, and maximum). The lines are for illustration purpose only, and represent where the dosimetric parameters are equal for the isocenter-shifted and original DIBH plans.

for the median $D_{mean,LAD}$, and 161% to 107% for the median $D_{2\%,LAD}$ (Table 4). Also, the minimum deviations in the median $D_{98\%,PTV}$ could be reduced from 8% to 2% and from 4% to 1% for tangential and locoregional treatment, respectively (Tables 3 and 4).

One limitation of this study is that the dosimetric effect of the intrafractional DIBH isocenter reproducibility was estimated using isocenter shifts in the TPS. When performing isocenter shifts a rigid motion is assumed, that is, the whole patient moves the

corresponding isocenter shift and the distance between the heart and target volume is thus kept constant. This is actually not true since the distance between the heart and target volume changes with breathing. Using a deformable patient model would probably improve the accuracy of these calculations. But since the isocenter shifts were rather small (in the order of a few millimeter), we believe our calculations still gives a reasonable approximation of the dosimetric effect.

The analysis of this study was population based, using the cumulative probability of the intrafractional DIBH isocenter reproducibility to simulate the dosimetric effects for each patient plan. Hence, the dosimetric effect of each patient's individual isocenter reproducibility was not simulated. The maximum intrafractional DIBH isocenter reproducibility represents the worst-case scenario for the entire population and deviations of this magnitude were only observed for a few percent of the DIBHs. The results in this study are based on the assumption that the isocenter reproducibility was the same for every DIBH, which of course is not the case. Slightly different isocenter positions will be obtained for each DIBH throughout the treatment, resulting in a small blurring of the dose distribution. The total delivered dose to the patient would, therefore, most likely differ less from the planned dose than the result presented in this study. The 50% cumulative probability level would probably be a more realistic representation of the dosimetric effects caused by the intrafractional DIBH isocenter reproducibility for an entire treatment.

Overall, using the xiphoid process as a surrogate for the breast tissue during DIBH was found to be reproducible (Fig. 4). Gierga et al.[22] reported that 22% of the DIBHs were out of a 5 mm tolerance using the breast surface to trigger the beam when a rigid match algorithm and audio coaching were used. If using a 5 mm tolerance in either lat, long, or vert direction in this study, only 2% of the DIBH would be out of tolerance for locoregional treatments and 1% for tangential treatments. This implies that using the xiphoid process as a surrogate for the breast tissue improved the intrafractional DIBH isocenter reproducibility compared to using the breast surface. And according to this study, the intrafractional DIBH isocenter reproducibility could be improved even further by introducing tolerances on the isocenter position.

5 | CONCLUSION

Deep inspiration breath-hold (DIBH) treatments for breast cancer radiotherapy, using the optical surface scanning system Catalyst™ including visual guidance, reduces the absorbed doses to the heart, LAD, and ipsilateral lung in accordance to previous studies, which may reduce the risk of long-term cardiovascular and pulmonary mortality and morbidity.

Excellent intrafractional DIBH isocenter reproducibility was observed for the majority of the treatment sessions for both tangential and locoregional treatment. However, values of the intrafractional DIBH isocenter reproducibility up to approximately 5 mm were seen for some treatment sessions, which resulted in large dosimetric effects, primarily for the OARs. Hence, it is of importance to set tolerance levels on the intrafractional isocenter motion and not only perform DIBH based on the motion of the bony anatomy of the xiphoid process.

CONFLICT OF INTEREST

All authors approved the final manuscript, and declared that they have no potential conflicts of interest to this work.

DECLARATION OF INTEREST

Our research is partly financially supported by C-RAD AB, Uppsala, Sweden, however, the authors alone are responsible for the content, analyses, and writing.

REFERENCES

1. Early Breast Cancer Trialists' Collaborative Group. Effect of radiotherapy after breast-conserving surgery on 10-year recurrence and 15-year breast cancer death: meta-analysis of individual patient data for 10 801 women in 17 randomised trials. *Lancet*. 2011;378:1707–1716.
2. Early Breast Cancer Trialists' Collaborative Group. Effect of radiotherapy after mastectomy and axillary surgery on 10-year recurrence and 20-year breast cancer mortality: meta-analysis of individual patient data for 8135 women in 22 randomised trials. *Lancet*. 2014;383:2127–2135.
3. Darby SC, McGale P, Taylor CW, Peto R. Long-term mortality from heart disease and lung cancer after radiotherapy for early breast cancer: prospective cohort study of about 300 000 women in US SEER cancer registries. *Lancet Oncol*. 2005;6:557–565.
4. Early Breast Cancer Trialists' Collaborative Group. Effects of radiotherapy and of differences in the extent of surgery for early breast cancer on local recurrence and 15-year survival: an overview of the randomised trials. *Lancet*. 2005;366:2087–2106.
5. Darby SC, Ewertz M, McGale P, et al. Risk of ischemic heart disease in women after radiotherapy for breast cancer. *N Engl J Med*. 2013;368:987–998.
6. Giordano SH, Kuo YF, Freeman JL, Buchholz TA, Hortobagyi GN, Goodwin JS. Risk of cardiac death after adjuvant radiotherapy for breast cancer. *J Natl Cancer Inst*. 2005;97:419–424.
7. Boero IJ, Paravati AJ, Triplett DP, et al. Modern radiation therapy and cardiac outcomes in breast cancer. *Int J Radiat Oncol Biol Phys*. 2016;94:700–708.
8. van den Bogaard VA, Ta BD, van der Schaaf A, et al. Validation and modification of a prediction model for acute cardiac events in patients with breast cancer treated with radiotherapy based on three-dimensional dose distributions to cardiac substructures. *J Clin Oncol*. 2017;35:1171–1178.
9. Boekel NB, Schaapveld M, Gietema JA, et al. Cardiovascular disease risk in a large, population-based cohort of breast cancer survivors. *Int J Radiat Oncol Biol Phys*. 2016;94:1061–1072.
10. Nilsson G, Holmberg L, Garmo H, et al. Distribution of coronary artery stenosis after radiation for breast cancer. *J Clin Oncol*. 2011;30:380–386.
11. American Cancer Society. *Breast Cancer Facts and Figures 2011-2012*. https://www.cancer.org/content/dam/cancer-org/research/cancer-facts-and-statistics/breast-cancer-facts-and-figures/breast-cancer-facts-and-figures-2011-2012.pdf. Accessed June 7, 2017.

12. Shah C, Badiyan S, Berry S, et al. Cardiac dose sparing and avoidance techniques in breast cancer radiotherapy. *Radiother Oncol*. 2014;112:9–16.
13. Taylor CW, Wang Z, Macaulay E, Jagsi R, Duane F, Darby SC. Exposure of the heart in breast cancer radiation therapy: a systematic review of heart doses published during 2003 to 2013. *Int J Radiat Oncol Biol Phys*. 2015;93:845–853.
14. Smyth LM, Knight KA, Aarons YK, Wasiak J. The cardiac dose-sparing benefits of deep inspiration breath-hold in left breast irradiation: a systematic review. *J Med Radiat Sci*. 2015;62:66–73.
15. Edvardsson A, Nilsson MP, Amptoulach S, Ceberg S. Comparison of doses and NTCP to risk organs with enhanced inspiration gating and free breathing for left-sided breast cancer radiotherapy using the AAA algorithm. *Radiat Oncol*. 2015;10:84.
16. Wiant D, Wentworth S, Liu H, Sintay B. How important is a reproducible breath hold for deep inspiration breath hold breast radiation therapy? *Int J Radiat Oncol Biol Phys*. 2015;93:901–907.
17. Bergh L. Breathing adapted radiotherapy of breast cancer: Investigation of two different gating techniques and visual guidance, using optical surface scanning and pressure monitoring. http://lup.lub.lu.se/luur/download?func=downloadFile&recordOId=4623050&fileOId=4647706. Accessed June 7, 2017.
18. Cervino LI, Gupta S, Rose MA, Yashar C, Jiang SB. Using surface imaging and visual coaching to improve the reproducibility and stability of deep-inspiration breath hold for left-breast-cancer radiotherapy. *Phys Med Biol*. 2009;54:6853–6865.
19. Boda-Heggemann J, Knopf AC, Simeonova-Chergou A, et al. Deep inspiration breath hold-based radiation therapy: a clinical review. *Int J Radiat Oncol Biol Phys*. 2016;94:478–492.
20. Tang X, Zagar TM, Bair E, et al. Clinical experience with 3-dimensional surface matching-based deep inspiration breath hold for left-sided breast cancer radiation therapy. *Pract Radiat Oncol*. 2014;4:e151–e158.
21. Padilla L, Kang H, Washington M, Hasan Y, Chmura SJ, Al-Hallaq H. Assessment of interfractional variation of the breast surface following conventional patient positioning for whole-breast radiotherapy. *J Appl Clin Med Phys*. 2014;15:4921.
22. Gierga DP, Turcotte JC, Sharp GC, Sedlacek DE, Cotter CR, Taghian AG. A voluntary breath-hold treatment technique for the left breast with unfavorable cardiac anatomy using surface imaging. *Int J Radiat Oncol Biol Phys*. 2012;84:e663–e668.
23. Tang X, Cullip T, Dooley J, et al. Dosimetric effect due to the motion during deep inspiration breath hold for left-sided breast cancer radiotherapy. *J Appl Clin Med Phys*. 2015;16:91–99.
24. Nutti B, Kronander Å, Nilsing M, Maad K, Svensson C, Li H. Depth sensor-based realtime tumor tracking for accurate radiation therapy. *Eurographics*. 2014;10–13.
25. Li H, Sumner R, Pauly M. Global correspondence optimization for non-rigid registration of depth scans. *Comput Graph Forum*. 2008;27:1421–1430.
26. Schonecker S, Walter F, Freislederer P, et al. Treatment planning and evaluation of gated radiotherapy in left-sided breast cancer patients using the Catalyst™/Sentinel™ system for deep inspiration breath-hold (DIBH). *Radiat Oncol*. 2016;11:143.
27. Stieler F, Wenz F, Shi M, Lohr F. A novel surface imaging system for patient positioning and surveillance during radiotherapy. A phantom study and clinical evaluation. *Strahlenther Onkol*. 2013;189:938–944.
28. Damkjaer SM, Aznar MC, Pedersen AN, Vogelius IR, Bangsgaard JP, Josipovic M. Reduced lung dose and improved inspiration level reproducibility in visually guided DIBH compared to audio coached EIG radiotherapy for breast cancer patients. *Acta Oncol*. 2013;52:1458–1463.
29. Chung E, Corbett JR, Moran JM, et al. Is there a dose-response relationship for heart disease with low-dose radiation therapy? *Int J Radiat Oncol Biol Phys*. 2013;85:959–964.
30. Marks LB, Yu X, Prosnitz RG, et al. The incidence and functional consequences of RT-associated cardiac perfusion defects. *Int J Radiat Oncol Biol Phys*. 2005;63:214–223.

Paper III

ACTA ONCOLOGICA
https://doi.org/10.1080/0284186X.2018.1512153

Taylor & Francis
Taylor & Francis Group

ORIGINAL ARTICLE

OPEN ACCESS Check for updates

Comparative treatment planning study for mediastinal Hodgkin's lymphoma: impact on normal tissue dose using deep inspiration breath hold proton and photon therapy

Anneli Edvardsson[a]*, Malin Kügele[a,b]*, Sara Alkner[b], Marika Enmark[b], Joakim Nilsson[b], Ingrid Kristensen[b], Elisabeth Kjellén[b], Silke Engelholm[b] and Sofie Ceberg[a,b]

[a]Department of Medical Radiation Physics, Clinical Sciences, Lund University, Lund, Sweden; [b]Department of Hematology, Oncology and Radiation Physics, Skane University Hospital, Lund, Sweden

ABSTRACT

Background: Late effects induced by radiotherapy (RT) are of great concern for mediastinal Hodgkin's lymphoma (HL) patients and it is therefore important to reduce normal tissue dose. The aim of this study was to investigate the impact on the normal tissue dose and target coverage, using various combinations of intensity modulated proton therapy (IMPT), volumetric modulated arc therapy (VMAT) and 3-dimensional conformal RT (3D-CRT), planned in both deep inspiration breath hold (DIBH) and free breathing (FB).

Material and methods: Eighteen patients were enrolled in this study and planned with involved site RT. Two computed tomography images were acquired for each patient, one during DIBH and one during FB. Six treatment plans were created for each patient; 3D-CRT in FB, 3D-CRT in DIBH, VMAT in FB, VMAT in DIBH, IMPT in FB and IMPT in DIBH. Dosimetric impact on the heart, left anterior descending (LAD) coronary artery, lungs, female breasts, target coverage, and also conformity index and integral dose (ID), was compared between the different treatment techniques.

Results: The use of DIBH significantly reduced the lung dose for all three treatment techniques, however, no significant difference in the dose to the female breasts was observed. Regarding the heart and LAD doses, large individual variations were observed. For VMAT, the mean heart and LAD doses were significantly reduced using DIBH, but no significant difference was observed for 3D-CRT and IMPT. Both IMPT and VMAT resulted in improved target coverage and more conform dose distributions compared to 3D-CRT. IMPT generally showed the lowest organs at risk (OAR) doses and significantly reduced the ID compared to both 3D-CRT and VMAT.

Conclusions: The majority of patients benefited from treatment in DIBH, however, the impact on the normal tissue dose was highly individual and therefore comparative treatment planning is encouraged. The lowest OAR doses were generally observed for IMPT in combination with DIBH.

ARTICLE HISTORY
Received 13 March 2018
Accepted 5 August 2018

Introduction

There has been a tremendous development in the treatment of Hodgkin's lymphoma (HL) the last couple of decades, primarily through the introduction of combined modality treatment consisting of both chemotherapy and radiotherapy (RT), resulting in survival rates above 90% [1,2]. Due to the relatively high survival rate and young age for most HL patients, a large proportion of the patients become long-time survivors and hence late effects of the treatment are of great concern. Previously, extended field radiotherapy (EFRT) and involved field radiotherapy (IFRT) were used to treat entire nodal stations, which has been shown to result in increased mortality from late effects, most commonly from secondary cancer, cardiovascular diseases and respiratory diseases [3–6]. Modern HL treatment has focused on reducing the risk of late effects while still maintaining high disease control [7]. This has been achieved through reducing the prescribed dose [1,2], and the irradiated volume, by introducing the involved node radiotherapy (INRT) and involved site radiotherapy (ISRT) concepts where only the initially involved lymph nodes are included in the target [8]. Also, more advanced image guidance and conform treatment techniques, such as 3-dimensional conformal radiation therapy (3D-CRT), intensity modulated radiation therapy (IMRT), volumetric modulated arc therapy (VMAT) and helical tomotherapy, have been introduced in HL RT [9–11]. The dynamic treatment techniques provide a very conformal high-dose distribution, however at the expense of larger healthy tissue volumes being irradiated to low doses. Hence, new techniques that enable a reduction of the normal tissue irradiation for all dose levels would be desirable. Deep inspiration breath hold (DIBH) has demonstrated the ability to reduce

CONTACT Sofie Ceberg Sofie.Ceberg@med.lu.se Department of Hematology, Oncology and Radiation Physics, Skane University Hospital, Lund, Sweden
*Both authors contributed equally to this work.

© 2018 The Author(s). Published by Informa UK Limited, trading as Taylor & Francis Group.
This is an Open Access article distributed under the terms of the Creative Commons Attribution-NonCommercial-NoDerivatives License (http://creativecommons.org/licenses/by-nc-nd/4.0/), which permits non-commercial re-use, distribution, and reproduction in any medium, provided the original work is properly cited, and is not altered, transformed, or built upon in any way.

dose to healthy tissue for mediastinal HL, due to favorable anatomical changes in tumor position in relation to healthy tissue [12–16]. Also, proton therapy (PT) has shown a positive impact on the normal tissue dose compared to photon therapy [6,17–19]. Most studies for mediastinal HL have used the passive scattering technique, however, more modern PT, using pencil beam scanning (PBS) and intensity modulated PT (IMPT), enables even more conformal treatment plans. Also, automatic beam triggering is nowadays available for PT, enabling gated beam delivery in DIBH [20]. To our knowledge, only two previous treatment planning studies exist on the use of both PT and DIBH for mediastinal HL, showing an overall benefit for the combined use of the techniques [21,22]. Thus, further investigations of the combined use of PT and DIBH are highly desirable. The aim of this study was to investigate the impact on the normal tissue dose and target coverage, using various combinations of IMPT, VMAT and 3D-CRT planned in both DIBH and free breathing (FB). To our knowledge, no previous study exists that have investigated all these treatment techniques in both FB and DIBH for mediastinal HL.

Material and methods

Patients

Between April 2014 and June 2017, 19 patients with mediastinal HL were enrolled in this retrospective comparative dose planning study. One patient was excluded from the study because the target volumes were not deemed comparable between the two computed tomography (CT) images acquired due to insufficient image quality. Table 1 provides the detailed characteristics of the patient cohort, including age, gender, stage and disease location. The patients were classified as unfavorable if they had one or more risk factors according to the Swedish national treatment guidelines for HL (www.cancercentrum.se). Risk factors for stage IA and IIA are bulky disease, >2 involved sites and erythrocyte sedimentation rate ≥ 50. Risk factors for stage IIB-IV are male, <45 years, stage IV, hemoglobin <105 g/L, S-albumin <40 g/L, leukocytes $>15 \times 10^9$/L and B-lymphocytes $<8\%$ or $<0.6 \times 10^9$/L. Residual PET-positive disease after chemotherapy was also considered a risk factor. Only disease above the diaphragm was included in this study.

Table 1. Patient and disease characteristics.

Age, median (range)	34 (15–71)
Gender	
Female	10
Male	8
Stage	
IIA	9 (7[a])
IIB	3 (3[a])
III	4 (4[a])
IV	1 (1[a])
Recurrence	1
Disease location	
Mediastinum	3
Mediastinum + fscl	5
Mediastinum + fscl + neck	7
Mediastinum + fscl + neck + axilla	3

fscl: supraclavicular fossa.
[a]Unfavorable disease.

Ethical consideration

The use of the RT database for retrospective research has been approved by the committee of the Regional Ethical Review Board in Lund (No. 2013/742).

CT imaging and deep inspiration breath hold techniques

Two CT images were acquired for treatment planning and dosimetric comparison purposes, one during DIBH and one during FB. The patients were positioned supine, generally in immobilizing fullbody vacuum bags, with the arms positioned above the head. However, two patients were positioned with the arms along the side of the body. The CT images were acquired using a Siemens Somatom definition AS plus (Siemens Medical Solutions, Erlangen, Germany) with a slice thickness of 3 mm. For improved image quality, contrast-enhanced CT (60 ml, Visipaque^{TM} 270 mg I/ml, Iodixanol, GE Healthcare AS, Oslo, Norway) was acquired for eight of the patients, two in FB and six in DIBH.

The real-time position management (RPM) system (Varian Medical Systems, Palo Alto, CA) or the optical surface scanning system Sentinel (C-rad Positioning AB, Uppsala, Sweden) was used to track the respiratory motion for the CT scan in DIBH. The RPM system and the Sentinel system have previously been described elsewhere [23,24]. All patients were trained by an oncology nurse to perform deep inspiration at a comfortable and reproducible level prior to the CT scan. For the first 10 patients, audio-coached enhanced inspiration gating (EIG) was used in combination with the RPM-system to acquire the DIBH CT images [23]. The patients were repeatedly deep breathing for approximately 4–5 seconds throughout the CT scan. For each inspiration, a smaller sequenced segment of the CT scan length was acquired with an axial CT scan mode. These segments were appended to each other to assess the full scan volume. For the remaining eight patients, the Sentinel system was used to acquire the DIBH CT images, using both audio and visual guidance [24]. A helical CT scan was acquired during a single DIBH. For all patients, the respiratory motion was tracked at sternum, at the surface above the xiphoid process. The median deep inspiration amplitude was 11.7 mm (range 9.0–20.7 mm) and the median gating window was 3.2 mm (range 2.7–4.3 mm). The same criteria for the amplitude and gating window were used for all patients in this study, regardless of the breathing technique or gating system used, resulting in equal DIBH CT images. Both EIG and DIBH are therefore referred to as DIBH.

Contouring

Target volumes were delineated using the ISRT technique [8], based on a 18F-fluoro-deoxyglucose (FDG) positron emission tomography (PET)/CT image acquired during FB (GE Discovery 690, General Electric Healthcare and Philips Gemini

TF 16, Philips Medical Systems, Amsterdam, Netherlands). The information from the PET images were transferred to the FB and DIBH planning CTs through visual comparison between the images. All structures were delineated in both the DIBH and FB CT-sets by the same radiation oncologist. The clinical target volume (CTV) was defined as involved lymph node stations, to which radiation treatment was warranted. The median CTV volume was 338 cm^3 (range 124–1530 cm^3) in FB and 341 cm^3 (range 123–1381 cm^3) in DIBH. A planning target volume (PTV) was constructed with an 8 mm isotropic margin to CTV, and cropped 4 mm from the skin surface. The organs at risk (OAR) delineated were the heart, the left anterior descending (LAD) coronary artery, lungs, and for female patients also the breasts. The lungs were automatically delineated using the segmentation wizard in the treatment planning system (TPS, Eclipse, version 13.6, Varian Medical Systems, Palo Alto, CA) and then manually verified. All other structures were delineated manually. The heart was defined as the entire myocardium including the big vessels up to the departure of the coronary arteries from aorta ascendens. LAD was delineated with a 6 mm diameter from the vessels departure from aorta as far as it could be visualized, often to the middle of the heart. The female breasts were outlined as the clinical limits of the breast, including all glandular tissue and cropped 5 mm from the skin surface. All OARs were delineated without margins.

Treatment planning

Six treatment plans were created for each patient; 3D-CRT in FB, 3D-CRT in DIBH, VMAT in FB, VMAT in DIBH, IMPT in FB and IMPT in DIBH, resulting in a total of 108 treatment plans. All treatment plans were created in the Eclipse TPS (version 13.6, Varian Medical Systems, Palo Alto, CA). The prescribed dose was 29.75 Gy/Gy(RBE) (relative biological equivalent) in 17 fractions normalized to the mean dose of the PTV, assuming a constant RBE of 1.1 for protons. The main goals creating the treatment plans were that 100% of the PTV volume should be covered by 95% of the prescribed dose, while the volume receiving more than 105% of the prescribed dose was minimized. At the same time, the dose to the OARs was kept as low as possible. To achieve the best possible dose distributions, each treatment plan was individually optimized.

3 D-CRT plans

For the 3D-CRT plans, two 6 MV anterior–posterior/posterior–anterior (AP/PA) parallel opposed fields were generally used (gantry angles 0° and 180°), with a PTV-to-field-edge margin of 7 mm. To individually optimize each plan, the beams were weighted and if needed wedges and/or supplementary fields (6 or 10 MV) were used to improve dose homogenization in the target volume. The 3D-CRT plans were generated for either a TrueBeam linear accelerator (version 2.0, Varian Medical Systems, Palo Alto, CA) or an Elekta Synergy linear accelerator (Elekta AB, Stockholm, Sweden). The Anisotropic Analytical Algorithm (AAA, version 13.6) was used for dose calculation.

VMAT plans

Basic VMAT plans with standard arc geometries were created. All plans were created with 6 MV using two, three or four arcs depending on patient anatomy and PTV volume. Depending on the resulting field size (*x*-direction), some fields were modified so that the field size in the *x*-direction for any given arc had a maximum size of 15 cm. For arcs with field size (*x*-direction) less or equal to 15 cm two arcs were typically used. For modified arcs with original field size larger than 15 cm, a third arc was typically added to maintain plan quality. In one case with a very large PTV, four arcs were used. All plans were optimized using the Photon Optimizer (version 13.6) for a TrueBeam linear accelerator and final dose was calculated with AAA (version 13.6). Full arcs with collimator angles 5° and 355° were typically used, but for lateral targets where full arcs would cause collision with the patient or couch the arc length was modified. In one case with four arcs collimator rotation 85° and 95° in addition to the standard 5° and 355° mentioned above were used.

IMPT plans

Either AP/PA fields (12 patients) or two oblique AP fields in 10° and 350° (six patients) were used, whichever was considered most beneficial for the individual patient. During optimization, constraints were assigned to the PTV and all OARs. The highest priority was set for the PTV and thereafter the heart, LAD and lungs had equal priority. The priority for the female breasts differed slightly between the AP/PA plans and the plans with two oblique AP fields. For the AP/PA plans, the priority was the same as for the heart, LAD and lungs. In the plans with two oblique AP fields, the female breasts had a slightly higher priority than the other OARs, since both fields passed through the breast tissue. High density materials, such as medical implants or contrast agent, were replaced with water equivalent structures for dose calculation purposes. The IMPT plans were created for an IBA PT System (Proteus Plus, IBA, Louvain-la-Neuve, Belgium) with a PBS beam delivery. The Proton Convolution Superposition algorithm (PCS, version 13.7) was used for dose calculation, with beam data from the Swedish proton center, the Skandion clinic (Uppsala, Sweden).

For the IMPT plans, additional margins for the range uncertainty was calculated as 3.5% of the range to the distal edge of the CTV plus 1 mm. If the range uncertainty exceeded the CTV-to-PTV margin of 8 mm, an additional margin was added. Otherwise the same PTV as for the photon plans was used. For the PA field for one patient in FB and four patients in DIBH, the distal margin exceeded the CTV-to-PTV margin by 1 mm and thus the margin was expanded 1 mm in this direction.

Treatment

All patients managed the DIBH CT acquisition and were clinically treated with a 3D-CRT plan in either DIBH or FB, whichever was considered most beneficial for the patient. Ten patients were treated using DIBH 3D-CRT and the remaining

eight patients with FB 3D-CRT. During EIG and DIBH treatment, the respiratory motion was tracked with the TrueBeam integrated gating systems, Polaris Spectra infrared camera (Northern Digital Medical, Waterloo, Canada) or the optical surface scanning system Catalyst (C-rad Positioning AB, Uppsala, Sweden) [24]. The patient position was verified with orthogonal X-ray imaging or cone beam CT (CBCT). The CBCTs were acquired during three or four DIBHs.

Dosimetric and statistical analysis

Dose volume histograms (DVH) were extracted for all treatment plans from the TPS, and average DVHs for all patients were calculated for all the treatment techniques. To compare the dose distributions for the different treatment techniques, the mean dose to the heart ($D_{mean,heart}$), LAD ($D_{mean,LAD}$), lungs ($D_{mean,lungs}$), right breast ($D_{mean,right\ breast}$) and left breast ($D_{mean,left\ breast}$), the dose received by 2% of the heart and LAD volumes ($D_{2\%,heart}$ and $D_{2\%,LAD}$), the lung volume receiving 5 and 20 Gy ($V_{5Gy,lungs}$ and $V_{20Gy,lungs}$) and the CTV and PTV volume covered by 95% of the prescribed dose ($V_{95\%,CTV}$ and $V_{95\%,PTV}$) were retrieved. For comparison of the PTV dose uniformity, the heterogeneity index (HI) was calculated (Equation (1)).

$$HI = \frac{D_{2\%} - D_{98\%}}{D_{mean}} \quad (1)$$

where $D_{2\%}$ and $D_{98\%}$ are the doses to 2% and 98% of the volume, respectively.

Further, to compare the dose to healthy tissue between the 3D-CRT, VMAT and IMPT plans the integral dose (ID) was evaluated (Equation (2)).

$$ID = \rho \cdot V \cdot D_{mean} \quad (2)$$

where ρ is the density and V is the volume. The ID was calculated for the full CT scanned body volume excluding the PTV volume and was corrected for the lung density. Generic density values of 0.26 g/cm^3 for the lung and 1.06 g/cm^3 for all other tissues were used [25].

The plan conformity was evaluated using Paddick's conformity index ($CI_{Paddick}$) [26] (Equation (3)).

$$CI_{Paddick} = \frac{TV_{PIV}^2}{TV \cdot PIV} \quad (3)$$

where TV is the target volume, PIV is the prescription isodose volume and TV_{PIV} is the target volume covered by the prescription isodose. In this study, the TV corresponds to the PTV and PIV the 95% isodose volume. A perfectly conformal plan has a $CI_{Paddick}$ value of 1.

Friedman tests were carried out to investigate if there were any statistical significant differences between the six different treatment techniques (FB 3D-CRT, DIBH 3D-CRT, FB VMAT, DIBH VMAT, FB IMPT and DIBH IMPT). If a statistically significant difference was observed, post hoc two-sided paired Wilcoxon's tests were carried out. A significance level of 0.05 was used. Multiple testing was not accounted for because it was considered too conservative due to the large number of comparisons.

All dosimetric and statistical analyses were performed in Matlab (R2014b, Mathworks, Natick, MA).

Results

All dosimetric parameters are presented in Table 2 and the average DVHs for the target volumes and OARs are presented in Figure 1. The mean OAR doses for each individual patient are presented in Figure 2, where a large variation in the OAR doses between the individual patients can be observed.

Comparison of DIBH and FB

Lungs

Regarding the lung dose, the vast majority of patients benefited from DIBH, with reduced $D_{mean,lungs}$ for 94, 83 and 94% of the patients for 3D-CRT, VMAT and IMPT, respectively (Figure 2(a)). For 3D-CRT, VMAT and IMPT the median $D_{mean,lungs}$, $V_{20Gy,lungs}$ and $V_{5Gy,lungs}$ were significantly reduced by approximately 10–20% for DIBH compared to FB.

Heart and LAD

Regarding both the heart and LAD doses, the benefit of using DIBH varied substantially between the patients (Figure 2(b,c)). The median $D_{mean,heart}$ and $D_{mean,LAD}$ were reduced by approximately 10–40% and 10–60%, respectively, for DIBH compared to FB, however, this difference only reached statistical significance for VMAT. For DIBH compared to FB, both the $D_{mean,heart}$ and $D_{mean,LAD}$ decreased for 61% of the patients for 3D-CRT and IMPT, and 72% of the patients for VMAT. No significant differences in $D_{2\%,heart}$ and $D_{2\%,LAD}$ were observed between DIBH and FB for neither 3D-CRT, VMAT nor IMPT.

Breasts

There was no significant difference in the median $D_{mean,right\ breast}$ and $D_{mean,left\ breast}$ between DIBH and FB for neither 3D-CRT, VMAT nor IMPT.

Target coverage

Very similar target coverage was achieved between DIBH and FB for all treatment techniques (Figure 1(a,b)). For 3D-CRT and VMAT, no significant difference was observed in $V_{95\%,CTV}$ or $V_{95\%,PTV}$ between DIBH and FB. For IMPT, however, small but statistically significant decreases in $V_{95\%,CTV}$ and $V_{95\%,PTV}$ were observed for DIBH.

Comparison of IMPT, VMAT and 3D-CRT

Lungs

For both DIBH and FB, the lowest median $D_{mean,lungs}$ was observed for IMPT, followed by VMAT and 3D-CRT (Figure 2(a)). The $D_{mean,lungs}$ was reduced by approximately 40% and 20–30% for IMPT compared to 3D-CRT and VMAT, respectively.

Table 2. Dosimetric parameters for free breathing (FB) and deep inspiration breath hold (DIBH) 3-dimensional conformal radiation therapy (3D-CRT), volumetric modulated arc therapy (VMAT) and intensity modulated proton therapy (IMPT).

Parameter	FB 3D-CRT	DIBH 3D-CRT	FB VMAT	DIBH VMAT	FB IMPT	DIBH IMPT	*p* value Friedman
$V_{95\%,CTV}$ (%)	97.7 [90.9–100.0][c,d,e,f]	97.3 [91.1–99.9][c,d,e,f]	100.0 [100.0–100.0][a,b,e,f]	100.0 [100.0–100.0][a,b,e,f]	99.9 [97.8–100.0][a,b,c,d,f]	99.6 [98.4–100.0][a,b,c,d,e]	<.001
$V_{95\%,PTV}$ (%)	91.9 [85.3–99.2][c,d,e,f]	90.2 [84.7–98.5][c,d,e,f]	98.0 [96.1–99.5][a,b,e]	98.0 [96.5–99.2][a,b,e]	99.4 [97.2–99.8][a,b,c,d,f]	98.8 [96.1–99.7][a,b,e]	<.001
HI_{PTV} (%)	14.1 [8.8–18.9][c,d,e,f]	15.0 [9.2–17.6][c,d,e,f]	7.7 [5.5–9.9][a,b,e]	7.8 [5.7–10.0][a,b,e]	6.3 [4.3–9.5][a,b,c,d,f]	7.5 [4.2–11.3][a,b,e]	<.001
$D_{mean,Heart}$ (Gy/Gy(RBE))	8.8 [0.5–22.9][c,d,e,f]	7.7 [0.5–27.3][d,e,f]	6.7 [0.4–18.3][a,d,e,f]	5.3 [0.5–20.6][a,b,c,f]	6.1 [0.0–17.6][a,b,c]	3.8 [0.1–20.9][a,b,c,d]	<.001
$D_{2\%,Heart}$ (Gy/Gy(RBE))	29.2 [1.3–30.5]	29.1 [1.4–30.7]	29.8 [1.1–30.8]	29.5 [1.2–30.9]	30.0 [0.5–30.3]	29.6 [0.8–30.4]	.935
$D_{mean,LAD}$ (Gy/Gy(RBE))	15.2 [0.7–30.4][c,d,e,f]	13.9 [0.7–26.9][d,f]	13.0 [0.7–30.1][a,d,f]	5.6 [0.7–22.7][a,b,c,e]	12.9 [0.1–29.8][a,d]	8.1 [0.1–23.1][a,b,c]	<.001
$D_{2\%,LAD}$ (Gy/Gy(RBE))	28.3 [1.1–30.9]	28.5 [1.2–31.0]	29.9 [1.0–31.2]	22.7 [1.1–31.2]	30.3 [0.4–30.9]	26.6 [0.6–31.2]	.215
$D_{mean,lungs}$ (Gy/Gy(RBE))	8.8 [4.2–18.8][b,c,d,e,f]	7.2 [3.8–15.8][a,d,e,f]	6.7 [4.0–14.2][a,d,e,f]	6.2 [3.6–14.1][a,b,c,f]	5.2 [1.9–13.8][a,b,c,f]	4.5 [1.8–12.2][a,b,c,d,e]	<.001
$V_{20Gy,lungs}$ (%)	21.3 [8.4–57.0][b,c,d,e,f]	16.8 [7.6–44.8][a,c,d,e,f]	10.3 [3.2–29.8][a,b,d,e]	8.9 [3.1–25.5][a,b,c,e,f]	12.7 [3.8–35.8][a,b,c,d,f]	10.9 [3.6–32.8][a,b,d,e]	<.001
$V_{5Gy,lungs}$ (%)	37.1 [16.3–76.1][b,c,e,f]	31.4 [15.1–70.9][a,c,d,e,f]	42.5 [22.7–83.5][a,b,e,f]	39.8 [20.0–91.1][b,e,f]	26.4 [9.7–66.4][a,b,c,d,f]	22.4 [9.1–58.0][a,b,c,d,e]	<.001
$D_{mean,left\ breast}$ (Gy/Gy(RBE))[g]	2.1 [0.3–10.0][e,f]	1.6 [0.5–5.6][e,f]	2.2 [0.5–7.0][e,f]	2.3 [0.5–5.3][e,f]	0.5 [0.0–2.6][a,b,c,d]	0.7 [0.0–2.1][a,b,c,d]	<.001
$D_{mean,right\ breast}$ (Gy/Gy(RBE))[g]	1.9 [0.4–8.5][e,f]	2.3 [0.5–9.9][e,f]	1.4 [0.4–5.3][e,f]	2.1 [0.4–5.1][e,f]	0.3 [0.0–3.0][a,b,c,d]	0.5 [0.0–4.2][a,b,c,d]	<.001
ID (Gy·kg/Gy(RBE)·kg)[h]	80.6 [42.2–217.3][c,e]	85.8 [43.5–211.4][d,f]	79.8 [38.3–189.8][a,e]	84.9 [40.3–180.4][b,f]	42.2 [13.6–119.5][a,c]	44.9 [14.2–118.2][b,d]	<.001
$CI_{Paddick}$	0.40 [0.35–0.58][b,c,d,e,f]	0.39 [0.31–0.59][a,c,d,e,f]	0.88 [0.85–0.90][a,b,e,f]	0.88 [0.84–0.91][a,b,e,f]	0.84 [0.74–0.87][a,b,c,d,f]	0.81 [0.71–0.86][a,b,c,d,e]	<.001

CTV: clinical target volume; PTV: planning target volume; HI: heterogeneity index; LAD: left anterior descending coronary artery; ID: integral dose; $CI_{Paddick}$: Paddick's conformity index.
The data are presented as median value and range, with the results of the Friedman and pairwise Wilcoxon tests.
Statistically significant difference ($p<.05$) for the pairwise comparison of each treatment technique vs. alternatives: [a]vs. FB 3D-CRT, [b]vs. DIBH 3D-CRT, [c]vs. FB VMAT, [d]vs. DIBH VMAT, [e]vs. FB IMPT and [f]vs. DIBH IMPT.
[g]For the 10 female patients, [h]Comparison only within the same breathing technique.

The lowest $V_{20Gy,lungs}$ was observed for VMAT, followed by IMPT and 3D-CRT, and the lowest $V_{5Gy,lungs}$ was observed for IMPT, followed by 3D-CRT and VMAT. All these differences were statistically significant. Hence, compared to 3D-CRT, IMPT reduced the irradiated lung volume for all dose levels, while VMAT reduced the lung volume receiving high doses, however at the cost of increasing the low dose volume (Figure 1(c)).

Heart and LAD

For both DIBH and FB, the lowest median $D_{mean,heart}$ was observed for IMPT, followed by VMAT and 3D-CRT (Figure 2(c)), with all differences being statistically significant. The $D_{mean,heart}$ was reduced by approximately 30–50% and 10–30% for IMPT compared to 3D-CRT and VMAT, respectively. The median $D_{mean,LAD}$ was significantly lower for VMAT and IMPT compared to 3D-CRT, however, no significant difference was observed between VMAT and IMPT. No significant differences in $D_{2\%,heart}$ and $D_{2\%,LAD}$ were observed between any of the treatment techniques.

Breasts

For both DIBH and FB, the median $D_{mean,right\ breast}$ and $D_{mean,left\ breast}$ were significantly reduced by approximately 60–90% for IMPT compared to both VMAT and 3D-CRT, however, no significant difference was observed between VMAT and 3D-CRT (Figure 2(d,e)).

Paddick's conformity index and integral dose

For both DIBH and FB, the highest $CI_{Paddick}$ was observed for VMAT, followed by IMPT and 3D-CRT, with all differences being statistically significant. The ID was approximately halved for IMPT compared to both VMAT and 3D-CRT.

Target coverage

For both DIBH and FB, the $V_{95\%,CTV}$, $V_{95\%,PTV}$ and HI_{PTV} were significantly improved for IMPT and VMAT compared to 3D-CRT (Figure 1(a,b)). The target coverage and HI were similar for VMAT and IMPT, however, for some comparisons there were small but statistically significant differences.

Comparison of FB IMPT and DIBH VMAT

The lowest OAR doses were generally observed for the combination of DIBH and IMPT (Figures 1 and 2). However, this combination may not always be feasible and to compare FB IMPT with DIBH 3D-CRT and VMAT is therefore also of clinical interest. Since DIBH VMAT was generally superior to DIBH 3D-CRT, FB IMPT was compared to DIBH VMAT. There was no significant difference in the median $D_{mean,lungs}$ and $D_{mean,heart}$ between FB IMPT and DIBH VMAT. However, $V_{20Gy,lungs}$ and $D_{mean,LAD}$ were significant lower for DIBH VMAT compared to FB IMPT and vice versa for $V_{5Gy,lungs}$, $D_{mean,right\ breast}$ and $D_{mean,left\ breast}$.

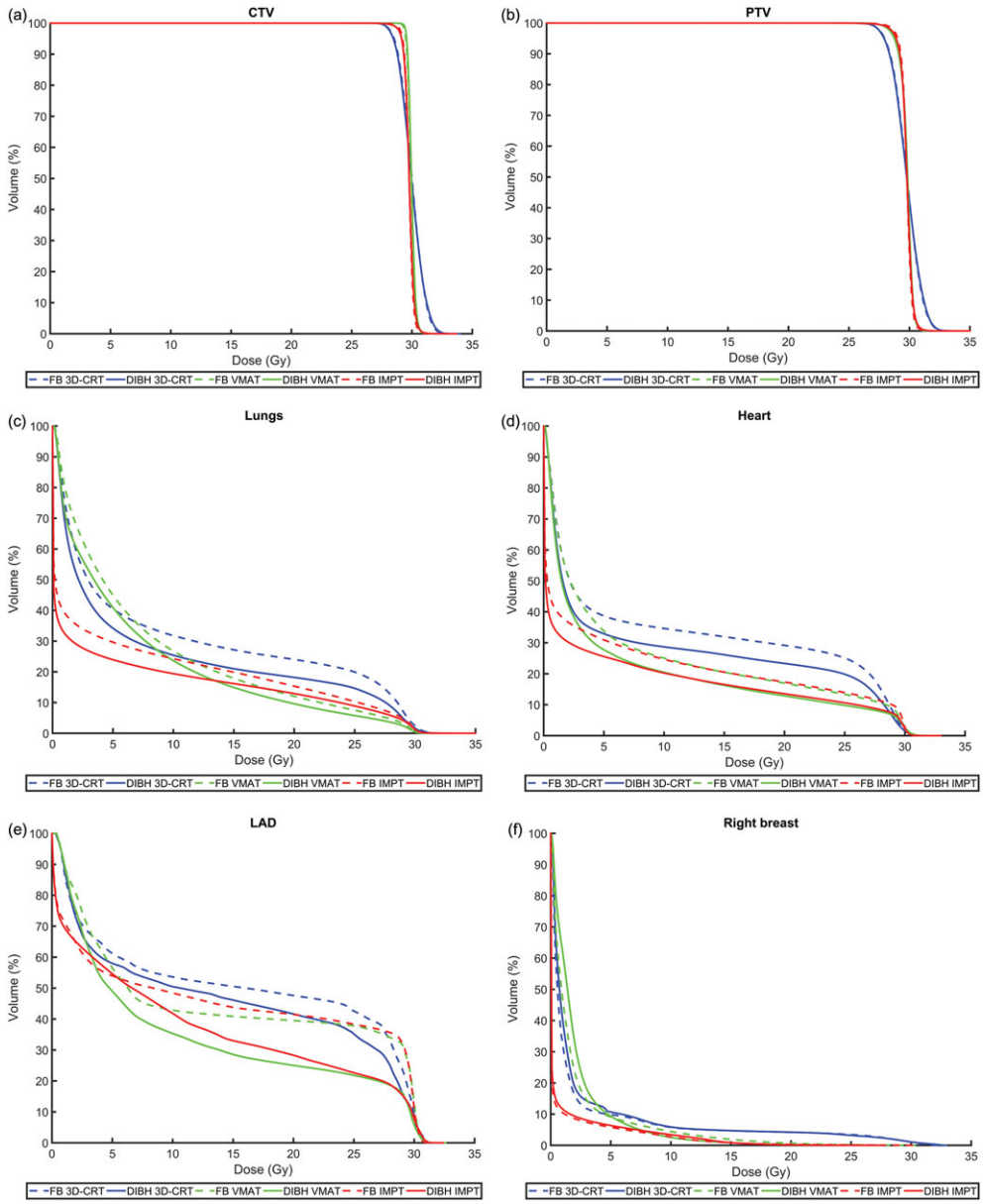

Figure 1. Average dose volume histograms for all patients comparing deep inspiration breath hold (DIBH, solid lines) and free breathing (FB, dashed lines) as well as intensity modulated proton therapy (IMPT, red), volumetric modulated arc therapy (VMAT, green) and 3-dimensional conformal radiation therapy (3D-CRT, blue) for the (a) CTV, (b) PTV, (c) lungs, (d) heart, (e) left anterior descending (LAD) coronary artery, (f) right breast and (g) left breast.

Discussion

Treatment using DIBH is widely assessable in modern RT, and was hereby found to be well tolerated and to reduce doses to OARs for the majority of the patients with mediastinal HL for various treatment techniques. For the vast majority of the patients, the mean lung dose was reduced using DIBH. However, larger variations were observed for the

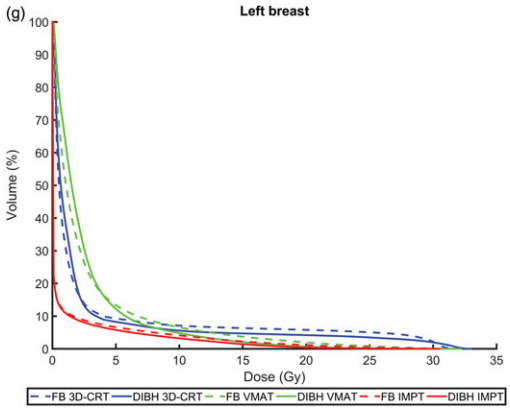

Figure 1. Continued.

mean heart and LAD doses, increasing the dose during DIBH for individual patients (Figure 2(b,c)). Regarding the female breasts, no significant difference was observed between DIBH and FB. For IMPT, a small difference was observed in the target coverage between FB and DIBH, which probably is clinically irrelevant. Thus the DIBH and FB plans could be considered comparable regarding the target coverage.

Both IMPT and VMAT improved the target coverage and resulted in more conform dose distributions compared to 3D-CRT. However, IMPT was more beneficial than VMAT, since it reduced the OAR doses for all dose levels, while VMAT reduced the volumes receiving high doses, however, at the expense of increasing the low-dose volumes. Also, the ID, reflecting the total body radiation exposure, was greatly reduced for all patients using IMPT compared to VMAT and 3D-CRT, potentially leading to a lower risk of secondary malignancies [6]. The lowest doses to the OARs were generally observed for the combination of DIBH and IMPT. For LAD, however, the lowest mean dose was observed for DIBH VMAT. The entire LAD is usually located within the high-dose area, and therefore greatly benefits from the excellent conformity achieved by VMAT while it is not affected by the increased low-dose bath.

The use of DIBH increased the lung volume, which resulted in a smaller proportion of the lung included in the treatment fields. Also, the heart was pulled caudally and the mediastinum elongated, which resulted in an increased separation between the heart and the target volume for most patients. However, this study showed that the desired separation between the heart and target volume was not always achieved with DIBH. For a few of the patients, the overlap between the heart and target volume was instead increased during DIBH, which resulted in higher heart doses. This effect was most pronounced for 3D-CRT, since the dose distribution was less conformed compared to VMAT and IMPT. The anatomical changes during DIBH were highly individual, and for some patients there were none or only a small overlap between the heart and target volume in FB, limiting the possible heart dose reduction for DIBH. For patients with an overlap between the heart and target volume, deformations during DIBH led to more or less advantageous positions with regards to treatment beams. Hence, the impact of DIBH on the heart dose for mediastinal HL is highly individual and cannot be predicted in advance. Therefore, CT images in both FB and DIBH should be acquired for each patient and comparative treatment planning performed. However, large heart and LAD dose reductions were observed using DIBH for individual patients. For example, one of the patients had relative mean heart and LAD dose reductions of approximately 70% and 30–40% using DIBH for all three treatment techniques.

Several studies have compared treatment of mediastinal HL in DIBH and FB for photon therapy, both for 3D-CRT and IMRT [13–16]. The reduced lung dose observed in this study using DIBH confirms the results of the prior studies. However, previous studies have shown a significant decrease in the mean heart dose for DIBH, which was only observed for VMAT in this study, although a decrease was observed for most patients for the other treatment techniques as well. The study by Petersen et al. [14] was the only one that investigated the LAD dose and they showed a significant reduction in the mean LAD dose using DIBH, which was only observed for VMAT in this study. Possible reasons for the difference in heart and LAD doses could be that smaller treatment margins were used for DIBH compared to FB in some of the studies, different target localization in mediastinum and that different photon treatment delivery techniques (3D-CRT/IMRT/VMAT) were used. In accordance with our study, Petersen et al. [14] and Aznar et al. [16] did not find any significant difference in the mean breast dose between DIBH and FB. Charpentier et al. [15], however, reported a significant increase in the mean breast dose for DIBH compared to FB.

Regarding the use of PT, most previous studies for mediastinal HL have investigated the impact on normal tissue dose using the passive scattering technique in FB. In accordance to this study, they showed that the dose to the lungs, heart and breasts was generally reduced for proton compared to photon therapy [6,17–19]. However, in this study, the more advanced delivery technique PBS, which enables even larger normal tissue sparing, has been used. In a review article, Tseng et al. [6] present a weighted average OAR dose comparison of 14 studies between PT (passive scattering and PBS), modern RT (IMRT, VMAT and tomotherapy) and 3D-CRT during FB. The $D_{mean,heart}$, $D_{mean,breasts}$ and $D_{mean,lungs}$ were reduced by 3.57 Gy, 1.47 Gy and 2.81 Gy for PT compared to 3D-CRT, which is comparable to the dose reductions observed in this study. Comparing PT with modern RT, the corresponding dose reductions were 2.24 Gy, 2.45 Gy and 3.28 Gy, which are slightly larger than the dose reductions observed in this study. Tseng et al. concluded that a larger dose reduction could be achieved for PT compared to modern RT than for modern RT compared to 3D-CRT for all OARs. In this study, however, a larger benefit of using modern RT (VMAT) compared to 3D-CRT was observed, thus reducing the differences between PT (IMPT) and modern RT (VMAT).

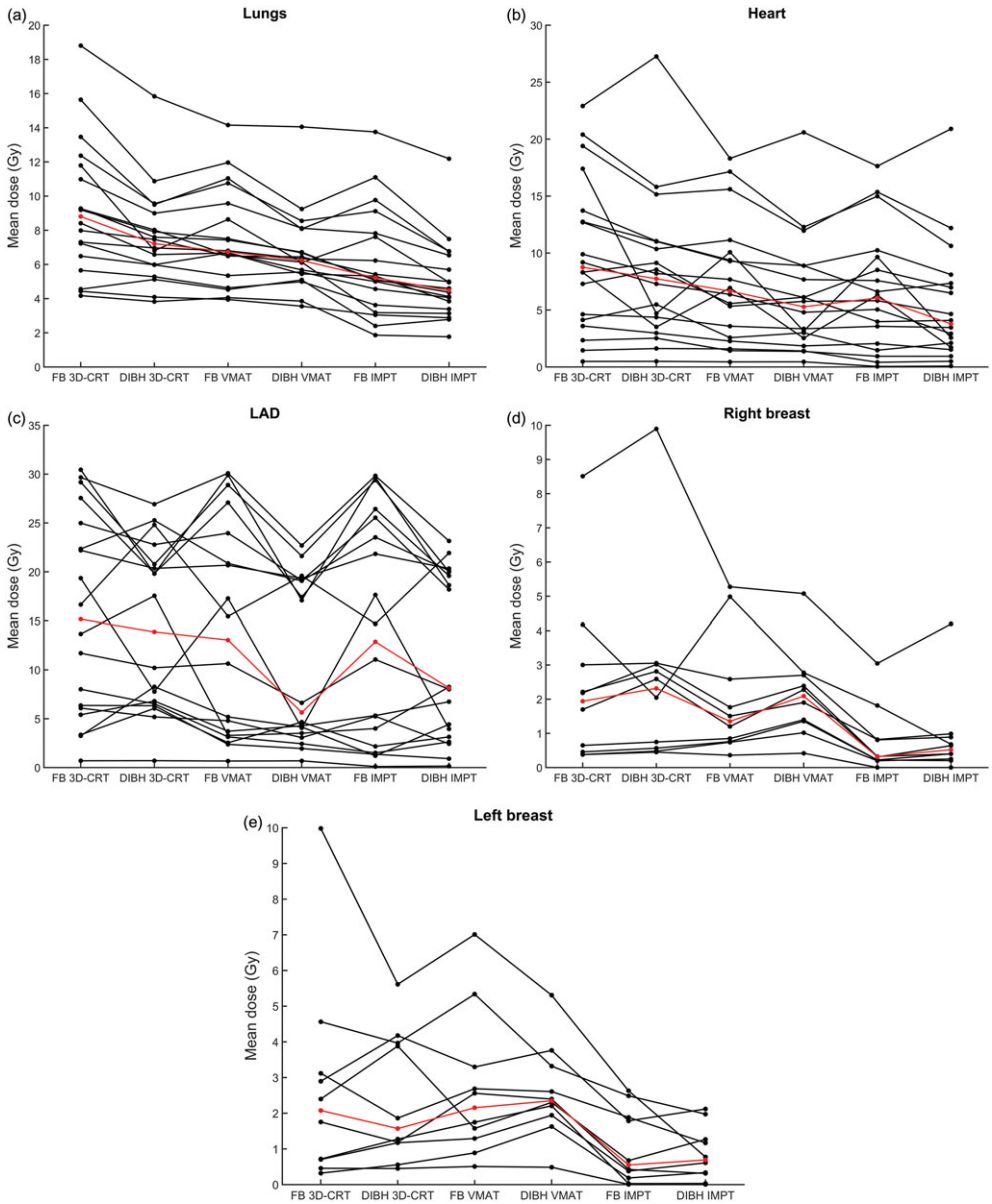

Figure 2. The mean dose to the (a) lungs, (b) heart, (c) LAD, (d) right breast and (e) left breast for free breathing (FB) 3-dimensional conformal radiation therapy (3D-CRT), deep inspiration breath hold (DIBH) 3D-CRT, FB volumetric modulated arc therapy (VMAT), DIBH VMAT, FB intensity modulated proton therapy (IMPT) and DIBH IMPT. The values for each individual patient are shown in black and the median values for the whole patient cohort in red.

However, a clear disadvantage of VMAT is the increased low-dose bath.

To our knowledge, only two previous studies have investigated the combined use of DIBH and PT for mediastinal HL [21,22]. However, no previous study as comprehensive as this exists, comparing DIBH and FB for IMPT, VMAT and 3D-CRT for the same patient cohort. Rechner et al. [22] compared PT and IMRT for both DIBH and FB. Both this study and Rechner et al. showed the lowest OAR doses for the combined use of DIBH and PT. In contrary to what was observed in this study, they

showed a significant reduction in the mean heart and LAD doses and no significant difference in the mean lung dose, comparing DIBH and FB for PT. Also, they found no significant difference in the heart and lung mean dose between DIBH photon therapy and FB PT. In this study, however, significant differences in favor of FB IMPT were found compared to DIBH 3D-CRT, but not compared to DIBH VMAT. Generally, a larger benefit on normal tissue dose for proton compared to photon therapy was observed in this study, whereas, Rechner et al. found a larger benefit of DIBH compared to FB. Possible reasons for the differences observed between the studies could be different target localization in mediastinum, the use of different treatment techniques (single field uniform dose/IMPT and 3D-CRT/IMRT/VMAT) and that smaller margins were used in the superior–inferior direction for DIBH by Rechner et al., whereas, in this study the same margins for FB and DIBH were used.

Baues et al. [21] is the only previous study that has compared IMPT and VMAT during DIBH for mediastinal HL, however, they did not make a comparison between DIBH and FB. They showed reduced mean doses of 38–83% for the lungs, heart and breasts using IMPT compared to VMAT, comparable to the reductions of 27–76% observed in this study. Also, they showed a 49% decrease in the mean dose to healthy tissue, corresponding to the 47% decrease in ID observed in this study. However, they showed a 32% reduction in $V_{20Gy,lungs}$ for IMPT compared to VMAT, whereas a 22% increase was observed in this study.

PET images during DIBH, shown feasible by Petersen et al. [14], were not available in this study. However, to reduce contouring uncertainties, target delineation was performed by the same oncologist and carefully investigated for each patient during FB and DIBH. In order to make a strict comparison between all different treatment techniques, the same CTV-PTV margins were used for FB and DIBH. Also, essentially the same PTV volumes were used for the IMPT plans, with only a small (1 mm) additional margin for range uncertainties added for a few patients. Thus, the dose reductions observed for DIBH were derived only by anatomical changes and not reduced CTV-PTV margins.

A limitation of this study is that intrafractional motion during treatment has not been considered, which has the largest dosimetric effects for IMPT, followed by VMAT and 3D-CRT. Intrafractional motion in combination with VMAT and PBS delivery can lead to unwanted dosimetric interplay effects, resulting in a degradation of the dose distribution to the target and/or OARs [27,28]. For PT, range uncertainties may also negatively impact the dose distribution [27]. However, this was a pure treatment planning study, guiding to what is possible regarding dose sparing to OARs using different treatment techniques, and thus, the plans were not created with regards to robust treatment delivery. Robust optimization could have been used [29,30], however, this technique was not available during the execution of this study. However, robust PBS plans have been shown feasible for mediastinal lymphomas, with minimal impact of interplay effect if repainting and/or larger spot size is used [31]. Further, reduced margins due to mitigation of the target motion during DIBH were not considered in this study. However, the treatment is delivered during several DIBHs, raising concerns about uncertainties in the intrafractional DIBH target position reproducibility [32]. Another limitation is that a constant RBE value of 1.1 was assumed for the IMPT plans according to ICRU recommendations [33], however in reality the RBE increases toward the distal edge of the SOBP [34]. In the case of mediastinal HL, this could potentially increase the biological effective dose to the OARs since they are situated beyond the SOBP and this would depend on the field setting used.

In addition, this study focuses on dosimetric effects, and it is hard to estimate the exact clinical benefit for each individual from the dose distributions obtained for the different treatment techniques. However, as low doses as possible to OARs are always preferable in order to reduce side effects. Especially in these often young patients, with a long life-expectancy, who also receive chemotherapy which may increase risk of cardiac-/lung toxicity as well as secondary malignancies.

Conclusions

The majority of patients in this study benefited from DIBH, however, the impact on the normal tissue dose was highly individual and therefore comparative treatment planning between DIBH and FB is encouraged. The largest benefits were generally observed for the combination of DIBH and IMPT. However, since multiple OARs are considered simultaneously and there is a large variation in disease distribution, there is not a single best treatment technique for all mediastinal HL patients, and the treatment technique should be chosen individually for each patient.

Disclosure statement

No potential conflict of interest was reported by the authors.

References

[1] Eich HT, Diehl V, Gorgen H, et al. Intensified chemotherapy and dose-reduced involved-field radiotherapy in patients with early unfavorable Hodgkin's lymphoma: final analysis of the German Hodgkin Study Group HD11 trial. JCO. 2010;28:4199–4206.

[2] Engert A, Plütschow A, Eich HT, et al. Reduced treatment intensity in patients with early-stage Hodgkin's lymphoma. N Engl J Med. 2010;363:640–652.

[3] Aleman BM, van den Belt-Dusebout AW, Klokman WJ, et al. Long-term cause-specific mortality of patients treated for Hodgkin's disease. J Clin Oncol. 2003;21:3431–3439.

[4] Castellino SM, Geiger AM, Mertens AC, et al. Morbidity and mortality in long-term survivors of Hodgkin lymphoma: a report from the Childhood Cancer Survivor Study. Blood. 2011;117:1806–1816.

[5] Ng A, Bernardo M, Weller E, et al. Long-term survival and competing causes of death in patients with early-stage Hodgkin's disease treated at age 50 or younger. J Clin Oncol. 2002;20:2101–2108.

[6] Tseng YD, Cutter DJ, Plastaras JP, et al. Evidence-based review on the use of proton therapy in lymphoma from the Particle Therapy Cooperative Group (PTCOG) lymphoma subcommittee. Int J Radiat Oncol Biol Phys. 2017;99:825–842.

[7] Maraldo MV, Specht L. A decade of comparative dose planning studies for early-stage Hodgkin lymphoma: what can we learn? Int J Radiat Oncol Biol Phys. 2014;90:1126–1135.
[8] Specht L, Yahalom J, Illidge T, et al. Modern radiation therapy for Hodgkin lymphoma: field and dose guidelines from the international lymphoma radiation oncology group (ILROG). Int J Radiat Oncol Biol Phys. 2014;89:854–862.
[9] Voong KR, McSpadden K, Pinnix CC, et al. Dosimetric advantages of a "butterfly" technique for intensity-modulated radiation therapy for young female patients with mediastinal Hodgkin's lymphoma. Radiat Oncol. 2014;9:94.
[10] Lohr F, Georg D, Cozzi L, et al. Novel radiotherapy techniques for involved-field and involved-node treatment of mediastinal Hodgkin lymphoma: when should they be considered and which questions remain open? Strahlenther Onkol. 2014;190:864–871.
[11] Fiandra C, Filippi AR, Catuzzo P, et al. Different IMRT solutions vs. 3D-conformal radiotherapy in early stage Hodgkin's lymphoma: dosimetric comparison and clinical considerations. Radiat Oncol. 2012;7:186.
[12] Stromberg JS, Sharpe MB, Kim LH, et al. Active breathing control (ABC) for Hodgkin's disease: reduction in normal tissue irradiation with deep inspiration and implications for treatment. Int J Radiat Oncol Biol Phys. 2000;48:797–806.
[13] Paumier A, Ghalibafian M, Gilmore J, et al. Dosimetric benefits of intensity-modulated radiotherapy combined with the deep-inspiration breath-hold technique in patients with mediastinal Hodgkin's lymphoma. Int J Radiat Oncol Biol Phys. 2012;82:1522–1527.
[14] Petersen PM, Aznar MC, Berthelsen AK, et al. Prospective phase II trial of image-guided radiotherapy in Hodgkin lymphoma: benefit of deep inspiration breath-hold. Acta Oncol. 2015;54:60–66.
[15] Charpentier AM, Conrad T, Sykes J, et al. Active breathing control for patients receiving mediastinal radiation therapy for lymphoma: impact on normal tissue dose. Pract Radiat Oncol. 2014;4:174–180.
[16] Aznar MC, Maraldo MV, Schut DA, et al. Minimizing late effects for patients with mediastinal Hodgkin lymphoma: deep inspiration breath-hold, IMRT, or both? Int J Radiat Oncol Biol Phys. 2015;92:169–174.
[17] Hoppe BS, Flampouri S, Zaiden R, et al. Involved-node proton therapy in combined modality therapy for Hodgkin lymphoma: results of a phase 2 study. Int J Radiat Oncol Biol Phys. 2014;89:1053–1059.
[18] Chera BS, Rodriguez C, Morris CG, et al. Dosimetric comparison of three different involved nodal irradiation techniques for stage II Hodgkin's lymphoma patients: conventional radiotherapy, intensity-modulated radiotherapy, and three-dimensional proton radiotherapy. Int J Radiat Oncol Biol Phys. 2009;75:1173–1180.
[19] Li J, Dabaja B, Reed V, et al. Rationale for and preliminary results of proton beam therapy for mediastinal lymphoma. Int J Radiat Oncol Biol Phys. 2011;81:167–174.
[20] Enmark M, Lundkvist N, Fager M, et al. PTC17-0493: Clinical Commissioning of Gated Proton Pencil Beam Scanning. Additional Proceedings to the 56th Annual Meeting of the Particle Therapy Cooperative Group (PTCOG). Int J Part Ther. 2017;4:39.
[21] Baues C, Marnitz S, Engert A, et al. Proton versus photon deep inspiration breath hold technique in patients with Hodgkin lymphoma and mediastinal radiation: a planning comparison of deep inspiration breath hold intensity modulation radiotherapy and intensity modulated proton therapy. Radiat Oncol. 2018;13:122.
[22] Rechner LA, Maraldo MV, Vogelius IR, et al. Life years lost attributable to late effects after radiotherapy for early stage Hodgkin lymphoma: the impact of proton therapy and/or deep inspiration breath hold. Radiother Oncol. 2017;125:41–47.
[23] Edvardsson A, Nilsson MP, Amptoulach S, et al. Comparison of doses and NTCP to risk organs with enhanced inspiration gating and free breathing for left-sided breast cancer radiotherapy using the AAA algorithm. Radiat Oncol. 2015;10:84.
[24] Kugele M, Edvardsson A, Berg L, et al. Dosimetric effects of intrafractional isocenter variation during deep inspiration breath-hold for breast cancer patients using surface-guided radiotherapy. J Appl Clin Med Phys. 2018;19:25–38.
[25] Flejmer AM, Edvardsson A, Dohlmar F, et al. Respiratory gating for proton beam scanning versus photon 3D-CRT for breast cancer radiotherapy. Acta Oncol. 2016;55:577–583.
[26] Paddick I. A simple scoring ratio to index the conformity of radiosurgical treatment plans. Technical note. J Neurosurg. 2000;93 Suppl.3: 219–222.
[27] Bert C, Durante M. Motion in radiotherapy: particle therapy. Phys Med Biol. 2011;56:R113–R144.
[28] Edvardsson A, Nordstrom F, Ceberg C, et al. Motion induced interplay effects for VMAT radiotherapy. Phys Med Biol. 2018;63:085012.
[29] Liu W, Zhang X, Li Y, et al. Robust optimization of intensity modulated proton therapy. Med Phys. 2012;39:1079–1091.
[30] Li Y, Niemela P, Liao L, et al. Selective robust optimization: a new intensity-modulated proton therapy optimization strategy. Med Phys. 2015;42:4840–4847.
[31] Zeng C, Plastaras JP, Tochner ZA, et al. Proton pencil beam scanning for mediastinal lymphoma: the impact of interplay between target motion and beam scanning. Phys Med Biol. 2015;60:3013–3029.
[32] Enmark M, Olofsson J, Ceberg S, Jonsson J. [P205] The impact on pencil beam scanning (PBS) proton therapy for mediastinal lymphoma from deep inspiation breath-hold (DIBH) variability. Phys Med. 2018;52:159.
[33] Prescribing, Recording, and Reporting Proton-beam Therapy. ICRU Report 78 2007.
[34] Paganetti H. Relative biological effectiveness (RBE) values for proton beam therapy. Variations as a function of biological endpoint, dose, and linear energy transfer. Phys Med Biol. 2014;59:R419–R472.

Paper IV

Check for updates

Received: 15 February 2019 | Revised: 13 June 2019 | Accepted: 26 July 2019

DOI: 10.1002/acm2.12700

RADIATION ONCOLOGY PHYSICS

WILEY

Surface guided radiotherapy (SGRT) improves breast cancer patient setup accuracy

Malin Kügele[1,2] | Annika Mannerberg[2] | Susanne Nørring Bekke[3] | Sara Alkner[1,4] | Lovisa Berg[1] | Faisal Mahmood[5] | Charlotte Thornberg[1] | Anneli Edvardsson[1] | Sven Å. J. Bäck[1] | Claus F. Behrens[3] | Sofie Ceberg[1,2]

[1]Department of Hematology, Oncology and Radiation Physics, Skåne University Hospital, Lund, Sweden

[2]Medical Radiation Physics, Department of Clinical Sciences, Lund University, Lund, Sweden

[3]Radiotherapy Research Unit, Department of Oncology, Herlev Hospital, University of Copenhagen, Copenhagen, Denmark

[4]Department of Clinical Sciences, Division of Oncology and Pathology, Lund University, Lund, Sweden

[5]Department of Oncology, Odense University Hospital, Odense C, Denmark

Author to whom correspondence should be addressed. Sofie Ceberg
E-mail: sofie.ceberg@med.lu.se.

Funding information
C-RAD AB

Abstract

Purpose: The purpose of the study was to investigate if surface guided radiotherapy (SGRT) can decrease setup deviations for tangential and locoregional breast cancer patients compared to conventional laser-based setup (LBS).

Materials and Methods: Both tangential (63 patients) and locoregional (76 patients) breast cancer patients were enrolled in this study. For LBS, the patients were positioned by aligning skin markers to the room lasers. For the surface based setup (SBS), an optical surface scanning system was used for daily setup using both single and three camera systems. To compare the two setup methods, the patient position was evaluated using verification imaging (field images or orthogonal images).

Results: For both tangential and locoregional treatments, SBS decreased the setup deviation significantly compared to LBS ($P < 0.01$). For patients receiving tangential treatment, 95% of the treatment sessions were within the clinical tolerance of ≤ 4 mm in any direction (lateral, longitudinal or vertical) using SBS, compared to 84% for LBS. Corresponding values for patients receiving locoregional treatment were 70% and 54% for SBS and LBS, respectively. No significant difference was observed comparing the setup result using a single camera system or a three camera system.

Conclusions: Conventional laser-based setup can with advantage be replaced by surface based setup. Daily SGRT improves patient setup without additional imaging dose to breast cancer patients regardless if a single or three camera system was used.

KEY WORDS
interfraction motion, optical surface scanning, patient positioning, surface guided radiotherapy

1 | INTRODUCTION

Breast conserving surgery can remove macroscopic disease for early stage breast cancer.[1] After surgery some microscopic tumor foci may remain, and if not treated with radiotherapy this can lead to locoregional recurrence and/or life-threatening distant metastases.[1] Early Breast Cancer Trialists' Group performed a meta-analysis of individual data for 10 801 women from 17 randomized trials and showed that the 10-yr risk for any first recurrence was 35% for women allocated to breast conserving surgery only, and 19% for women allocated to breast conserving surgery and radiotherapy.[1] The absolute risk reduction was 16%. For every four recurrence avoided by

This is an open access article under the terms of the Creative Commons Attribution License, which permits use, distribution and reproduction in any medium, provided the original work is properly cited.
© 2019 The Authors. *Journal of Applied Clinical Medical Physics* published by Wiley Periodicals, Inc. on behalf of American Association of Physicists in Medicine.

radiotherapy, one breast cancer death can be avoided.[1] There is no effective method to find microscopic disease after breast conserving surgery and therefor radiotherapy is still considered to be important for the cure of breast cancer. Radiotherapy for breast cancer treatment uses a three-dimensional computed tomography (3DCT)-based treatment planning which enables a high local selectivity for the dose distribution; the target tissue is irradiated while the normal tissue is spared. The treatment planning system (TPS) ensures a high accuracy in the dose deposition which requires high accuracy in daily patient setup. Breast cancer patients have a long expected survival and it is of importance to reduce interfractional setup errors to avoid excessive irradiation that can cause toxicity in normal healthy tissue. The organs at risk (OAR) are primarily the lung and the heart. Hence, complications such as radiation pneumonitis and cardiac mortality have been shown to positively correlate with the volume irradiated.[2,3] Setup verification imaging strategies, generally classified as either online or offline, are used to ensure that systematic and randomized setup deviations are minimized throughout treatment. The drawback is that both strategies are associated with a risk for second malignancies due to imaging dose.[4] The online strategy implies daily imaging before treatment with a preset threshold for deviations. Laaksomaa et al., recommended daily online image guidance due to large random interfractional variation in patient posture.[5] This strategy is time-consuming and contributes imaging dose to the patient throughout treatment. Having in mind the increased radiation dose due to imaging, the ALARA principle and the fact that the survival of breast cancer patients is expected to be long, an accurate nondose-contributing setup system is warranted. The offline strategy requires frequent imaging in the beginning of the treatment course. The result is statistically analyzed for the systematic and random components of the deviation in the patient position. The systematic deviation is compensated for by a couch shift for the following treatment sessions.[6] The random deviation is mainly due to the inaccuracy in laser aligned setup, which is commonly used for daily setup. The patients are aligned according to landmarks on the skin and room lasers.[6] An alternative approach is to use surface guided radiotherapy (SGRT), which uses a three-dimensional (3D) model of the skin surface for positioning and monitoring. The optical surface scanning (OSS) system compares a 3D model of the patient's external surface extracted from the TPS with a live scan of the surface while the patient is positioned on the treatment couch (Fig. 1). Surface based setup (SBS) increases the patient setup information compared to laser-based setup (LBS), by using the entire patient skin surface instead of only three skin marks. Several OSS systems have shown a high correlation with verification imaging results.[7–9] Also, Chang et al. have in a study with 23 patients shown that SGRT has a high correlation to the lumpectomy cavity defined by surgical clips for breast cancer patients receiving accelerated partial breast irradiation.[10] The OSS system Catalyst™ (C-rad Positioning AB, Uppsala, Sweden) has been evaluated in this study. This OSS system is unique because it uses a deformable algorithm to calculate the isocenter position. The principle behind the deformable registration in depth scans is described by Hao Li et al.[11] Recently published results showed that patient setup using the deformable algorithm of the Catalyst™ system was superior to LBS for breasts with nodal involvement in TomoTherapy (Accuray, Sunnyvale, CA).[12] The work carried out by Crop et al. used mass-weighted PTV location for patient setup, specially designed for the TomoTherapy environment. Similar results were observed at a linear accelerator by Stanley et al. using the Catalyst™ for breast cancer patient positioning.[13] However, comparison between tangential and locoregional treatments and single *vs.* three camera systems has to our knowledge not been investigated.

Tangential and locoregional treatments, and also, single and three camera systems result in different surface coverage which motivates an investigation of how the setup accuracy is affected. The aim of this study was to retrospectively compare LBS with SBS using the OSS system Catalyst™ for both tangential and locoregional breast cancer patients using single and three camera systems.

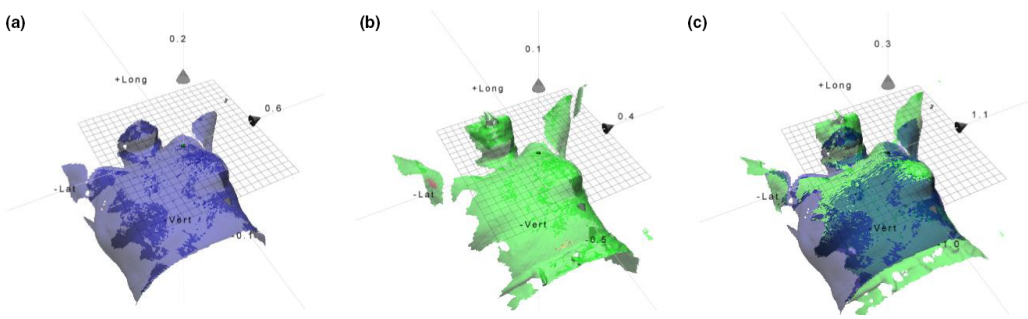

FIG. 1. (a) Reference surface (blue color) with the planned isocenter from the treatment planning system. (b) The live patient surface (green color) captured by a single camera Catalyst™ system. (c) The reference and live surface are matched with a deformable algorithm and a couch shift in 6° of freedom is calculated to shift the live surface into the correct position with respect to the isocenter.

2 | MATERIALS AND METHODS

2.A | Ethical consideration and consent

The use of the radiotherapy database for retrospective research has been approved by the Regional Ethical Review Board in Lund (No. 2013/742).

2.B | Patient selection

A total of 139 patients were enrolled in this study, 63 patients received tangential treatment after breast conserving surgery and 76 with locally advanced breast cancer patients received locoregional treatment after mastectomy or breast conserving surgery. Both left- and right-sided breast cancers were included, however, patients treated in deep inspiration breath hold were excluded in this study. The median age was 62 yr (range: 34–83 yr) and 64 yr (range: 33–87 yr) for the breast cancer patients receiving tangential and locoregional treatment, respectively.

2.C | Computed tomography and patient immobilization

All patients underwent CT using a Siemens Somatom definition AS plus (Siemens Medical Solutions, Erlangen, Germany) for treatment planning. In the TPS (Eclipse version 10.0.28 and 13.6.23, Varian medical systems; CA Varian), the surface structure set (BODY), treatment fields and isocenter position were exported to the Catalyst™ in the industry standard DICOM format. The patients were treated in supine position on a breast board (Posiboard™-2 Breastboard, CIVCO Medical Solutions) with their arms raised over the head and positioned on an arm support. For tangential and locoregional treatment, a breastboard pitch of 7.5° and 0° was used as standard, respectively. An immobilization wedge was placed under the patients' knees for support. One patient receiving locoregional treatment was positioned in a WingStep™ (Elekta AB, Stockholm, Sweden) and body vacuum bag with the contralateral arm by the side of her body.

2.D | Treatment plans

The treatment prescription was 50 Gy in 25 fractions or 42.6 Gy in 15 fractions, normalized to the PTV mean or median dose. In the TPS 3D conformal treatment plans were created for all patients. For the tangential treatments, two opposing 6 MV tangential fields to cover the breast tissue was used. Also, a supplementary field and/or wedges were used for dose homogenization purposes. The isocenter position was placed central in the breast tissue. For the locoregional treatments, opposing tangential fields were used to cover the location of the breast tissue. To complement the tangential fields in order to achieve homogeneous dose a various number of supplementary fields of 6 or 10 MV were used. The number of fields used depended on target size and patient anatomy. The locoregional axillary lymph nodes were covered with a 6 MV anterior-posterior (AP) field and a 10 MV posterior-anterior (PA) field. Also, a supplementary 10 MV PA field was used while shielding of the lung tissue. The total number of fields used for the locoregional treatments ranged between six and nine. For mastectomy patients, a 0.5-cm thick and 6-cm wide bolus (Superflab, Mick Radio-Nuclear Instruments, Inc. An Eckert & Ziegler BEBIG Company) was placed over the operation scar. For locoregional treatment, the treatment isocenter was positioned in the junction between the tangential and AP-PA fields.

2.E | Surface guided radiotherapy with a deformable algorithm for isocenter calculation

The OSS systems were ceiling-mounted in nine treatment rooms, as either a single camera or a three camera configuration. The three camera configuration provides a 360° surface coverage of the patient, due to a 120° installation angle between the systems. For the single camera configuration, only one system is scanning the patient, thus, the surface coverage becomes degraded. OSS systems at six Varian TrueBeam (Varian Medical Systems, Palo Alto, USA) and three ELEKTA Synergy (Elekta AB, Stockholm, Sweden) equipped with verification imaging systems were used. The single camera Catalyst™ configuration was used for setup of all the tangential treatments. For locoregional treatments, both the single and three camera Catalyst™ configuration were used for patient setup.

The Catalyst™ system consists of a high-power LED projector, which projects a near-visible violet light (λ = 405 nm) for surface reconstruction purposes and a green (λ = 528 nm) and red (λ = 624 nm) projection light for live feedback of the patient posture.[14] The near-visible violet light is projected as sequenced lines onto the object to be scanned. The irregularity of the object scanned disperses the sequenced lines, which is detected by a charged-coupled device (CCD) camera. Due to fixed geometry between the projector and the CCD, the principle of optical triangulation can be used to reconstruct a 3D surface of the object scanned.[15] Patient setup with the Catalyst™ was carried out in two steps; (a) patient posture correction using surface matching and (b) isocenter position adjustment using a deformable algorithm. To correct for patient posture, the OSS system matches the reference surface with the live surface within a determined scanning volume and creates a distance map between the two surfaces. If the two surfaces differ from a preset surface tolerance, the system creates a color map that is back-projected onto the patient's skin. The therapists manually correct the patient posture, and the color map turns transparent once the two surfaces are within the surface tolerance. Based on how well the reference and live surface match the system carries out a depth calculation of the isocenter position using a deformable algorithm (Fig. 1).[16] Thus, the calculated isocenter shift depends on the daily patient setup. For the isocenter calculation, the full patient surface coverage of the thorax was used, however, surface close to isocenter is weighted higher in the calculation than distant surface. Also, anatomical deformations that can occur during the course of radiotherapy were automatically handled by the algorithm. For each

patient, the scanning parameters were adjusted individually in the Catalyst™ software to obtain optimal image quality, minimize camera shadowing, and over or under exposed images.

2.F | Patient setup protocol

At the treatment machine, all patients were initially positioned by laser alignment to a 3-point based tattoo setup.

For the patients positioned using LBS, the calculated shift from the reference point to the isocenter position was manually carried out the first treatment session and the isocenter position was drawn onto the patient's skin using a marker pen. Verification images were acquired, according to a No Action Level (NAL) offline strategy.[17] The systematic deviation was estimated after the first three treatment sessions and the setup was corrected for the remaining treatment sessions. To carry out a fair comparison between the LBS and SBS setup strategy, the setup data from the three first treatment session for the patients positioned using LBS were excluded.

For the patients positioned using SBS, the couch was shifted to the treatment position and the correction for posture was performed using the color map with a tolerance of 5 mm (Fig. 2). The effect of the free breathing motion was minimized by using a floating mean value calculation over 4 s for the live image. Once the posture was within the surface tolerance, the therapists manually shifted the couch to correct for the isocenter deviation. The patient setup result was saved by the therapists inside the treatment room and a residual isocenter deviation ≤2 mm, and rotations ≤ 3° were accepted in this study.

For both the tangential and locoregional treatments, each patient was positioned using either SBS or LBS and the position was verified using onboard imaging at the linac. Different patient anatomies were included for all four groups. The shifts in lateral (lat), longitudinal (lng) and vertical (vrt) direction, respectively, and the total vector offset ($v = \sqrt{lat^2 + lng^2 + vrt^2}$), were evaluated. For SBS, the variation in patient anatomies caused more or less camera shadowing in the live image (Fig. 3).

2.F.1 | Tangential treatment

A total of 63 patients, 26 patients with LBS and 37 patients with SBS, were positioned using a single camera system. The two different setup techniques were verified with field images to enable comparison of the breast position in the treatment field. The anatomical landmarks used were the lung edge and the breast tissue. In total, 677 field images were evaluated. For comparison, a two-sided Wilcoxon sum rank test was carried out for the vector offset and

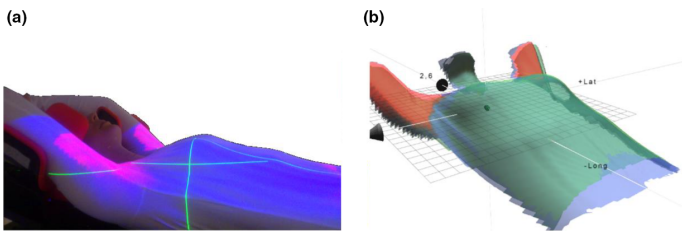

FIG. 2. (a) Color map projected onto the patient's skin for live visual guidance of posture errors in the patient setup. (b) The color map is also shown in the software inside the treatment and control room.

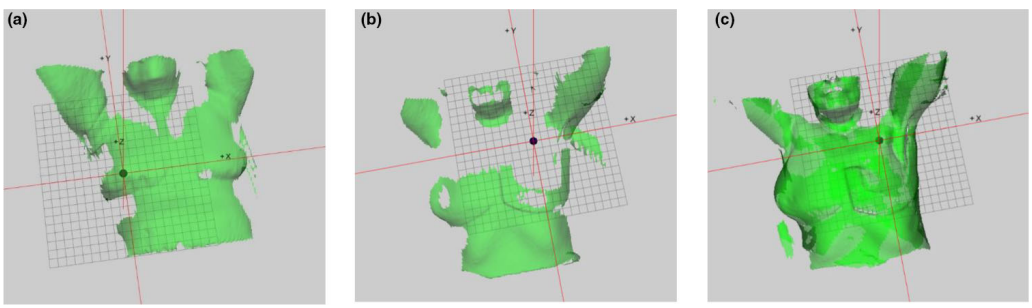

FIG. 3. (a) Surface of a patient receiving tangential breast cancer treatment, positioned with a single camera system. The breast board pitch of 7.5° enhances the patient surface coverage. The isocenter is located in the breast tissue. (b) Surface of a patient receiving locoregional breast cancer treatment at a single camera Catalyst™ system. Nonoptimal camera settings in combination with a 0° pitch of the breast board cause shadowing and the bolus occludes the signal. The loss of patient surface is above the isocenter. (c) Surface of a patient receiving locoregional breast cancer treatment at a three camera Catalyst™ system, with optimal camera settings. Full surface coverage of the patient, including the bolus, is observed.

Students *t*-test for two independent mean for the lat, lng, and vrt directions, with a statistical level of significance α = 0.01.

2.F.2 | Locoregional treatment

Three patient groups of totally 76 patients were enrolled in this study. For SBS, 43 patients were included; 22 patients positioned using a three camera system and 21 patients positioned using a single camera system. Nineteen of the patients had bolus over the operation scar, and one patient had a 1-cm thick wet towel as a bolus. One patient was excluded due to that the OSS system was not used according to the study protocol. In the LBS group, 34 patients were enrolled. The patient setup was verified with orthogonal kilovolt (kV) or megavolt (MV) images. The anatomical landmarks used were the clavicular bone position, the lung edge, and sternum. In total, 632 verification images were evaluated. For comparison a two-sided Wilcoxon sum rank test was carried out for the vector offset and Students t-test for two independent mean for the translational directions with a statistical level of significance α = 0.01.

A two-sided Wilcoxon sum rank test was carried out to investigate if there were any statistical significant difference between the single and three camera system with a significance level of 0.01.

3 | RESULTS

3.A | Tangential treatment

The median vector offset was 4.2 mm (range: 0–19.7 mm) for LBS and 2.4 mm (range: 0–8.1 mm) for SBS verified with field imaging ($P < 0.01$). For LBS and SBS, 84% and 95% of the treatment sessions were within the clinical tolerance of ≤4 mm in all the three directions (lat, lng, or vrt). The cumulative probability for positioning a patient within a spatial vector of 5.0 mm from isocenter was 57% for LBS and 89% for SBS (Fig. 4). For 90% of the setup cases, the

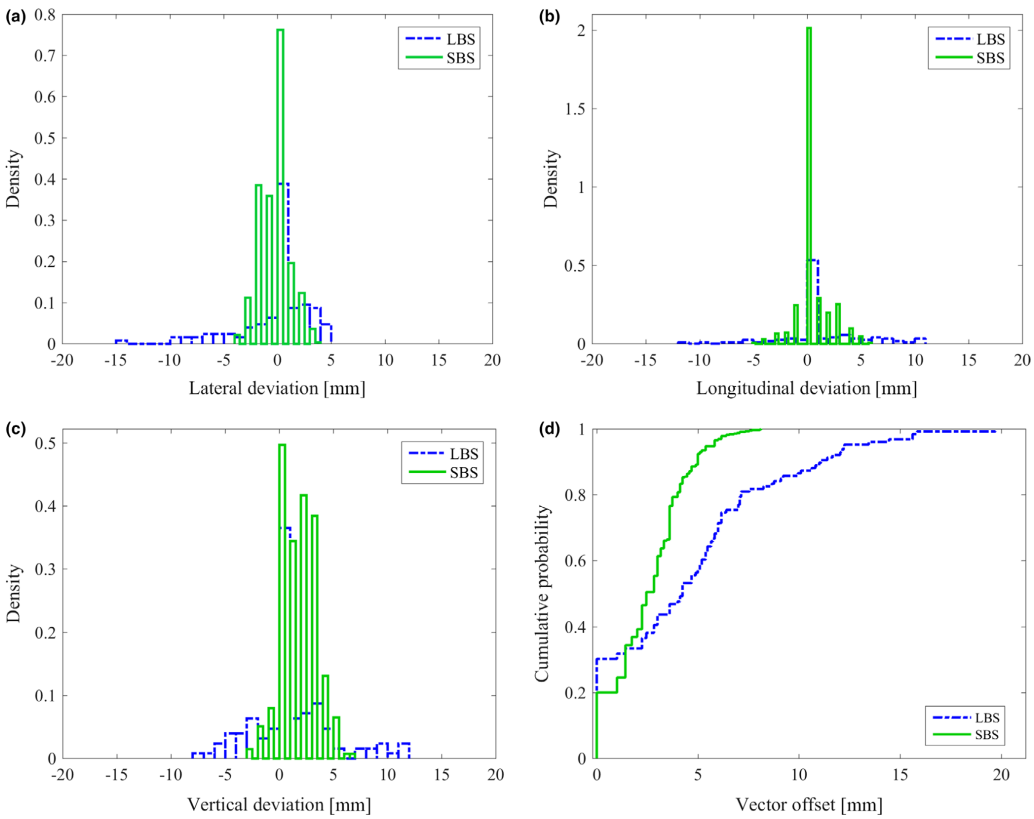

FIG. 4. Setup deviation for breast cancer patients receiving tangential treatment positioned using laser-based setup (LBS) and surface based setup (SBS). Histograms of the setup accuracy in (a) lateral, (b) longitudinal, and (c) vertical direction verified with field imaging. Reduced maximal deviations can be observed for SBS compared to LBS in all three translational directions. (d) The cumulative probability of the vector offset show a significantly improved patient setup for SBS compared to LBS ($P < 0.01$).

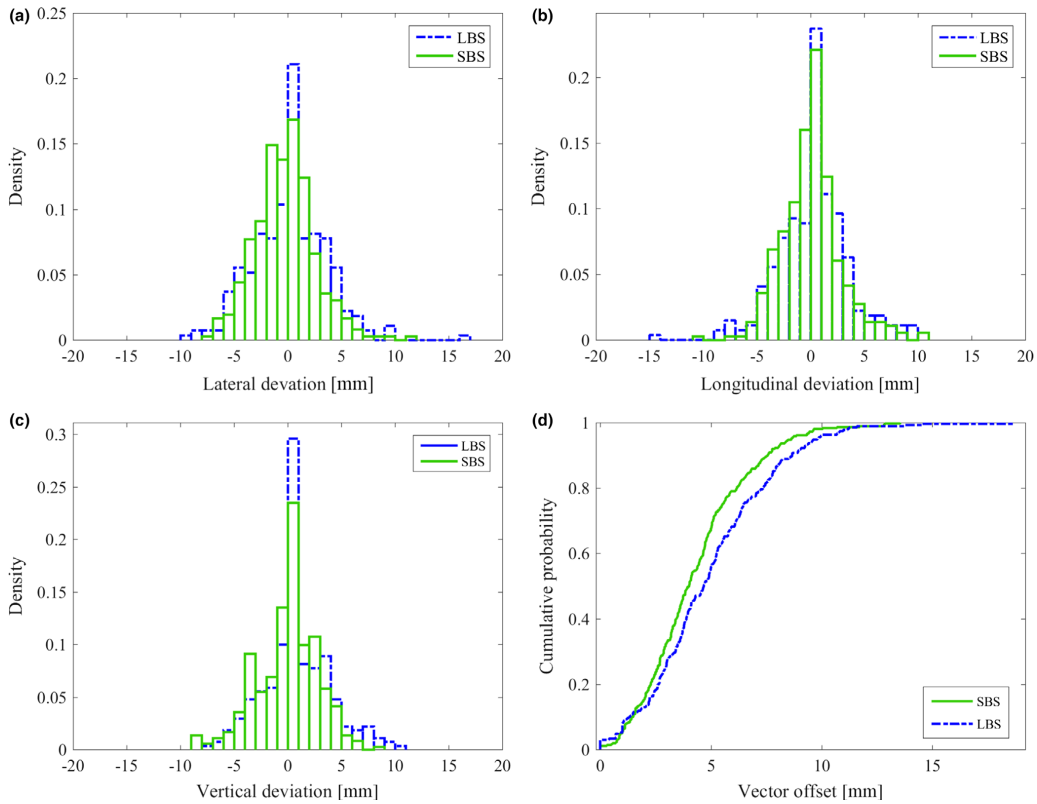

FIG. 5. Setup deviation for breast cancer patients receiving locoregional treatment positioned using laser-based setup (LBS) and surface based setup (SBS). Histograms of the setup accuracy in (a) lateral, (b) longitudinal, and (c) vertical direction verified with field imaging. (d) The cumulative probability of the vector offset shows a significantly improved patient setup for SBS compared to LBS ($P < 0.01$).

spatial vector was within 11.0 mm for LBS and 5.0 mm for SBS. For LBS, the mean value (±1 SD) was −0.6 ± 3.3 mm, 0.8 ± 3.7 mm, 0.6 ± 3.7 mm in lat, lng, and vrt direction, respectively. For SBS, the mean value was −0.5 ± 1.4 mm, 0.4 ± 1.5 mm, 1.5 ± 1.7 mm in lat, lng, and vrt direction, respectively (Fig. 4). Significant difference was found in the vrt direction ($P < 0.01$).

3.B | Locoregional treatment

The median vector offset was 4.7 (0–18.7 mm) and 4.0 (range: 0–13.5 mm) for LBS and SBS, respectively ($p < 0.01$). For LBS, the mean value (±1 SD) was 0.1 ± 3.4 mm, 0.1 ± 3.3 mm, 0.7 ± 3.1 mm in lat, lng, and vrt directions, respectively. For SBS, the mean value (±1 SD) was −0.5 ± 2.8, −0.1 ± 2.8, −0.3 ± 2.9 mm in lat, lng, and vrt directions, respectively. The result was statistically significant for lat and vrt directions ($P < 0.01$). The cumulative probability for positioning a patient within a spatial vector of 5 mm from isocenter was 55% for LBS and 67% for SBS (Fig. 5). For 90% of the treatment sessions, the spatial vector was within 9.1 and 7.6 mm for LBS and SBS, respectively. For LBS and SBS, 54% and 70% of all treatment sessions were within the clinical tolerance of ≤4 mm in all three directions (lat, lng, vrt), respectively (Fig. 5). A small but not significant difference was observed ($P = 0.02$) for the vector offset, comparing the single camera system with the three camera system for SBS (Fig. 6).

4 | DISCUSSION

For both the patient groups receiving tangential and locoregional breast cancer treatment, the patient setup was significantly improved using the Catalyst™ system. For locoregional treatments, the clinical criteria (≤4 mm) were fulfilled for 16% more treatment sessions using SBS compared to LBS. The corresponding improvement for tangential treatments was 11%. This could potentially lead to a reduced amount of verification imaging in the clinic. Also, the standard setup deviation for patients receiving tangential treatment was

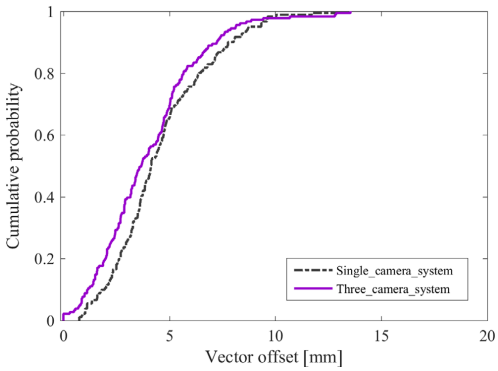

FIG. 6. For the breast cancer patients receiving locoregional treatment, a total of 362 verification images were evaluated for patients positioned using SBS at a single camera Catalyst system (181 verification images) and a three camera Catalyst system (181 verification images). The cumulative probability of the vector offset shows a nonsignificant improved patient setup for three camera compared to single camera system (P = 0.02).

approximately reduced by half. For a few treatment sessions, deviations up to 11 mm were observed for locoregional breast cancer patients using SBS, which also was observed by Stanley et al. using CBCT as verification imaging.[13] In both LBS and SBS groups, large setup deviations were found when the patient's arm was incorrectly positioned. For SBS, the therapists manually corrected the patient setup according to the criteria for posture, however, for a few treatments sessions, the criteria were not achievable due to shoulder stiffness after surgery.

The back-projected color map had a great impact on correction of patient posture to the planned position, while LBS deficiencies were largely caused by the lack of information of the patient posture. Degraded image quality for SBS was observed for a few patients, due to nonoptimal camera settings. This was observed for individual patients, and also, for the surface covered with bolus. The camera exposure setting was optimized to scan the patient's skin color, and since the color of the bolus deviated from the patient skin color the camera got overexposed in this area. In the area of overexposure, the Catalyst™ fails to reconstruct a surface, hence, information about the bolus position will be lost. Also, since the deformable algorithm values area above the isocenter in the calculation, an area where the bolus often is positioned, vital information is lost. For a single camera system and a locoregional patient with bolus, the surface that was covered was the lower parts of the thorax, arm, and chin. Since the arm and chin are not optimal anatomical structures to use for patient setup, this contributes to inaccuracy in this study. For the three camera system, better surface coverage over the treatment area was observed, contributing to a more accurate patient setup. The single camera system was installed in the ceiling by the foot end of the couch. The reconstructed surface depended on how much of the patient surface the camera was able to detect. For tangential treatments, a breastboard pitch of 7.5° was used which favored the Catalyst™ camera, hence, the patient was tilted toward the camera. For patients receiving locoregional treatments, a breastboard pitch of 0° was used and in combination with a cranial isocenter, important surface above the isocenter was not covered using the single camera system. This loss of surface had a negative impact on the accuracy of the patient setup (Fig. 3). For 17 out of the 76 patients in this study, the mass center of the PTV was used instead of the isocenter for the setup calculation in the Catalyst™ system. However, since the surface above the calculation point was lost, the setup accuracy was similar to using the calculated isocenter. For the three camera system, for locoregional treatment, and single camera for tangential treatment, the treatment site was well covered, which according to our results, as well as in the study of Chang et. al, leads to accurate positioning.[10] In the time span between the in room SBS and the verification imaging during treatment, patient motion contributed to inaccuracy. For example, during one treatment session for one patient, an offset of −3, −6 and −3mm in lat, long and vrt direction, respectively, was observed for SBS. The Catalyst™ log showed that the registered shifts were caused by patient motion between the setup and the verification imaging. Also, verification images (MV or kV) are snapshots of the patient position, while the OSS system was averaging the patient position over 4 s to reduce the effect of the breathing motion which also might contribute to uncertainty. Another source of error was patient rotation, which was observed to be larger than the 3° tolerance in the study protocol for individual treatment sessions using SBS. Rotations >2° has previously been reported by Guckenberger et al in 26% of patients with thoracic tumors, with a maximal rotational error of 8°.[18] The authors could not observe any correlation between the rotational error and the magnitude of the translational error. Since three degree of freedom couches cannot compensate for rotations, an advantageous feature using SBS is the ability to manually correct for rotations inside the treatment room prior to verification imaging and/or treatment.

5 | CONCLUSION

This study showed that surface based setup, using the Catalyst™ system can replace the conventional laser-based setup for tangential and locoregional breast cancer treatments, regardless if a single or a three camera system was used. Additional information of the patient posture was provided using surface based setup compared to laser-based setup, which improved positioning. Daily surface guided radiotherapy for breast cancer patients can thus reduce time and dose associated with verification imaging.

ACKNOWLEDGMENT

Our research is partly financially supported by C-RAD AB, Uppsala, Sweden, however, the authors alone are responsible for the content, analyses, and writing.

CONFLICT OF INTEREST

All authors approved the final manuscript, and declared that they have no potential conflict of interest to this work.

REFERENCES

1. Darby S, McGale P, Correa C, et al. Effect of radiotherapy after breast-conserving surgery on 10-year recurrence and 15-year breast cancer death: meta-analysis of individual patient data for 10,801 women in 17 randomised trials. *Lancet*. 2011;378:1707–16.
2. Gagliardi G, Bjöhle J, Lax I, et al. Radiation pneumonitis after breast cancer irradiation: analysis of the complication probability using the relative seriality model. *Int J Radiat Oncol Biol Phys*. 2000;46:373–381.
3. Gyenes G, Rutqvist LE, Liedberg A, et al. Long-term cardiac morbidity and mortality in a randomized trial of pre- and postoperative radiation therapy versus surgery alone in primary breast cancer. *Radiother Oncol*. 1998;48:185–90.
4. Björk P. Report from SSM's scientific council on ionizing radiation within oncology. C.D.S. Peter Björk, Editor. 2010, Swedish Radiation Safety Authority: www.stralsakerhetsmyndigheten.se
5. Laaksomaa M, Kapanen M, Haltamo M, et al. Determination of the optimal matching position for setup images and minimal setup margins in adjuvant radiotherapy of breast and lymph nodes treated in voluntary deep inhalation breath-hold. *Radiation Oncology*. 2015;10:76.
6. Dawson LA, Sharpe MB. Image-guided radiotherapy: rationale, benefits, and limitations. *Lancet Oncol*. 2006;7:848–858.
7. Djajaputra D, Li S. Real-time 3D surface-image-guided beam setup in radiotherapy of breast cancer. *Med Phys*. 2005;32:65–75.
8. Pallotta S, Marrazzo L, Ceroti M, Silli P, Bucciolini M. A phantom evaluation of Sentinel (TM), a commercial laser/camera surface imaging system for patient setup verification in radiotherapy. *Med Phys*. 2012;39:706–712.
9. Shah AP, Dvorak T, Curry MS, Buchholz DJ, Meeks SL. Clinical evaluation of interfractional variations for whole breast radiotherapy using 3-dimensional surface imaging. *Pract Radiat Oncol*. 2013;3:16–25.
10. Chang A, Zhao H, Wahab SH, et al. Vidoe surface guidance for external beam partial breast irradiation. *Pract Radiat Oncol*. 2012;2:97–105.
11. Li H, Sumner RW, Pauly M. Global Correspondence Optimization for Non-Rigid Registration of Depth Scans. In: *Eurographics Symposium of Geometry Processing*; 2008. Zurich: Computer Graphics Forum.
12. Crop F, Pasquier D, Baczkiewic A, et al. Surface imaging, laser positioning or volumetric imaging for breast cancer with nodal involvement treated by helical TomoTherapy. *J Appl Clin Med Phys*. 2016;17:200–211.
13. Stanley DN, McConnell KA, Kirby N, Gutiérrez AN, Papanikolaou N, Rasmussen K. Comparison of initial patient setup accuracy between surface imaging and three point localization: a retrospective analysis. *J Appl Clin Med Phys*. 2017;18:58–61.
14. Stieler F, Wenz F, Shi M, Lohr F. A novel surface imaging system for patient positioning and surveillance during radiotherapy. A phantom study and clinical evaluation. *Strahlenther Onkol*. 2013;189:938–944.
15. Pears NE. Optical Triangulation Range Sensors, in Optical Triangulation Range Sensors for Vehicle Manoeuvres. S.C.a.P. Probert, Editor. 1994, World Scientific Publishing Co. p. 85–106.
16. Nutti B, Kronander Å, Nilsing M, Maad K, Svensson C, Li H.*Depth Sensor-Based Realtime Tumor Tracking for Accurate Radiation Therapy*. Eurographics.2014;10–13.
17. de Boer HC, van Sörnsen de Koste JR, Creutzberg CL, Visser AG, Levendag PC, Heijmen BJM. Electronic portal image assisted reduction of systematic set-up errors in head and neck irradiation. *Radiother Oncol*. 2001;61:299–308.
18. Guckenberger M, Meyer J, Vordermark D, Baier K, Wilbert J, Flentje M. Magnitude and clinical relevance of translational and rotational patient setup errors: a cone-beam CT study. *Int J Radiat Oncol Biol Phys*. 2006;65:934–942.

Paper V

Check for updates

Validation of a commercial deformable image registration for surface-guided radiotherapy using an ad hoc-developed deformable phantom

Stefania Pallotta[a)]
Department of Biomedical, Experimental and Clinical Sciences "Mario Serio", University of Florence, Florence, Italy
Medical Physics Unit AOU Careggi, Florence, Italy

Malin Kugele
Department of Hematology, Oncology and Radiation Physics, Skåne University Hospital, Lund, Sweden
Medical Radiation Physics, Department of Clinical Sciences, Lund University, Lund, Sweden

Laura Redapi
Department of Biomedical, Experimental and Clinical Sciences "Mario Serio", University of Florence, Florence, Italy

Sofie Ceberg
Medical Radiation Physics, Department of Clinical Sciences, Lund University, Lund, Sweden

(Received 15 June 2020; revised 31 August 2020; accepted for publication 30 September 2020; published 27 October 2020)

Purpose: The use of optical surface systems (OSSs) for patient setup verification in external radiation therapy is increasing. To manage potential deformations in a patient's anatomy, a novel deformable image registration (DIR) tool has been applied in a commercial OSS. In this study we investigate the accuracy of the DIR as compared to rigid image registration (RR).
Methods and Materials: The positioning accuracy of the DIR and RR implemented in the OSS was investigated using an *ad hoc*-developed anthropomorphic deformable phantom, named Mary.

The phantom consists of 33 slices of expanded polystyrene slabs shaped thus to simulate part of a female body. Anatomical details, simulating the ribs and spinal cord, together with 10 inner targets at different depths are included in thorax and abdominal parts. Mary is capable of realistic body movements and deformations, such as head and arm rotations, body torsion and moderate breast/abdomen swelling. The accuracy of DIR and RR was investigated for four internal targets after deliberately deforming the phantom nine times. Breast and abdomen enlargements and torsions around x, y, and z axes were applied. For reference purposes, rigid displacements (where Mary's anatomy was kept intact) were included. The phantom was positioned on the linac couch under the OSS guidance and for each target and displacement a CBCT was acquired. The accuracy of DIR and RR was assessed evaluating the difference in means of absolute values between CBCT and the OSS registration parameters (lateral, longitudinal, vertical, rot, pitch, and roll), using both a reference surface extracted from CT (CTr) or acquired with the OSS (OSSr). A comparison of the four different combinations, DIR + OSSr, DIR + CTr, RR + OSSr, and RR + CTr, was carried out to evaluate the position accuracy for the various combinations. Finally, the positioning accuracy of the different target positions using only OSSr was investigated for the DIR. A paired sample Wilcoxon signed-rank test ($P < 0.05$) and a two-tailed Mann–Whitney test ($P < 0.05$) were carried out.
Results: The DIR in combination with OSSr showed significantly ($P < 0.05$) improved positioning accuracy in the lateral and longitudinal directions and in pitch, compared to RR, when deformations were applied to Mary. The positioning accuracy improved from 1.9 ± 1.5 mm, 1.1 ± 0.8 mm to 1.1 ± 1.2 mm, 0.6 ± 0.5 mm in lateral and longitudinal directions, respectively, and from $0.8 \pm 0.6°$ to $0.4 \pm 0.4°$ in pitch, using DIR compared to RR. Both the DIR and RR showed a similar positioning accuracy when rigid displacements of Mary were applied. For DIR, the OSSr generally showed improved calculation accuracy compared to CTr.

Independent of the reference image used, the target position influenced the registration accuracy, and hence, one target could not be evaluated using RR due to its inability to calculate the correct position.
Conclusions: Improved positioning accuracy was observed for DIR with respect to RR when deformations of Mary's anatomy were applied. For both DIR and RR, improved positioning accuracy was observed using OSSr as compared to CTr. The position of the target inside the phantom influenced the positioning accuracy for DIR. © *2020 American Association of Physicists in Medicine* [https://doi.org/10.1002/mp.14527]

Key words: accuracy, deformable image registration, optical scanning systems, patient set-up, surface registration

1. INTRODUCTION

Modern radiotherapy systems, applying a highly conformal dose distribution, require accurate patient positioning techniques. Widespread verification systems, such as portal imaging, cone-beam computed tomography (CBCT), or megavoltage computed tomography use ionizing radiation to acquire an image representing the treatment position. Data concerning patient position can also be derived using optical surface systems (OSSs).[1,2] OSSs use the external surface of the patient for patient positioning, which allows increased accuracy in patient positioning with respect to three-point laser localization in superficial treatment sites, such as the breast,[3–7] and rigid body parts, such as the head.[8–10] One of the major advantages of using OSSs for patient positioning is the potential to reduce daily verification imaging, and hence, the imaging dose to the patient.[3] The performance of OSSs have shown to be comparable to CBCT and comparable or superior with respect to portal imaging when used on phantoms.[11–14] However, the accuracy of OSSs have shown to vary depending on the treatment site, with decreased accuracy for deeply situated targets, mainly in the abdomen and pelvis, when compared to CBCT.[15–18] In several commercial OSSs, rigid registration (RR) between the reference surface and the acquired surface is used to calculate to patient position.[19] However, changes in anatomical structures and posture differences can present challenges for OSSs. To reduce the impact of the patient's external surface deformations on the surface guidance accuracy, the OSS CatalystHD™ (C-RAD Positioning AB, Uppsala, Sweden) uses a deformable image registration (DIR) tool in the setup evaluation software.[20,21] The use of DIR requires an in-depth evaluation to understand the algorithm's strengths and weaknesses and, at the same time, to highlight the implications of its clinical use. DIR algorithm validation can be performed using deformable phantoms, synthetic phantoms, and clinical patient data.[22] The main advantage of using a deformable phantom is that the whole treatment chain can be evaluated to assess the global OSS performance in 6 degrees of freedom.

Catalyst™ is the only OSS to date which has implemented both a DIR and a RR algorithm. To our knowledge, this is the first study comparing the performance of the two registration algorithms. Another study[23] evaluates the DIR performances applying deformations and rigid displacements to a synthetic phantom, but no comparison between DIR and RR was performed. Moreover, to carry out the comparison in a realistic scenario, we developed a deformable anthropomorphic phantom, named "Mary," capable of simulating realistic body movement and deformation. The phantom Mary has an external surface suitable in both color and texture for OSS acquisitions and contains structures and targets that are detectable with ionizing radiations.

The purpose of this study was to investigate the accuracy of DIR as compared to RR, using the deformable phantom Mary and CBCT as a reference. DIR positioning accuracy was investigated for different target positions and anatomical deformations, as well as for type of reference surface used.

2. MATERIALS AND METHODS

2.A.. Catalyst™ deformable image registration

In Catalyst™ (C-RAD Positioning AB, Uppsala, Sweden), a DIR algorithm is implemented[20,21] to register the acquired surface to the reference surfaces. The reference surface can be a 3D surface previously acquired (OSSr) or a surface rendered from a CT planning study (CTr). Since the patient anatomy can deform during the treatment, a DIR algorithm could potentially provide a more accurate target volume registration than a global RR approach. Two deviations of patient setup are calculated: the posture and the isocenter deviations. The posture deviation guides the therapists during patient positioning with a color-coded distance map that is projected onto the patient's skin, which helps minimize the differences between live and patient reference positions. The isocenter deviation indicates possible fine tuning of patient setup with couch adjustment expressed as three translations and three rotations. The isocenter error evaluation is a two-step process that consists of a deformable surface registration of the reference and acquired surfaces followed by a volumetric deformable model, which deduces the isocenter position from the surface differences. In the first step, both reference and live surfaces are replaced by a surface mesh of triangles. Then a deformation node graph, associated with the reference surface, is built and correspondence points on the live surface are obtained following a closest point approach. A nonlinear optimization algorithm is then employed to generate the reference mesh deformation that minimizes the sum of each deformation node energy. The stiffness of the mesh is initially set high, but it is subsequently reduced in the iterative process, to account for local deformations. This approach is adopted with the aim of maintaining maximum rigidity.

In the second step, a volumetric mesh, consisting of uniformly distributed cubes, is created to relate all nodes of the volumetric mesh to the nodes of the reference surface mesh. Based on the source mesh node transformations evaluated in the first step, the algorithm calculates the translations and rotations of the isocenter.

2.B.. The deformable phantom

The deformable phantom "Mary" (Fig. 1) is an anthropomorphic phantom developed in-house at the University of Florence, Florence, Italy and designed to simulate realistic body movement and deformation. For x-ray imaging purposes, structures were placed in the body of the phantom to simulate bony anatomy (spinal cord and ribs).

The phantom was built by assembling 33 slices (2-cm thick) of expanded polystyrene slabs shaped thus to simulate part of a female body (from the head to the abdomen). In order to create anatomical details simulating the ribs and spinal cord, an incision was made in the internal surface of 10 slices and filled with clay, targets were simulated by drilling eight holes in select slices and filled with clay, and a duct running along the entire phantom was built to simulate the spinal cord. All the slices were then connected using a rope

FIG. 1. Pictures of the deformable phantom "Mary" showing different postures due to torsion of the thorax or deformations of the breast structures and the abdomen. A 3D model showing the phantom's internal structures simulating the bony anatomy of a female thorax. [Color figure can be viewed at wileyonlinelibrary.com]

that runs through the duct along the phantom's body. The distance between adjacent slices was modifiable in order to enable thorax bending and torsion. A cellulose envelope, used to cover the thorax and abdominal slices, makes the external body contour visible in CT and CBCT images. Two separate objects made with polystyrene foam (not visible in CBCT) were fixed to the phantom to simulate arms. Three rubber sacks fixed under the breasts and in the abdomen region can be inflated via three small pipes running out from the phantom body to simulate breast and abdomen swelling. The complete phantom is covered in a white Lycra tissue. Independent and realistic head rotation, arm flexion, body torsion around a longitudinal axis, and bending around lateral and vertical axes can be achieved. Breast and abdomen enlargement can also be simulated. CT, CBCT, and surface images of Mary were acquired to demonstrate the phantom usability.

2.C.. Assessment of the deformable image registration accuracy

Mary was used to evaluate the DIR as compared to RR, using CBCT as reference. All surface images, CT and CBCT images were acquired at the Radiotherapy department in Lund, Sweden.

Comparison between the DIR and RR was carried out for both rigid displacements while keeping the anatomy of the Mary's body intact ($Mary_{rigid}$), and deformed displacements where the anatomy of Mary's body was altered with torsions and/or deformations ($Mary_{deformed}$).

The positioning accuracy with regard to the reference surface used, both the CT data-derived surface (CTr) and a surface captured with the OSS (OSSr), was also investigated.

CT acquisition of Mary was performed using a Siemens Somatom definition AS plus (Siemens Medical Solutions, Erlangen, Germany) with a slice thickness of 1 mm. The CT data were sent to the TPS (Eclipse, v 13.6, Varian Medical Systems, Palo Alto, CA) where the external phantom surface was segmented and manually edited, and four representative phantom targets were selected. For each target, an RT plan was generated and sent to the Catalyst™ (HD v5.2.1) system together with the external surface to be used as reference (CTr). The same RT plans were shared with a linac (TrueBeam 2.5, Varian Medical Systems, Palo Alto, CA) by means of ARIA R&V system. The OSSr was acquired for each of the four targets using a CatalystHD™ OSS while the phantom

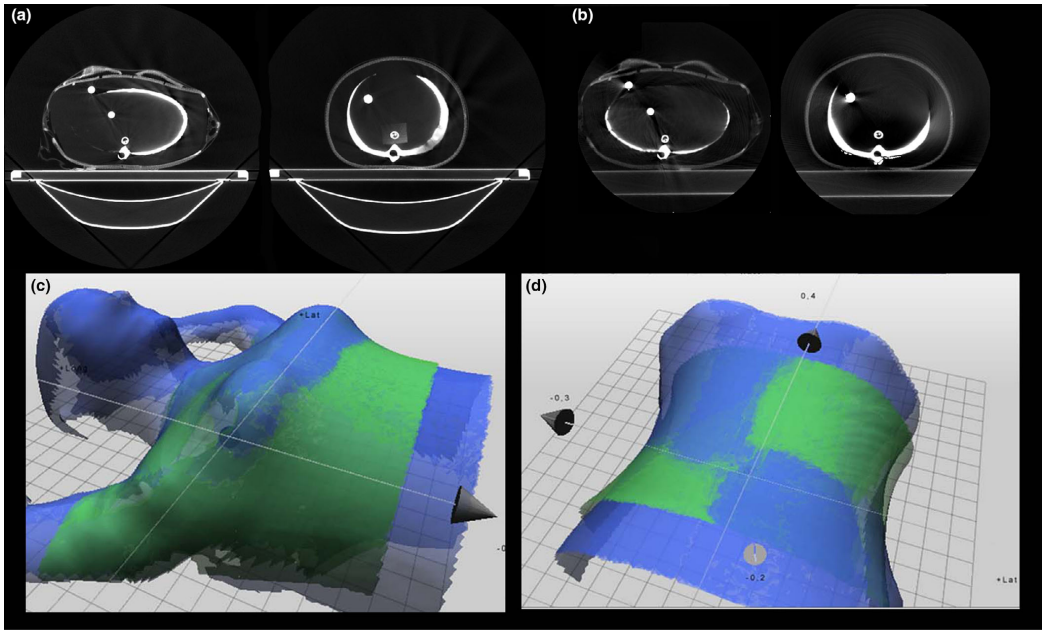

FIG. 2. Some selected slices of computed tomography (CT) (a) and cone-beam CT (CBCT) (b) acquisitions of Mary. In (c) and (d), two examples of Catalyst™ acquisitions showing the reference surface images in green and the live surface images in blue. Torsion of Mary around the y-axis is shown in (d), where the blue and the green surfaces no longer overlap, and the live surface is either above or below the reference surface resulting in a chess pattern. [Color figure can be viewed at wileyonlinelibrary.com]

was positioned in the isocenter verified by CBCT imaging. Prior to OSS acquisitions, Mary was positioned on the treatment couch and the surface images acquisition width was optimized for each target. A scanning volume, similar in extension to that used for patients, was set in order to exclude surface anatomy far away from the considered target.

The phantom was then deliberately deformed manually, and, for each target, was positioned at the isocenter using couch shifts under the OSS guidance and with OSSr as a reference surface. Moderate deformations were used in order to evaluate OSS in a clinically realistic scenario. Mary is not fitted with any instrument to measure the deformations applied but, using CBCT, it is possible to obtain an *a posteriori* estimate of the extent of deformation.

Nine deformations were tested: five torsions around x, y, and z axes, two breast, and two abdomen enlargements. While the five torsions were used to test the DIR and RR performances on all target positions, the breast and abdomen deformations were only used for the targets close to the deformed regions.

Three rigid displacements in which Mary was positioned by the OSS guidance without any deformations applied were carried out successively for each target using couch shifts under the OSS guidance with OSSr as a reference surface.

For each positioning of $\text{Mary}_{\text{rigid}}$ and $\text{Mary}_{\text{deformed}}$, a surface image and a CBCT was acquired. The CBCT was registered on the planning CT using the automatic registration software based on mutual information and subsequently refined manually, following a local approach focused on the target. The surface images were acquired for an offline calculation of the isocenter position, enabling both DIR and RR to be evaluated.

The differences in means of absolute values between the CBCT and DIR or RR registration parameters (Δlat, Δlong, Δvert, Δpitch, Δroll, Δrot) were assessed offline using both CTr and OSSr as reference surfaces. A comparison was carried out between the various combinations of DIR + CTr, DIR + OSSr, RR + CTr, and RR + OSSr, to investigate the optimal combination for accurate patient positioning.

A statistical analysis was carried out using a paired sample Wilcoxon signed-rank test ($P < 0.05$). A statistical analysis between deformations and rigid displacements was carried out using a two-tailed Mann–Whitney U test ($P < 0.05$). All statistical analyses were performed with OriginPro (version 9.0.0, OriginLab Corporation, Northampton, MA).

3. RESULTS

3.A.. The deformable phantom

In Fig. 2 some samples of CT, CBCT, and surface images of Mary are shown. The internal anatomical structures and

TABLE I. Mean values and standard deviations of the absolute differences between the OS and cone-beam computed tomography (CBCT) for deformations and rigid displacements using OSSr and CTr for DIR and RR algorithms (for targets 1, 2, and 3). Only the *P* values expressing a statistically significant difference between DIR and RR at the 0.05 level are reported.

		DIR					RR				
		Δlat (mm)	Δlong (mm)	Δvert (mm)	Δrot (°)	Δpitch (°)	Δroll (°)	Δlat (mm)	Δlong (mm)	Δvert (mm)	Δrot (°)	Δpitch (°)	Δroll (°)
Mary$_{deformed}$	OSSr	1.1 ± 1.2	0.6 ± 0.5	1.0 ± 0.9	0.4 ± 0.5	0.4 ± 0.4	0.6 ± 0.4	1.9 ± 1.5	1.1 ± 0.8	1.3 ± 1.0	0.6 ± 0.6	0.8 ± 0.6	0.4 ± 0.4
p(DIR vs RR)		<0.01	0.01			<0.01							
Mary$_{rigid}$	OSSr	0.7 ± 0.6	0.7 ± 0.5	0.7 ± 0.4	0.3 ± 0.2	0.5 ± 0.3	0.7 ± 0.3	0.9 ± 0.9	0.5 ± 0.4	1.0 ± 1.2	0.2 ± 0.2	1.1 ± 0.6	0.6 ± 0.4
p(DIR vs RR)						0.02							
Mary$_{deformed}$	CTr	2.6 ± 1.2	1.1 ± 0.9	1.3 ± 0.8	0.7 ± 0.5	0.8 ± 0.5	1.2 ± 0.4	2.2 ± 1.6	1.5 ± 0.9	1.6 ± 1.4	0.8 ± 0.5	0.8 ± 0.4	0.7 ± 0.5
p(DIR vs RR)													<0.01
Mary$_{rigid}$	CTr	2.1 ± 1.0	1.0 ± 0.8	1.7 ± 0.7	0.4 ± 0.2	0.8 ± 0.4	1.3 ± 0.6	0.8 ± 0.8	0.9 ± 0.6	2.5 ± 1.0	0.6 ± 0.1	0.9 ± 0.4	1.0 ± 0.2
p(DIR vs RR)				<0.01				<0.01					

DIR, Deformable Image Registration; RR, Rigid Registration

targets, as well as the external surface, were visible in CT and CBCT images and the external surface is well reproduced in surface images.

3.B.. Assessment of the deformable image registration accuracy

3.B.1.. Comparison between DIR and RR algorithms

Using OSSr as reference image, improved positioning accuracy was observed for DIR as compared to RR in Δlat, Δlong, and Δpitch ($P < 0.05$) when deformed displacements were applied to Mary (Table I). In this case, the mean positioning accuracy, evaluated for all targets and deformations, was improved from 1.9(±1.5)mm, 1.1(±0.8)mm to 1.1(±1.2) mm, 0.6(±0.5)mm in lateral and longitudinal directions, respectively, and from 0.8°(±0.6°) to 0.4°(±0.4°) in Δpitch. For rigid displacements of Mary and using OSSr, the positioning accuracy of DIR and RR was equivalent for Δlat, Δlong, Δvert, Δrot and Δroll (Fig. 3 and Table I). For Δpitch, a significant improvement in positioning accuracy was observed for DIR.

The Catalyst™ rigid registration algorithm, in combination with OSSr, was not able to evaluate the registration parameters for target 4, probably due to the inability of the OSS algorithm to find the global minimum of the cost function. For this reason, all the data related to this target were excluded from this analysis.

Reduced positioning accuracy was observed using CTr for both DIR and RR, and hence, differences between the two registration algorithms could not be observed (Table I).

3.B.2.. Positioning accuracy dependency of reference surface used for DIR

The global performances of the DIR are described in Fig. 4 where the absolute differences between OSS and CBCT registration parameters, obtained by deforming the phantom (Mary$_{deformed}$) or applying rigid displacements (Mary$_{rigid}$), are reported for all targets using both OSSr and CTr. In Table II the mean values and standard deviations of the absolute differences for all targets are reported together with the p values between OSSr and CTr and between deformations and rigid displacements using OSSr and CTr at the significance level of 0.05. Improved positioning accuracy was observed for OSSr as compared to CTr for Δlat, Δlong, Δrot, and Δroll and Δlat, Δvert, Δrot, and Δroll for Mary$_{deformed\ and\ Maryrigid}$, respectively ($P < 0.05$; Table II). The positioning accuracy for the four internal targets in Mary$_{deformed}$ was reduced from (mean ± 1 SD) 2.4 ± 1.3 mm, 2.3 ± 2.2 mm, 2.2 ± 2.9 mm to 1.2 ± 1.2 mm, 1.0 ± 0.9 mm, 1.4 ± 1.8 mm, in Δlat, Δlong, and Δvert directions, respectively, for CTr as compared to OSSr (Table II). Comparison of the DIR algorithm's ability to handle deformed displacements as compared to rigid displacements of Mary showed no significant difference in Δlat,

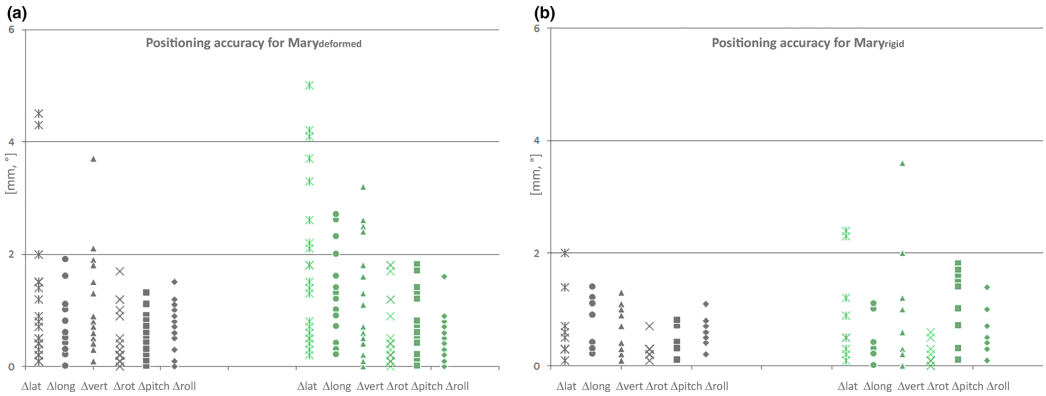

FIG. 3. The positioning accuracy using deformable image registration (in black) and RR (in green) for (a) deformed displacements and (b) rigid displacements of Mary. Each symbol represents the absolute difference between the corresponding cone-beam computed tomography and OS registration parameters evaluated for targets 1, 2, and 3 (target 4 was excluded) and displacement. In both cases OSSr was used. [Color figure can be viewed at wileyonlinelibrary.com]

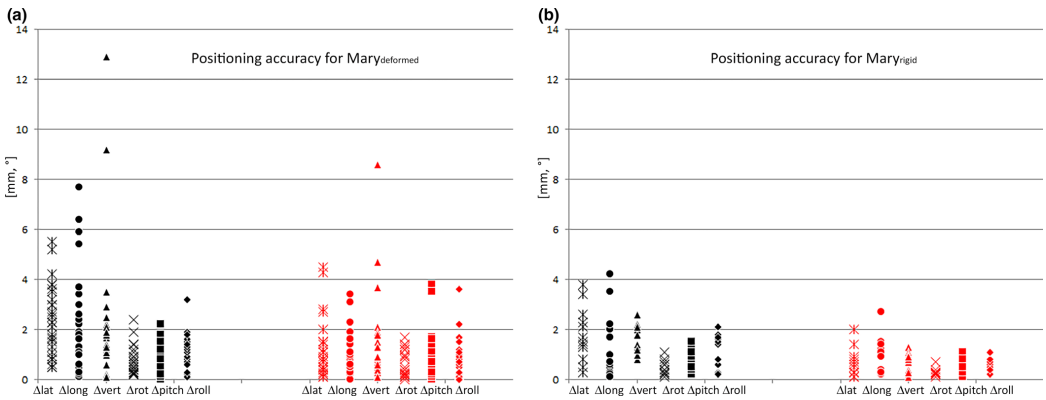

FIG. 4. Absolute differences between Catalyst™ (using the deformable image registration algorithm) and cone-beam computed tomography registration parameters evaluated for each target and displacement using OSSr (red) or CTr (black) as reference surface. In (a) the results obtained deforming the phantom (Mary $_{deformed}$) are reported and in (b) those obtained applying rigid displacements (Maryrigid) are reported. Using OSSr showed an improvement compared to using CTr. [Color figure can be viewed at wileyonlinelibrary.com]

Δlong, Δrot, Δroll, and Δpitch; however, a significant difference was observed in the Δvert direction, which is likely an effect of inflated abdomen and breast tissue (Table II).

An estimate of applied deformations, assessed comparing CBCT and CT Mary's surface, resulted up to 10 mm for breast and abdomen enlargement. Additionally, in torsions of Mary the CT-CBCT match showed differences of 6 mm of the phantom surface and up to 3 degrees of rotation.

3.B.3.. Positioning accuracy dependency of target position for DIR

The positioning accuracy of DIR in combination with OSSr, split by target, is reported in Fig. 5. Overall, a larger data dispersion was observed for target 4, both for deformations and rigid displacements, compared to the other three targets. Target 4 was situated in the abdominal area and was affected by inflation of the abdomen to a larger extent; hence, larger surface deformations in the z-direction (up to 8.8 mm) were observed by the DIR; however, no shift of the internal target was observed by the CBCT registration (Fig. 6).

4. DISCUSSION

The purpose of this study was to investigate the deformable surface image registration algorithm implemented in the optical surface scanning system Catalyst™ as compared to rigid registration used traditionally. The DIR has been in

TABLE II. Mean values (m) and standard deviation (σ) of the absolute differences between Catalyst™ using the deformable image registration (DIR) algorithm and CBCT for deformations and rigid displacements of Mary using OSSr or CTr as reference surface for all the targets. Only the *P* values expressing a statistically significant difference between OSSr and CTr or between deformations and rigid displacements using OSSr and CTr at the significance level of 0.05 are reported.

	OSSr						CTr					
	Δlat (mm)	Δlong (mm)	Δvert (mm)	Δrot (°)	Δpitch (°)	Δroll (°)	Δlat (mm)	Δlong (mm)	Δvert (mm)	Δrot (°)	Δpitch (°)	Δroll (°)
$\mathbf{Mary_{Deformed}}$	1.2 ± 1.2	1.0 ± 0.9	1.4 ± 1.8	0.6 ± 0.5	0.8 ± 0.9	0.8 ± 0.8	2.4 ± 1.3	2.3 ± 2.2	2.2 ± 2.9	0.7 ± 0.5	0.9 ± 0.6	1.2 ± 0.7
p(OSSr vs CTr)	**<0.01**	**<0.01**		**0.02**		**<0.01**						
$\mathbf{Mary_{Rigid}}$	0.7 ± 0.6	0.9 ± 0.7	0.7 ± 0.4	0.3 ± 0.2	0.6 ± 0.3	0.6 ± 0.3	1.8 ± 1.1	1.4 ± 1.3	1.8 ± 0.6	0.5 ± 0.3	0.8 ± 0.4	1.1 ± 0.7
p(OSSr vs CTr)	**<0.01**		**<0.01**	**0.04**		**0.01**						
p ($Mary_{deformed}$ vs $Mary_{rigid}$)			**<0.01**									

OSSr, Optical Surface System reference; CTr, CT reference

clinical use since 2016 but an in-depth analysis of the system's performance has not yet been fully undertaken. This aspect is important because knowing the limits of the systems helps to establish appropriate site-specific tolerances necessary for a routine use of OSS in clinical use. Evaluating the clinical application of OSSs is also important as relevant technical guidelines have not yet been published.

One significant drawback of using OSSs for patient setup is the potentially reduced correlation between the external surface and internal anatomy when deformations and posture variations occur. Due to the infinite possible combinations of posture error and deformations, a complete validation of a DIR algorithm is extremely difficult and, until now, limited to software approaches[23] or rigid phantom studies.[13,15] In order to evaluate the DIR in a clinically realistic scenario, we developed a deformable phantom capable of realistic movements such as body torsion, bending or enlargement of the breast and abdomen.

To compare our results with those of previous studies, rigid displacements were also considered. The main results of our study consist of the comparison between the deformable and rigid registration algorithms implemented in Catalyst™. The results in this study demonstrate a significant advantage in using DIR over RR when anatomical deformations were considered. Differences between DIR and RR were small and, as the impact of these differences in terms of dose distributions have not been included in this study, it is difficult to assess if the use of DIR could lead to a clinical advantage in case of deformations or not.

As expected, both DIR and RR show similar results when rigid displacements of Mary were investigated. The results obtained for rigid displacements are comparable to those obtained in previous studies[15,23] using the same OSS. However, for target 4, the RR was not capable of carrying out the positioning calculation, showing the limitations of the CatalystTM RR algorithm. Also, the DIR showed decreased accuracy for positioning of target 4, due to abdominal enlargements applied to Mary, although the internal target was fixed to bony anatomy and was not affected by this enlargement. This comparison provides an order of magnitude between the DIR and RR and suggests that caution should be taken when using either DIR or RR in the case of large deformations. A major limitation in this study was the inability to measure the level of deformity applied to Mary; hence, the study is a relative comparison between DIR and RR in the presence of deformations.

Significantly improved results were observed using OSSr over CTr for both deformed displacements and rigid displacements of the phantom Mary. The sensitivity to the reference surface used implies that a systematic error was present for the CTr, most likely due to inaccuracy of the external surface delineation in the TPS or lower density of the points for the distance map used in the initial calculation step.

DIR positioning accuracy of the four internal targets was also investigated. Our study highlights a difference in positioning accuracy using DIR dependent on the target position.

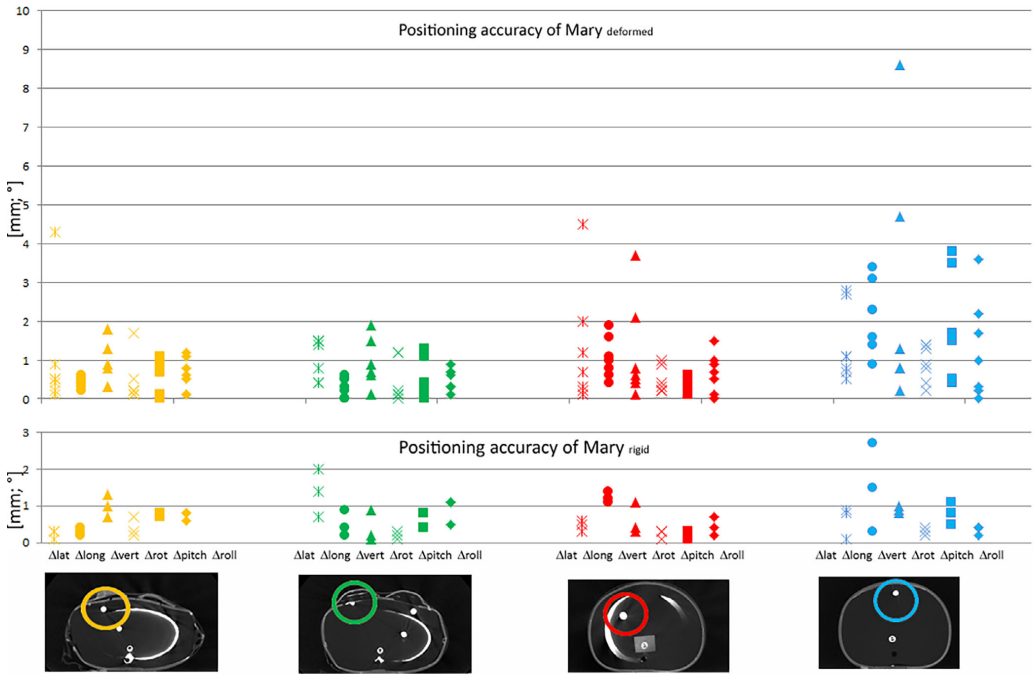

FIG. 5. The positioning accuracy of the deformable image registration in combination with OSSr for each target and for deformed displacements and rigid displacements of Mary. Targets 1, 2, 3, and 4 are represented by yellow, green, red, and blue colors, respectively, and are highlighted in some Mary images in the last row. [Color figure can be viewed at wileyonlinelibrary.com]

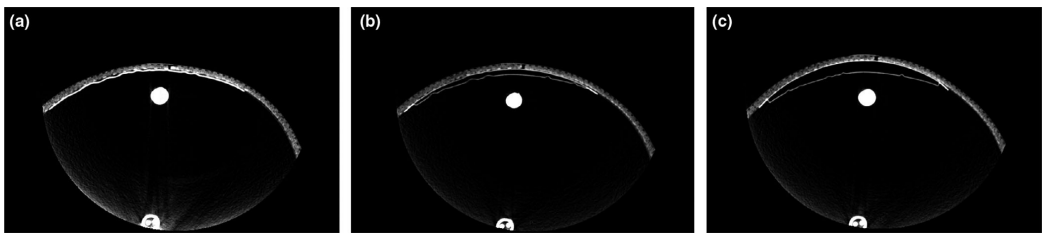

FIG. 6. Cone-beam computed tomography images of target 4 showing (a) no abdomen enlargement, (b) small abdomen enlargement, and (c) medium abdomen enlargement.

Targets located in body parts with no or poor gradient (lack of anatomical structures) in the external surface were observed to be challenging for the OSS, and reduced positioning accuracy was therefore observed. Also, decreased positioning accuracy was observed for target 1 when a large breast enlargement was applied. From this study we infer that the most problematic situations for DIR to handle are body enlargements in regions with poor shape gradient (such as the abdomen or thorax in men).

A previous study on the deformable registration algorithm performance of the Catalyst™ system was conducted by Meyer et al[23] on a synthetic phantom. The authors evaluated the system by introducing some deformations of the body surface extracted from a real phantom CT study in relation to breast deformation in size, hunching/arching back, and distended/deflated abdomen. A comparison of our study results and those obtained by Meyer et al is quite difficult due to the different approaches followed. We placed the phantom Mary like an actual patient, simulating a realistic clinical scenario, while Meyer et al. compare applied transformation with the registration parameters obtained using the DIR algorithm implemented in Catalyst™.

In this study, breast and abdominal enlargements were also included, which had an impact on all registration parameters, in contrast to Meyer et al who only highlighted a poor accuracy estimate of the translation along the vertical axis or pitch.

5. CONCLUSIONS

A deformable thorax phantom, capable of realistic deformations was developed and used to compare deformable and rigid image registration algorithms.

Differences between DIR and RR were small; however, the use of DIR slightly improves the positioning accuracy compared to RR when clinically realistic deformations were applied to the deformable phantom. As expected, the difference between DIR and RR was not observed when rigid displacements of the phantom were considered. For targets located in body parts with poor shape gradients or when larger deformations were applied to the deformable phantom, reduced positioning accuracy was observed for DIR. Also, using a reference surface captured by the OSS improved the positioning accuracy with respect to a CT derived surface. The approach we propose is suitable for quality assurance of different registration algorithms developed for OSSs.

[a)]Author to whom correspondence should be addressed. Electronic mail: stefania.pallotta@unifi.it; Telephone: +39 055 2751831; Fax: +39 055 2751835.

REFERENCES

1. Freislederer P, Kügele M, Öllers M, et al. Recent advanced in surface guided radiation therapy. *Radiat Oncol*. 2020;15:187.
2. Hoisak JDP, Pawlicki T. The role of optical surface imaging systems in radiation therapy. *Semin Radiat Oncol*. 2018;28:185–193.
3. Kügele M, Mannerberg A, Nørring Bekke S, et al. Surface guided radiotherapy (SGRT) improves breast cancer patient setup accuracy. *J Appl Clin Med Phys*. 2019;20:61–68.
4. Wei X, Liu M, Ding Y, et al. Setup errors and effectiveness of Optical Laser 3D Surface imaging system (Sentinel) in postoperative radiotherapy of breast cancer. *Sci Rep*. 2018;8:7270.
5. Cravo Sá A, Fermento A, Neves D, et al. Radiotherapy setup displacements in breast cancer patients: 3D surface imaging experience. *Rep Pract Oncol Radiother*. 2018;23:61–67.
6. Fassi A, Ivaldi GB, de Fatis PT, et al. Target position reproducibility in left-breast irradiation with deep inspiration breath-hold using multiple optical surface control points. *J Appl Clin Med Phys*. 2018;19:35–43.
7. Crop F, Pasquier D, Baczkiewic A, et al. Surface imaging, laser positioning or volumetric imaging for breast cancer with nodal involvement treated by helical TomoTherapy. *J Appl Clin Med Phys*. 2016;17:200–211.
8. Li G, Ballangrud A, Chan M, et al. Experience with two frameless stereotactic radiosurgery (fSRS) systems using optical surface imaging for motion monitoring. *J Appl Clin Med Phys*. 2015;16:149–162.
9. Covington EL, Fiveash JB, Wu X, et al. Optical surface guidance for submillimeter monitoring of patient position during frameless stereotactic radiotherapy. *J Appl Clin Med Phys*. 2019;20:91–98.
10. Cerviño LI, Detorie N, Taylor M, et al. Initial clinical experience with a frameless and maskless stereotactic radiosurgery treatment. *Pract Radiat Oncol*. 2012;2:54–62.
11. Bert C, Metheany KG, Doppke K, et al. A phantom evaluation of a stereo-vision surface imaging system for radiotherapy patient setup. *Med Phys*. 2005;32:2753–2762.
12. Pallotta S, Marrazzo L, Ceroti M, et al. A phantom evaluation of SentinelTM, a commercial laser/camera surface imaging system for patient setup verification in radiotherapy. *Med Phys*. 2012;39:706–712.
13. Stieler F, Wenz F, Shi M, Lohr F. A novel surface imaging system for patient positioning and surveillance during radiotherapy. A phantom study and clinical evaluation. *Strahlenther Onkol*. 2013;189:938–944.
14. Wiant D, Liu H, Hayes TL, Shang Q, Mutic S, Sintay B. Direct comparison between surface imaging and orthogonal radiographic imaging for SRS localization in phantom. *J Appl Clin Med Phys*. 2019;20:137–144.
15. Pallotta S, Simontacchi G, Marrazzo L, et al. Accuracy of a 3D laser/camera surface imaging system for setup verification of the pelvic and thoracic regions in radiotherapy treatments. *Med Phys*. 2013;40:011710.
16. Pallotta S, Vanzi E, Simontacchi G, et al. Surface imaging, portal imaging, and skin marker set-up vs. CBCT for radiotherapy of the thorax and pelvis. *Strahlenther Onkol*. 2015;191:726–733.
17. Stanley DN, McConnell KA, Kirby N, Gutiérrez AN, Papanikolaou N, Rasmussen K. Comparison of initial patient setup accuracy between surface imaging and three point localization: a retrospective analysis. *J Appl Clin Med Phys*. 2017;18:58–61.
18. Walter F, Freislederer P, Belka C, Heinz C, Söhn M, Roeder F. Evaluation of daily patient positioning for radiotherapy with a commercial 3D surface-imaging system (Catalyst™). *Radiat Oncol*. 2016;11:154.
19. Besl PJ, McKay ND. A method for registration of 3-D shapes. *IEEE Trans Pattern Anal Mach Intell*. 1992;14:239–256.
20. Li H, Sumner RW, Pauly M. Global correspondence optimization for non-rigid registration of depth scans. *Comput Graph Forum*. 2008;27:1421–1430.
21. Nutti B, Kronander Å, Nilsing M, et al. Depth Sensor-Based Realtime Tumor Tracking for Accurate Radiation Therapy. EUROGRAPHICS 2014 / E Galin and M Wand[Inline Image Removed1].
22. Brock KK, Mutic S, McNutt TR, Li H, Kessler ML. Use of image registration and fusion algorithms and techniques in radiotherapy: Report of the AAPM Radiation Therapy Committee Task Group No. 132. *Med Phys*. 2017;44: e43–e76.
23. Meyer J, Smith W, Geneser S, et al. Characterizing a deformable registration algorithm for surface-guided breast radiotherapy. *Med Phys*. 2020;47:352–362.

Paper VI

Faster and more accurate patient positioning with surface guided radiotherapy for ultra-hypofractionated prostate cancer patients

Annika Mannerberg[1], Malin Kügele[1, 2], Sandra Hamid[2], Anneli Edvardsson[2], Kristoffer Petersson[2, 3], Adalsteinn Gunnlaugsson[2], Sven ÅJ Bäck[2], Silke Engelholm[2] and Sofie Ceberg[1]

1) Department of Medical Radiation Physics, Lund University, Lund, Sweden
2) Department of Hematology, Oncology and Radiation Physics, Skåne University Hospital, Lund, Sweden
3) Department of Oncology, Oxford Institute for Radiation Oncology, University of Oxford, Oxford, United Kingdom

Accepted for publication in Technical Innovations & Patient Support in Radiation Oncology (July 2021)

Abstract

Introduction: The aim of this study was to evaluate if surface guided radiotherapy (SGRT) can decrease patient positioning time for localized prostate cancer patients compared to the conventional 3-point localization setup method. The patient setup accuracy was also compared between the two setup methods.

Materials and Methods: A total of 40 localized prostate cancer patients were enrolled in this study, where 20 patients were positioned with surface imaging (SI) and 20 patients were positioned with 3-point localization. The setup time was obtained from the system log files of the linear accelerator and compared between the two methods. The patient setup was verified with daily orthogonal kV images which were matched based on the implanted gold fiducial markers. Resulting setup deviations between planned and online positions were compared between SI and 3-point localization.

Results: Median setup time was 2:50 min and 3:28 min for SI and 3-point localization, respectively ($p < 0.001$). The median vector offset was 4.7 mm (range: 0 – 10.4 mm) for SI and 5.2 mm for 3-point localization (range: 0.41 – 17.3 mm) ($p = 0.01$). Median setup deviation in the individual translations for SI and 3-point localization respectively was: 1.1 mm and 1.9 mm in lateral direction ($p = 0.02$), 1.8 and 1.6 mm in the longitudinal direction ($p = 0.41$) and 2.2 mm and 2.6 mm in the vertical direction ($p = 0.04$).

Conclusions: Using SGRT for positioning of prostate cancer patients provided a faster and more accurate patient positioning compared to the conventional 3-point localization setup.

1. Introduction

Image guided radiotherapy (IGRT) is used in modern radiotherapy to minimize setup errors due to both inter- and intrafractional patient and tumour motion [1, 2]. Recently, a surface imaging (SI) modality has been adopted into the IGRT toolbox with the potential to further decrease the effect of inter- and intrafractional motion during patient positioning and treatment delivery [3, 4]. Surface guided radiotherapy (SGRT) generates real-time three-dimensional (3D) surface images of the scanned patient, which is compared to a reference surface for positioning purposes. Unlike the simple conventional 3-point localization setup method, SGRT provides additional information of the patient topography, highlighting patient posture errors and anatomical deformations (such as swelling or weight loss) [5]. As SI does not contribute to any radiation exposure, it can be used for patient monitoring during treatment delivery. Also, SGRT has the capability of automatic beam-hold if the patient motion exceeds a pre-set threshold [4]. Previous studies have shown that SGRT can provide accurate positioning for various treatment sites and treatment techniques [3, 6-10]. Most widespread, SI has been clinically implemented for positioning of breast cancer patients since the target position is well represented by the surface [8, 11, 12]. The improved setup has the potential to decrease the amount of verification images, which could reduce both setup time and absorbed dose to the patients [4, 8, 13]. For internal treatment sites, the target position is not always well represented by a surface image, resulting in reduced positioning accuracy [3, 6, 14]. For targets in abdomen and pelvis, SGRT achieves the similar accuracy as 3-point localization and is often considered to be used as a complement to verification images [3, 6, 14].

For prostate cancer radiotherapy, the treatment time should preferably be kept as short as possible due to the increased risk of prostate motion over time [15-17]. Having an accurate and fast patient positioning is therefore of particular importance. In recent years, ultra-hypofractionation with a high fractional dose delivered with flattening filter free (FFF) volumetric modulated arc therapy (VMAT) in few fractions has been proposed and implemented in our clinic [18]. With fewer fractions, it is less likely for the total delivered dose distribution to be evenly blurred around the target due to setup deviations. Hence, accurate patient positioning is even more crucial for ultra-hypofractionated treatment. To minimize potential setup errors, the initial patient setup method should provide a reliable correlation to the treatment position. Further, only small shifts after verification imaging are preferable to minimize patient displacements caused by large couch shifts. Two early publications have shown SGRT to be a reproducible and non-invasive method for positioning of prostate cancer patients treated with 3D-conformal radiotherapy [19, 20]. Only a few studies have examined the time efficiency of using surface

imaging during patient positioning instead of 3-point localization setup [9, 10]. These studies showed that the total treatment time can be reduced while improving or maintaining patient position accuracy, however, both studies were carried out on a TomoTherapy treatment system using the time consuming megavoltage computed tomography (MVCT) for image guidance.

The aim of this study was to investigate if SGRT could improve the setup workflow by reducing the setup time while maintaining the positioning accuracy for prostate patients receiving ultra-hypofractionation FFF-VMAT treatment. To our knowledge this is the first study to examine if SGRT can reduce the patient setup time for prostate cancer patients.

2. Method

2.1 Ethics

The Regional Ethical Review Board in Lund has approved retrospective research of radiotherapy data (No. 2013/42).

2.2 Patients

A total of 40 localized prostate cancer patients were included in this study. Each patient received 7 fractions of a 6 MV FFF ultra-hypofractionated VMAT treatment plan with a total absorbed dose of 42.1 Gy, delivered with a TrueBeam linear accelerator (ver 2.5, Varian Medical Systems, Palo Alto, CA). All patients had a CTV to PTV margin of 7 mm, in line with the HYPO-RC-PC trial [18]. The CTV included the prostate only and all patients had three gold fiducial markers implanted at least two weeks prior to start of radiotherapy treatment.

2.3 Positioning

Twenty patients were positioned using the conventional 3-point localization setup method, where skin tattoos were aligned with in-room lasers. The remaining 20 patients were positioned with SI setup where a single camera Catalyst^{TM} (C-Rad Positioning AB, Uppsala, Sweden) system was used for positioning. In this study, patient positioning refers to the initial setup carried out prior to acquisition of verification images.

The beginning of positioning was the same for all patients. All patients were positioned in a Combifix^{TM} (Civco Radiotherapy, IA, USA) for fixation of the knees and legs and were holding a small ring with their hands, placed on their chest. During the first fraction the in-room lasers were aligned with the patient's tattoos.

In order to move the patient from the reference position to the isocenter position, a manual couch shift was performed by the radiation therapists (RTTs). When in isocenter position, marks aligning with the lasers was drawn on the patient's skin.

For all patients, the position was always verified using orthogonal kilovoltage (kV) images, which were considered to be the gold standard. The fiducial markers in the kV images were matched to the position in the digital reconstructed radiograph (DRR). The deviations obtained in lateral (lat), longitudinal (lng) and vertical (vrt) directions from the image matching was compared between SI and 3-point localization setup. The total vector offset, *v*, was calculated using equation (1).

$$v = \sqrt{lat^2 + lng^2 + vrt^2} \quad (1)$$

In total, 280 paired images were analysed regarding patient positioning accuracy.

For the patients positioned with 3-point localization the in-room positioning was considered to be complete when the lasers were aligned with the patient's skin marks. The RTTs then left the treatment room and proceeded with the acquisition of the orthogonal kV images to verify the position of the gold fiducial markers.

2.3.1 Surface imaging setup

The optical surface scanning system Catalyst^{TM} creates 3-dimensional surface images for patient positioning. The hardware and functionality of the Catalyst^{TM} system has been described elsewhere [23, 24].

Skin marks were drawn during the first fraction for patients positioned with SI as well. This was done to help the RTTs in the transition to the new positioning method and these markers were often used the following fractions as a quick initial check for rotations. For SI setup, the reference surface used was the body structure of the planning CT data set, imported from the treatment planning system. Before treatment start, genitalia and the most cranial part of the stomach was cropped from the reference surface.

To obtain the best possible live surface with good surface coverage of the patient, the settings of the Catalyst^{TM} were optimized during the first fraction. Thereafter, the RTTs corrected for any rotations by comparing the live and reference surfaces and using a color map projected on the patient. This color map is a live feedback of the patient position and shows if the live position of the patient differs from the reference one in red and green color. A tolerance level for deviations between live and reference surface can be set, and only deviations larger than this threshold will activate the color map projection [23]. In this study, the color map threshold was set

to 5 mm. Lastly, the couch was shifted with Auto-GoTo to the correct isocenter position calculated with the non-rigid algorithm of the Catalyst™ system. When pressing the Auto-GoTo button, the couch coordinates for positioning the patient in isocenter is sent from the Catalyst™ system to ARIA (Varian Medical Systems, Palo Alto, USA). After this, a button on the treatment couch pendant can be pressed and the couch is automatically moved in lat, lng and vrt according to the calculations done by the Catalyst™ (Figure 1).

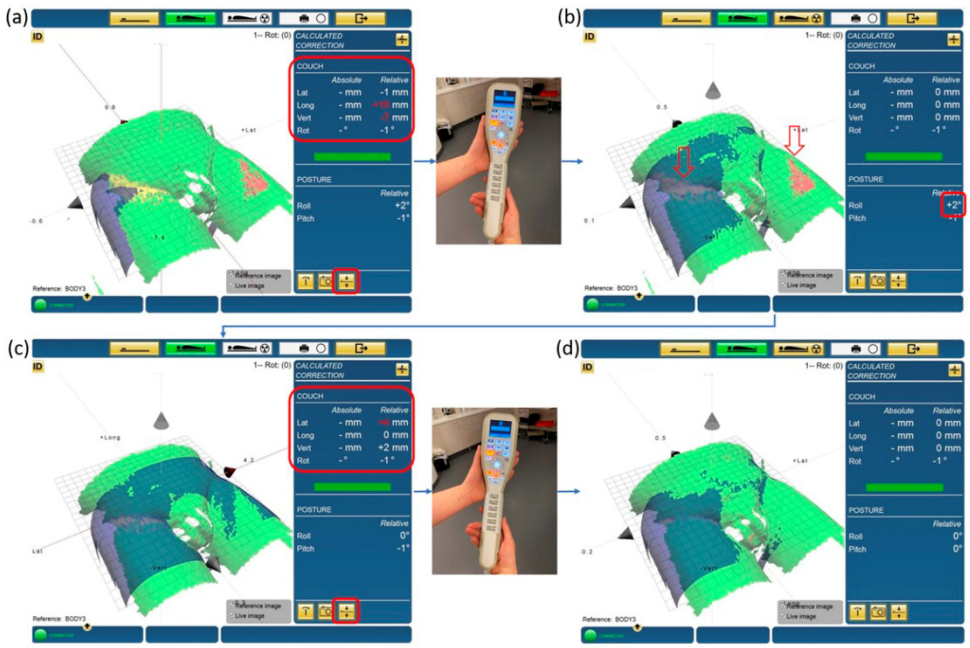

Figure 1. A surface imaging example. The blue and green surfaces are the reference and live surfaces, respectively. The couch was initially shifted to isocenter position using saved couch parameters. The shift indicated by Catalyst™ (Lat -1 mm, Lng +10 mm, Vrt -7 mm) (a) was then applied using the Auto-GoTo function. The color map and the positioning result indicated a roll (b), which was corrected for by asking the patient to adjust himself. Once the roll was corrected for, residual translations (Lat +4 mm, Lng 0 mm, Vrt +2 mm) (c) were applied using Auto-GoTo into the correct treatment position (d).

During the following fractions, the patient was positioned on the couch and the RTTs quickly checked the lasers and skin marks. The couch was initially shifted into the isocenter position using the Auto-GoTo function (Figure 1) using the saved couch parameters. Thereafter, also using the Auto-GoTo function, the couch was shifted to the correct isocenter position according to the Catalyst™. The live and reference surfaces were compared, and any rotations indicated by the Catalyst™

were corrected for. In presence of pelvis rotation, the color map was projected onto the patient's skin for setup correction guidance for the RTTs. The RTTs asked the patient to lift his hips and turn in the direction instructed by the red and yellow colors. After such correction, the Auto-GoTo was used to correct for any residual translations (Figure 1).

2.4 Setup time

The setup times were retrieved from system log files in ARIA. The start of positioning was defined as when the RTTs turned the in-room lasers on or when they first started moving the couch after the patient had been opened in ARIA for treatment, whichever occurred first. The end of positioning was when image acquisition started.

In our clinic there is no separate initial setup session prior to treatment start and instead all initial setup is carried out during the first treatment fraction. During the first fraction of SI setup, the RTTs went through all the steps that also were carried out during the first fraction of 3-point localization setup. This entailed correcting for rotations using the 3-point skin tattoos, manually shifting the couch from reference position to isocenter position and drawing skin marks in the isocenter position, before using SI for positioning. Thus, the time spent on 3-point localization and SI could not be resolved. The positioning time of the first fraction for SI setup was therefore not considered representative and was excluded. To obtain a fair positioning time comparison between the two different setup methods, the setup time of the first fraction for 3-point localization was also excluded. The setup time was investigated for 240 fractions.

2.5 Statistics

The setup time and setup deviation distributions were tested for normality using the Shapiro Wilks test. Setup times were not normally distributed. Consequently, the Mann-Whitney U test was used for comparing the setup times for the two methods. Positioning deviations in the lng and vrt direction for SI were normally distributed, however, positioning deviations for 3-point localization were not normally distributed. To test the hypothesis that the two setup methods result in equal setup accuracy, a Mann-Whitney U test was carried out. A significance level of $\alpha = 0.05$ was used for all tests.

3. Results

3.1 Setup time

The median setup time was 2:50 minutes (min) (range: 1:32 – 6:56 min) for SI, and 3:28 min (range: 1:42 – 12:57 min) for 3-point localization ($p < 0.001$) (Figure 2). On average the setup time decreased with 49 s for each fraction, using SI (Figure 2).

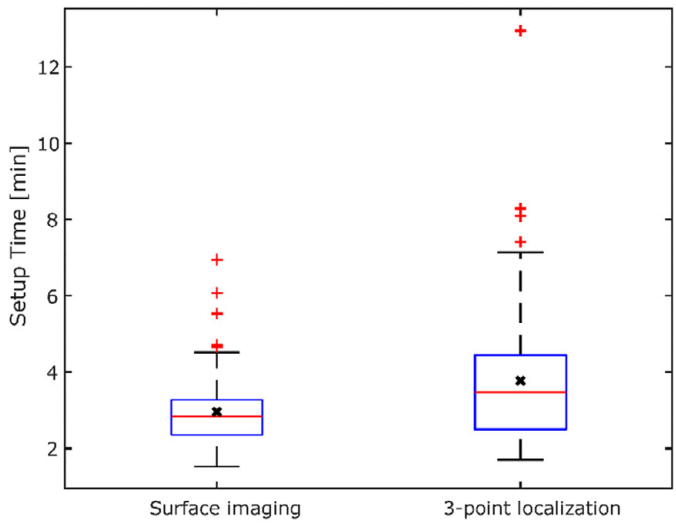

Figure 2. Comparison of patient setup time for surface imaging and 3-point localization setup. The lower quartile is the 25th percentile and the upper quartile is the 75th percentile. The red horizontal lines respresent the median setup time, the black crosses show the mean setup time. The whiskers shows the nonoutlier minimum and maximum value. Outliers are values larger than 1.5 times the interquartile range and are displayed as red plus signs.

3.2 Positioning

The median setup deviation in the lat translation was 1.1 mm (range: 0 – 5.6 mm) for SI and 1.9 mm (range: 0 – 15.2 mm) for 3-point localization ($p = 0.02$) (Figure 3a). For lng setup deviations the median was 1.8 mm (range: 0 – 9.6 mm) for SI and 1.6 mm (range: 0 – 15.2 mm) ($p = 0.41$) (Figure 3b). For vrt the median setup deviation was 2.2 mm (range: 0 – 9.3 mm) for SI and 2.6 mm (range: 0 – 12.6 mm) for 3-point localization ($p = 0.04$) (Figure 3c).

The median vector offset was 4.7 mm (range: 0 – 10.4 mm) for SI and 5.2 mm (range: 0.41 – 17.3 mm) for 3-point localization ($p = 0.01$). The probability of positioning a patient within a total vector offset of 7 mm was 84% for SI and 71%

for 3-point localization (Figure 3d). For 90% of the fractions the total vector offset was within 7.6 mm for SI and 10.1 mm for 3-point localization. For SI, only one fraction had a total vector offset larger than 10 mm, which implies that such large setup deviations occurs less than every 100th fraction. However, for 3-point localization a setup deviation larger than 10 mm occurred approximately every 10th fraction.

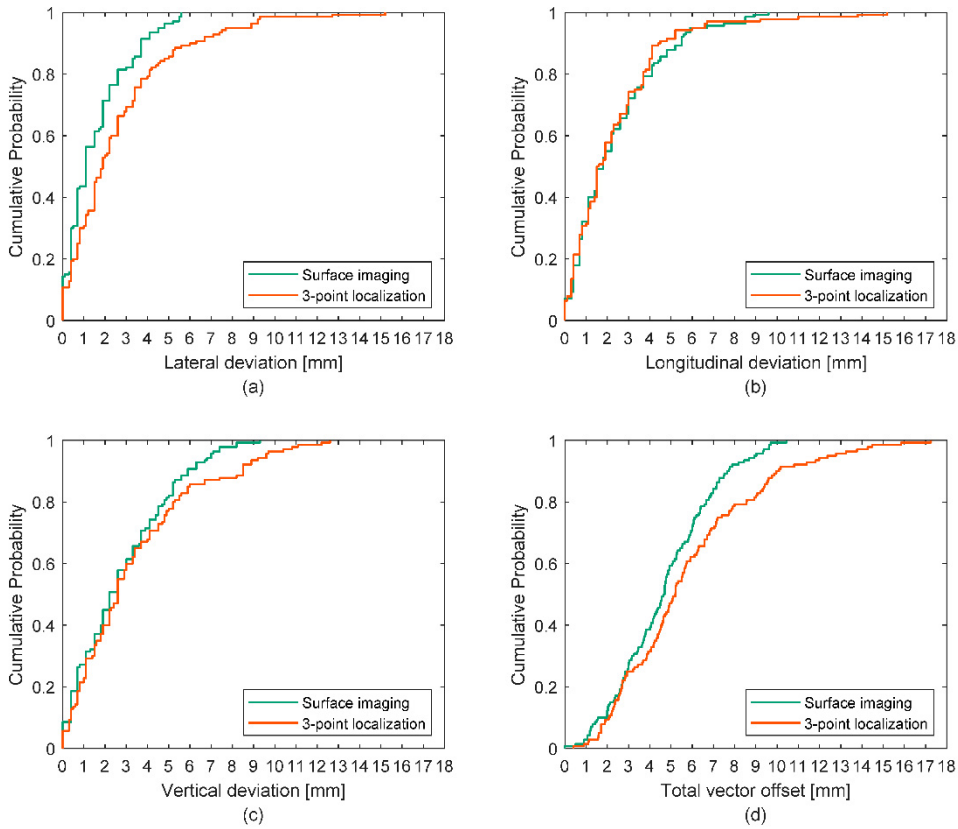

Figure 3. The cumulative probability for setup deviation comparing surface imaging and 3-point localization setup in the lateral (a), longitudinal (b) and vertical (c) direction as well as the total vector offset (d), verified with orthogonal kV images.

4. Discussion

In this study, the potential of SGRT for ultra-hypofractionated prostate cancer radiotherapy treatment, in terms of patient setup efficiency and accuracy, was investigated. Large setup deviations were reduced, while patient setup time was improved with 20% using SI. These findings are to our knowledge the first to show improved setup efficiency while maintaining the standard daily IGRT prostate protocol. It is of great importance to reduce the total treatment time for prostate cancer patients since prostate motion increases over time [15-17]. Langen et al. [15] showed that the prostate can drift 5 mm from isocenter after only 4 min and Ballhausen et al. [16] showed that the variance in prostate position increase over time for all prostate cancer patients. Even small total treatment time reductions in the order of minutes can therefore lead to a reduced effect of intrafractional motion, which is especially important for patients treated with a high fraction dose. Further, a shorter treatment time could also result in higher patient comfort and the possibility to treat more patients. Previously, FFF beams have been implemented which has halved the beam on time [21] for prostate cancer radiotherapy treatments.

This study was designed to isolate the initial setup time between SI and 3-point localization. It is therefore certain that time reductions shown in this study can be traced to the use of SGRT only. The results are independent of for instance the IGRT method used or different treatment techniques. Hence, other clinics who choose to start positioning patients with SI can expect around 1 min in time reduction per treatment fraction.

The patient setup time was found to be significantly reduced using SGRT for positioning of prostate cancer patients, which shows that SGRT is a potent tool to further reduce the treatment fraction time, by reducing the patient setup time. The reduced setup time could be because of a standardized workflow for surface imaging. Thus, the steps in the software are rigid and leaves no room for manual couch adjustments. The information from the color map mitigates the RTTs' subjectivity on how well the patient needs to be aligned since the color map and rotations must be fulfilled, hence the SI system works as an operator-independent check for the patient setup.

When this study was conducted, the use of SI for prostate cancer patients had just been started. The RTTs was therefore at the beginning of their learning curve on how to use the Catalyst^{TM} system for these patients. The Auto-GoTo function was introduced in connection with this project and was an additional step in the SI workflow to learn. Further time reductions might be achievable due to increased experience of using the SGRT system. As a further consequence of this study, the

RTTs have omitted drawing skin marks onto the patients, which also contributes to reducing the setup time.

Previous studies [3, 6, 14] have not shown any improvement using SGRT for pelvis positioning. This could be due to the fact that in those studies, they grouped different target sites in the most caudal part of the body into pelvis/lower extremities. To our knowledge this study is the first to investigate positioning accuracy for prostate patients receiving ultra-hypofractionation FFF-VMAT treatments. In the study by Stanley et al. [3], the average vector offset for treatment sites in the pelvis/lower extremities was 6 mm for setup using surface scanning. This agrees well with the median vector offset obtained in our study of 4.7 mm for SI. However, Stanley et al. found that the average vector offset for setup with lasers and skin marks for pelvis/lower extremities was 9 mm. This is slightly higher than the results in this study where the median vector offset was 5.2 mm for 3-point localization.

An early study by Bartoncini et al. [20] showed improved patient setup in lat and vrt directions using a different SI system and bony image registration for prostate patients. Bartoncini et al. evaluated if SI correlated to verification image registration and did not compare SI to the conventional 3-point localization setup. Hence, the present study is the first to show an improvement in the setup workflow and patient positioning. Positioning results in this study, showed that SI provides a significantly improved surrogate for the target in lat and vrt directions compared to 3-point localization. The improvement in the lat direction could be explained by the fact that a single central tattoo is used for 3-point localization, whereas the full topography of the patient is used for the SI setup. Moreover, while the non-normal distribution of setup deviations for 3-point localization implies a subjective setup method, the normally distributed setup deviations for SI are another indication of a more operator-independent method. Further, a single camera Catalyst^{TM} system was used for setup in this study. However, with a 3-camera Catalyst^{TM} system the patient setup accuracy could potentially be further improved. Additionally, based on these results, patient positioning using SI could potentially be applied for other deeply seated targets.

We have found SI to be useful in combination with kV imaging to prevent patient setup deviations prior to verification imaging. SGRT can be considered as an additional safety component in case imaging is left out or for target sites where daily images are not acquired.

Although outside the scope of this study, another important finding was the improved physical work environment reported by the RTTs when using SI for prostate cancer patients. When SI was used there was a lot less hands-on work for the RTTs and there was not as much need for lifting and pushing the patient into the

correct position. Since the start of this project the RTTs have therefore reportedly experienced a reduction in the amount of back and shoulder pain. These results are however not part of this study and should be further investigated.

5. Conclusion

Surface guided radiotherapy with the Catalyst^{TM} system reduced the patient setup time by approximately 1 minute per treatment fraction. Additionally, the initial patient setup accuracy was significantly improved using the surface imaging setup method prior to IGRT.

References

1. Langen, K.M. and T.L. Jones, *Organ motion and its management.* Int J Radiat Oncol Biol Phys, 2001. **50**(1): p. 265-278.
2. Bertholet, J., et al., *Real-time intrafraction motion monitoring in external beam radiotherapy.* Phys Med Biol, 2019. **64**(15): p. 15TR01.
3. Stanley, D.N., et al., *Comparison of initial patient setup accuracy between surface imaging and three point localization: A retrospective analysis.* J Appl Clin Med Phys, 2017. **18**(6): p. 58-61.
4. Freislederer, P., et al., *Recent advanced in Surface Guided Radiation Therapy.* Radiat Oncol, 2020. **15**(1): p. 187.
5. Batista, V., et al., *Clinical paradigms and challenges in surface guided radiation therapy: Where do we go from here?* Radiother Oncol, 2020. **153**: p. 34-42.
6. Carl, G., et al., *Optical Surface Scanning for Patient Positioning in Radiation Therapy: A Prospective Analysis of 1902 Fractions.* Technol Cancer Res Treat, 2018. **17**: p. 1533033818806002.
7. Wikstrom, K., et al., *A comparison of patient position displacements from body surface laser scanning and cone beam CT bone registrations for radiotherapy of pelvic targets.* Acta Oncol, 2014. **53**(2): p. 268-77.
8. Kügele, M., et al., *Surface guided radiotherapy (SGRT) improves breast cancer patient setup accuracy.* J Appl Clin Med Phys, 2019. **20**(9): p. 61-68.
9. Crop, F., et al., *Surface imaging, laser positioning or volumetric imaging for breast cancer with nodal involvement treated by helical Tomotherapy.* J Appl Clin Med Phys, 2016. **17**(5): p. 200-211.
10. Haraldsson, A., et al., *Surface-guided tomotherapy improves positioning and reduces treatment time: A retrospective analysis of 16 835 treatment fractions.* J Appl Clin Med Phys, 2020.

11. Laaksomaa, M., et al., *Determination of the optimal matching position for setup images and minimal setup margins in adjuvant radiotherapy of breast and lymph nodes treated in voluntary deep inhalation breath-hold.* Radiation Oncology, 2015. **10**.
12. Padilla, L., et al., *Assessment of interfractional variation of the breast surface following conventional patient positioning for whole-breast radiotherapy.* J Appl Clin Med Phys, 2014. **15**(5): p. 4921.
13. Laaksomaa, M., et al., *AlignRT and Catalyst in whole-breast radiotherapy with DIBH: Is IGRT still needed?* J Appl Clin Med Phys, 2019. **20**(3): p. 97-104.
14. Walter, F., et al., *Evaluation of daily patient positioning for radiotherapy with a commercial 3D surface-imaging system (Catalyst).* Radiat Oncol, 2016. **11**(1): p. 154.
15. Langen, K.M., et al., *Observations on real-time prostate gland motion using electromagnetic tracking.* Int J Radiat Oncol Biol Phys, 2008. **71**(4): p. 1084-90.
16. Ballhausen, H., et al., *Intra-fraction motion of the prostate is a random walk.* Phys Med Biol, 2015. **60**(2): p. 549-63.
17. Tong, X., et al., *Intrafractional prostate motion during external beam radiotherapy monitored by a real-time target localization system.* J Appl Clin Med Phys, 2015. **16**(2): p. 51-61.
18. Widmark, A., et al., *Ultra-hypofractionated versus conventionally fractionated radiotherapy for prostate cancer: 5-year outcomes of the HYPO-RT-PC randomised, non-inferiority, phase 3 trial.* The Lancet, 2019. **394**(10196): p. 385-395.
19. Krengli, M., et al., *Reproducibility of patient setup by surface image registration system in conformal radiotherapy of prostate cancer.* Radiat Oncol, 2009. **4**: p. 9.
20. Bartoncini, S., et al., *Target registration errors with surface imaging system in conformal radiotherapy for prostate cancer: study on 19 patients.* Radiol Med, 2012. **117**(8): p. 1419-28.
21. Benedek, H., et al., *The effect of prostate motion during hypofractionated radiotherapy can be reduced by using flattening filter free beams.* Phys Imaging Radiat Oncol, 2018. **6**: p. 66-70.